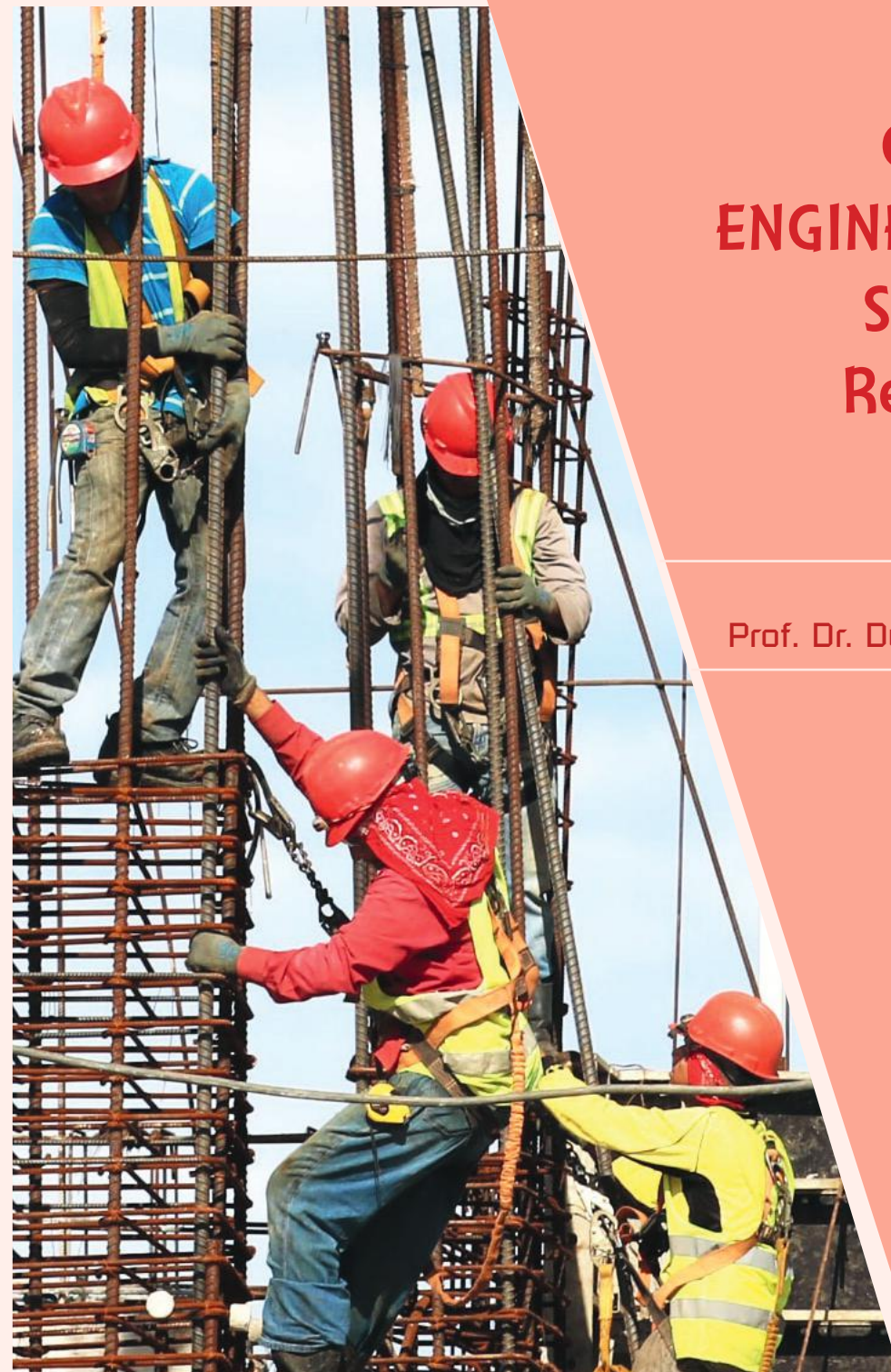


# Current ENGINEERING Sciences Research

Editor  
Prof. Dr. Duygu Kavak







Engineering

ISBN: 978-2-38236-091-0



LIVRE DE LYON

-  [livedelyon.com](http://livedelyon.com)
-  [livedelyon](https://twitter.com/livedelyon)
-  [livedelyon](https://www.instagram.com/livedelyon)
-  [livedelyon](https://www.linkedin.com/company/livedelyon)



LIVRE DE LYON

Lyon 2021


# **Current Engineering Sciences Research**

Editor  
Prof. Dr. Duygu Kavak



LIVRE DE LYON

Lyon 2021

**Editor** • Prof. Dr. Duygu Kavak  ORCID 0000-0002-1189-3110

**Cover Design** • Aruull Raja

**First Published** • January 2021, Lyon

**ISBN:** 978-2-38236-091-0

**© copyright**

All rights reserved. No part of this publication may be reproduced, stored in a retrieval system, or transmitted in any form or by any means, electronic, mechanical, photocopying, recording, or otherwise, without the publisher's permission.

The chapters in this book have been checked for plagiarism by  intihal.net

**Publisher** • Livre de Lyon

**Address** • 37 rue marietton, 69009, Lyon France

**website** • <http://www.livredelyon.com>

**e-mail** • livredelyon@gmail.com



## **PREFACE**

This book is titled as “Current Engineering Sciences Research” and it presents some significant current academic research studies in the field of engineering. The book consists of numerous reports of studies performed in various areas of science and engineering in order to get a multidisciplinary collection representing different points of view of the contributors and their approach to the solution of problems. Written by academics and researchers, this book will be an important resource for anyone in this field. I thank all the authors contributed to the book, the referees evaluated the studies and Livre de Lyon Publishing very much for their invaluable efforts. The editor and the editorial board hope that this book will be useful for all readers, especially for the researchers, engineers and academics.

Prof. Dr. Duygu KAVAK  
Editor



## CONTENTS

<b>PREFACE.....</b>	<b>I</b>
<b>Chapter I     A. S. Yargic</b>	
CONVERSION OF BIOPITCH TO CARBON FOAM WITH TUNABLE PROPERTIES: THE ROLE OF CHEMICAL ACTIVATION.....	<b>1</b>
<b>Chapter II    A. Eğrisöğüt Tiryaki</b>	
ADAPTIVE NEURO-FUZZY BASED APPROACH FOR INVERSE KINEMATICS        SOLUTION        OF        ROBOT MANIPULATOR.....	<b>23</b>
<b>Chapter III   A. Alkhattab &amp; D.Kavak</b>	
INVESTIGATION OF COLOR REMOVAL FROM DAIRY INDUSTRY WASTE WATER USING NF270 MEMBRANE.....	<b>39</b>
<b>Chapter IV    E. Duman &amp; M. Haslak</b>	
EFFECTS of INDUSTRIAL REFINING STAGES ON CORN OIL'S QUALITY AND BIOACTIVE COMPONENTS DETERMINED USING GAS CHROMATOGRAPHY AND INDUCTIVELY COUPLED PLASMA ATOMIC EMISSION SPECTROSCOPY.....	<b>47</b>
<b>Chapter V     H. O. Durmus &amp; E. Cetin Ari &amp; B. Karaboce &amp;                 M. H. Y. Seyidov</b>	
TEMPERATURE CHARACTERIZATION OF LIGHT SOURCES SUCH AS LOW-POWER LASER, INTENSE PULSED LIGHT (IPL) AND LIGHT EMITTING DIODE (LED) USED FOR THERAPEUTIC PURPOSES ON TISSUE- MIMICKING MATERIALS.....	<b>61</b>
<b>Chapter VI    H. O. Durmus &amp; E. Cetin Ari &amp; B. Karaboce &amp;                 M. H. Y. Seyidov</b>	
SAFETY ASSESSMENT OF A 635 NM LOW-POWER SOLID- STATE MEDICAL LASER ON ZERDINE PHANTOM...	<b>81</b>
<b>Chapter VII   B. Yayli &amp; I.Kilic</b>	
MITIGATION OF AMMONIA FROM LITTER BY ADDITIVES IN POULTRY HOUSES.....	<b>103</b>



# CHAPTER I


---

## CONVERSION OF BIOPITCH TO CARBON FOAM WITH TUNABLE PROPERTIES: THE ROLE OF CHEMICAL ACTIVATION

**Adife Seyda Yargic**

*(Asst. Prof. Dr.), Bilecik Şeyh Edebali University, Bilecik, Turkey*

*e-mail: seyda.guler@bilecik.edu.tr*

 ORCID 0000-0002-8671-5896

### 1. Introduction

Carbon foams are cellular structures with characteristic sizes between 100-500  $\mu\text{m}$  and involving randomly distributed pores. The properties of carbon foams can be listed as adjustable thermal and electrical conductivity, lightness, low thermal expansion, high thermal shock resistance, and mechanical strength (Gao, et al., 2018; Liu, et al., 2014; Wang, et al., 2016). These unique properties, which are primarily related to the features of the precursors and working parameters, turn carbon foams into high-performance engineering materials and become attractive for numerous application fields in industries (Tzvetkov, et al., 2016). Carbon foams are evaluated in various usages such as heat exchanger, high-temperature heat insulation, electromagnetic shielding, the electrode for fuel cells, catalyst support, sound/radar absorption, and filter (Antunes and Velasco, 2014; Elgafy and Mishra, 2014; Liu, et al., 2014; Lv, et al., 2012; Micheli, et al., 2014; Velasco, et al., 2010). Traditionally, carbon foams are produced by foaming pitch-based or organic polymer resins, curing in an inert atmosphere and applying carbonization/graphitization processes. Pitch-based carbon foams are in tendency to give a regular graphitic structure and reveal high thermal/electrical conductivities. On the contrary, carbon foams with amorphous structures are synthesized from synthetic polymer resins or naturally renewable materials (Chithra, et al., 2020).

In this study, carbon foam with adjustable properties was synthesized from the pistachio shell, which was renewable household waste, following the stages of pyrolysis, pitch production, foaming, and carbonization, respectively. Within the scope of examining the effect of the chemical activation process on carbon foam properties, it was aimed to increase porosity by applying activation with potassium hydroxide after the foaming process. In the last stage, comprehensive characterization



studies were carried out to determine the CHN content by elemental analysis of carbon foams, to examine their structural, morphological, and crystallographic properties, and to calculate porosity and compression strength values to get information about structure-property relevance.

## **2. Materials and Methods**

### **2.1. The Characteristics of Waste Biomass**

Pistachio shells (*PS*) were first washed with distilled water and were left to dry under laboratory air. Then, the particle size of the raw material was minimized by operating Armfield FT-7A brand grinder and the mean particle size was estimated as 1.57 mm via particle size analysis. *PS* with a particle size in the range of  $0.425 > D_p > 0.25$  mm was used in the experiments. The structural analyzes that determine the amounts of holocellulose, hemicellulose, extractive material, lignin, and cellulose, and also a preliminary analysis of the raw material including moisture, ash, volatile matter, and fixed carbon contents were performed based on ASTM standard test methods (Ozbay and Yargic, 2019). The ultimate analysis was carried out by examining the carbon, hydrogen, and nitrogen contents in the structure of *PS* with the organic sample burning process carried out in the elemental analysis device (Leco CNH628 S628) at 950 °C. The oxygen content was ascertained by subtracting the total amount of CHN% by weight obtained from the elemental analysis process from 100. Besides, thermal degradation behavior of *PS* with thermogravimetric analysis (TGA, Setaram Labsys Evo) and surface morphology with scanning electron microscopy (SEM, Zeiss Supra VP 40) were investigated, and functional groups were recognized by Fourier transform infrared spectroscopy (FT-IR, Perkin Elmer Spectrum 100). Before SEM analysis, the material was platinum-coated under vacuum in the Quorum Q 150 R ES DC Sputter device. FT-IR spectra were taken using the attenuated total reflectance (ATR) technique with a spectral resolution of 4 cm<sup>-1</sup> in the 4000-400 cm<sup>-1</sup> scan range.

### **2.2. Pyrolysis of *PS* and Tar Production**

Pyrolysis process was practiced in stainless steel (# 316) Heinze reactor under static atmospheric conditions at a heating rate of 7 °C/min. The temperature of the reactor was measured with a thermocouple and the heating of the system with the resistance furnace around the reactor was carried out in a controlled manner. The temperature of *PS* (15 g) was raised from T<sub>room</sub> to the final pyrolysis temperature of 400 °C and it was held at this temperature for 20 minutes until no remarkable gas evolution was observed. After condensing the tar and aqueous phase mixture in liquid collection traps at 0 °C, they were washed with dichloromethane and the tar was transferred into the organic phase by splitting up in the separation funnel. In the last stage, the aqueous phase that may have passed into the

organic phase was caught by using anhydrous sodium sulfate, and then the tar yield was calculated by separating the tar and solvent in the rotary evaporator. The solid product yield was determined by weighing the remaining part in the reactor, and the gaseous product yield was attained from the total mass balance. While determining the pyrolysis product distribution, calculations were made on a dry and ash-free basis (daf) and the mean of three runs was taken. Elemental analysis was accomplished to examine the structure of tar ( $PS_{@400\text{ }^{\circ}\text{C}}$ ) to be used in the production of biopitch, FT-IR spectroscopy, proton nuclear magnetic resonance spectroscopy ( $^1\text{H-NMR}$ , Varian Mercury 300 MHz), and gas chromatography-mass spectroscopy (GC-MS, GC-2010 Plus) analysis methods were applied. In the GC-MS device, a TRB-5MS model column with dimensions of  $30\text{m}\times 0.25\text{mm}\times 0.25\mu\text{m}$  was used and the peaks were identified using the Wiley7 library.

### **2.3. Biopitch Production Process from Tar**

The biopitch to be used as a precursor in the fabrication of carbon foam was prepared from the heavy phase aromatic structures in the tar structure by the vacuum distillation process performed for 24 hours at  $250\text{ }^{\circ}\text{C}$  and 50 mbar vacuum pressure. The oxygen content in the structure of biomass-based tar causes the deterioration of the pitch structure at higher temperatures and the formation of solid thermofix carbon residue (Rocha, et al., 2002). Prauchner et al. (2004) found that during the formation of eucalyptus tar pitches through the distillation process at  $250\text{ }^{\circ}\text{C}$ , the C–O bonds in the structure were broken, and although the side chains were released, the heavier fractions in the aromatic ring reacted to create larger molecules. While highlighting the structure of the biopitch, ash content and softening point were determined, elemental analysis, helium gas pycnometer, thermogravimetric analysis, and Fourier transform infrared spectroscopy methods were applied.

### **2.4. Foaming, Carbonization and Activation Processes, Product Characterization**

An inert atmosphere was provided with nitrogen gas during the foaming process of the biopitch performed in the Parr 4575B model reactor (Parr Instrument Company, USA). Synthesized-green foam, which was a semi-finished product, was produced by the process of heating the biopitch up to  $450\text{ }^{\circ}\text{C}$  with a heating rate of  $2.5\text{ }^{\circ}\text{C}/\text{min}$  at 1MPa reactor pressure and releasing the pressure after standing 1 hour at this temperature. To promote the surface area of the synthesized-green foam, a chemical activation process was applied with potassium hydroxide (KOH) in a ratio of foam: activation agent of 1:1 (Tondi, et al., 2010). The chemical reactions during the heat treatment applied to improve the surface area with the help of potassium hydroxide were detailed in the previous study

(Yargic and Ozbay, 2019). In the last stage, the synthesized-green foam and activated foam were heated to 1050 °C with a heating rate of 5 °C/min under a N<sub>2</sub> atmosphere (flow rate 100 mL/min) and carbonized for 2 hours in a tube furnace. The carbonized foams were coded as *PSCF* or *PSACF*, respectively, depending on whether they were synthesized or activated from the pistachio shell-based biopitch.

Elemental analysis, x-ray diffraction (XRD, PANalytical Empyrean, 2 $\theta$ =0–80° range), scanning electron microscope (Zeiss Supra VP 40), nitrogen sorption (Micromeritics ASAP 2020, @ 77 K) techniques were used to analyze the characteristic properties of carbon and activated foams. Also, Shimadzu AG-IC 100KN with a loading speed of 0.5 mm/min was utilized to measure the compressive strengths. Finally, the bulk density of the foams was computed and the porosity(%) was calculated by measuring the actual density values with a helium pycnometer (Micromeritics, Accupyc II 1340).

### 3. Results and Discussion

#### 3.1. The Properties of *PS*

The results of the ultimate and proximate analyses of the pistachio shell were presented in Table 1. According to the elemental analysis results, the higher heating value (HHV) of *PS* was calculated as 15.11 MJ/kg from the Dulong formula (Harker & Backhurst, 1981). The high volatile matter (80.68%) and low ash (2.12%) amounts of the *PS* with the carbon (47.10%) and lignin contents (27.36%) indicated that the selected biomass was suitable for the pyrolysis and biopitch preparation processes to be applied in the development of carbon foam. As shown in Figure 1, it was determined that *PS* consisted of particles with similar structures and had a non-porous morphology due to the image taken at 5000x magnification using the scanning electron microscope.

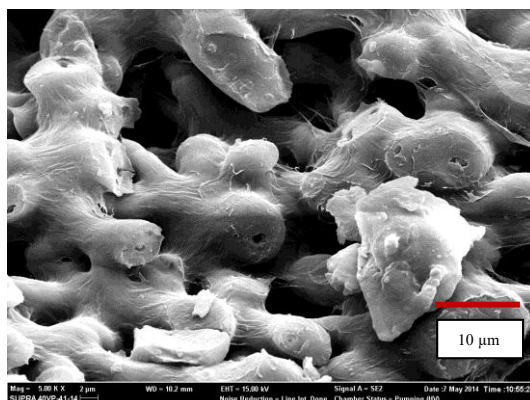


Figure 1. SEM Image of *PS*

Table 1. The Results of Ultimate and Proximate Analyses

<i>Ultimate Analysis</i>		
	<i>PS</i>	<i>PS@400 °C</i>
<b>Component (%)</b>		
C	47.10	51.66
N	2.46	4.66
H	5.08	6.01
O <sup>a</sup>	46.70	37.67
Empirical formula	CH <sub>1.29</sub> N <sub>0.05</sub> O <sub>0.75</sub>	CH <sub>1.40</sub> N <sub>0.08</sub> O <sub>0.55</sub>
H/C	1.29	1.40
O/C	0.75	0.55
HHV (MJ/kg)	15.11	19.35
<i>Proximate Analysis of PS</i>		
<i>Preliminary analysis</i>	<i>wt. %</i>	
Moisture	2.05	
Ash	2.12	
Volatiles	80.68	
Fixed Carbon <sup>a</sup>	15.15	
<i>Structural analysis</i>	<i>wt. %</i>	
Holocellulose	69.84	
Hemicellulose	23.05	
Extractives	0.68	
Lignin	27.36	
Cellulose <sup>a</sup>	46.79	
Average bulk density (g/cm <sup>3</sup> )	0.71	

<sup>a</sup> Calculated by the difference.

TG and dTG curves of the thermogravimetric analysis applied to determine the thermal and pyrolytic behavior of *PS* were shown in Figure 2.a. According to the thermogravimetric analysis results, the moisture in the structure of *PS* was removed in the first step between 80 and 120 °C, the high weight loss was arisen due to the breakdown of cellulose and

hemicellulose through the pyrolysis reaction in the range of 180-450 °C, and the degradation process was slower between 450 and 550 °C with regards to the degradation of lignin (Yargıç et al., 2021). The ash and non-degradable C amounts in the structure of raw material were detected from the residue remaining from the thermogravimetric analysis.

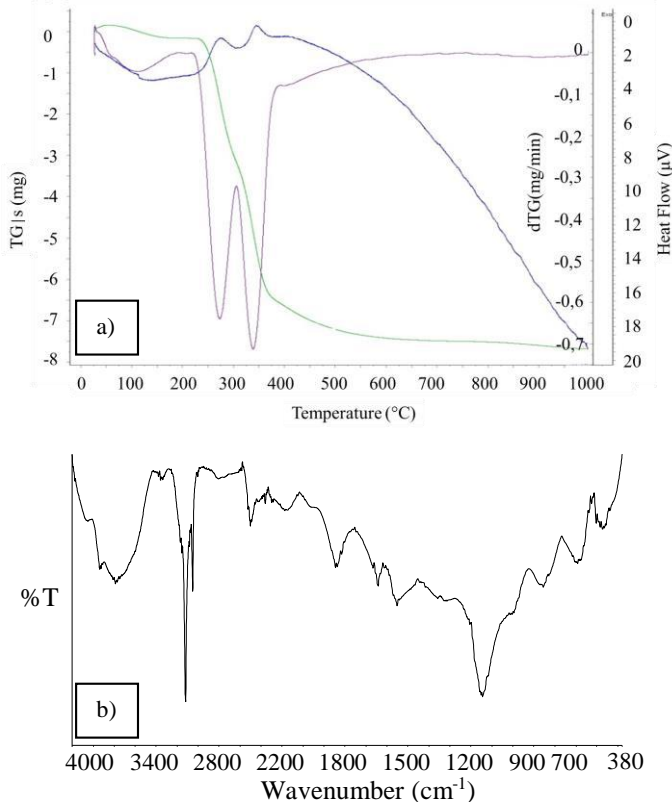


**Figure 2.** a) TG/dTG Curves and b) FT-IR Spectrum of PS

Due to the FT-IR spectrum taken to examine the functional groups in the PS structure (Figure 2b), the wide  $\text{-OH}$  band designating the presence of alcohol/phenol or carboxylic acids around  $3600\text{-}3300\text{ cm}^{-1}$  (Apaydın-Varol and Erülken, 2015) and peaks indicating the entity of aliphatic structures and asymmetrical/symmetrical  $\text{C-H}$  vibrations between  $2950\text{-}2800\text{ cm}^{-1}$  were determined. Strong peaks around  $1770\text{-}1500\text{ cm}^{-1}$  referring to the existence of either ester, ketone, carboxylic acid, or aldehyde indicated the  $\text{C=C}$  stretching vibrations in aromatic and olefinic structures and  $\text{C=O}$  vibrations of the carbonyl group. Peaks in the band range of  $1480\text{-}1420\text{ cm}^{-1}$ , which were an indicator of the presence of unsaturated ethers and phenols, defined  $\text{C-H}$  bending vibrations in aliphatic structures, and peaks between  $1430\text{-}1200\text{ cm}^{-1}$  defined  $\text{-CH}$  bending vibrations of aliphatic methyl and methylene, and also  $\text{C-O-C}$

stretching vibrations of unsaturated ethers. Finally, the C–O stretching band of lignin in the structure of biomass was detected with severe peaks around 1060-1020  $\text{cm}^{-1}$ . Finally, the C–O stretching band of lignin in the structure of biomass was attributed to severe peaks around 1060-1020  $\text{cm}^{-1}$  (Sun and Webley, 2011).

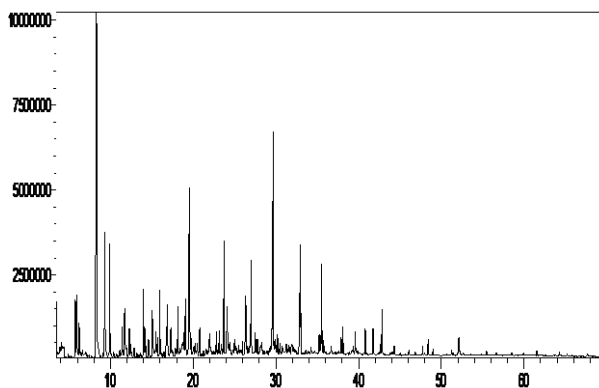
### 3.2. Pyrolysis Product Distribution and Characterization of Tar

According to the product distribution of the pyrolysis of *PS* at 400 °C, the gaseous and solid product yields were determined as 23.11% and 31.75%, respectively. Besides, tar and aqueous phase yields were calculated as 19.40% and 25.74%. As given in Table 1, the C content was detected as 51.66% and the higher heating value was 19.35 MJ/kg in reference to the elemental analysis of tar (*PS*<sub>@400 °C</sub>). Tar produced by thermal degradation of lignocellulosic biomass, which had a complex chemical structure, was found to be comprised of various organic compounds arising from the decomposition of cellulose, hemicellulose, and lignin. Functional groups specified to be in the structure of *PS*<sub>@400 °C</sub> via FT-IR analysis and the atomic structures/groups to which these functional groups belong were presented in Table 2 related to their wavenumber values.

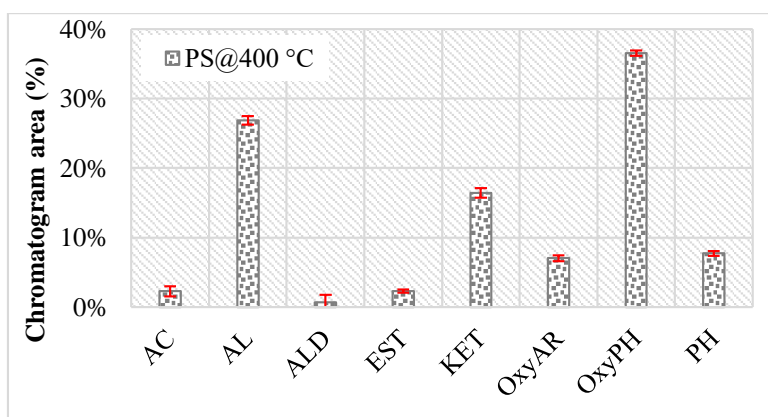
GC-MS chromatogram of *PS*<sub>@400 °C</sub> tar and qualitative composition data of organic fractions defined according to GC-MS analysis results were given in Figure 3 and Figure 4, respectively. Chemical compounds were categorized related to GC-MS chromatogram as acids (AC), alcohols (AL), aldehydes (ALD), esters (EST), phenols (PH), ketones (KET), oxygenated aromatics (OxyAR), and oxygenated phenols (OxyPH). Among these compounds, phenols and aromatic hydrocarbons were classified as high value-added chemicals that could be utilized in the production of next-generation technological materials such as carbon foam or used as fuel (Yaman, et al., 2018). It was found that furan and vanillin compounds were formed in the tar due to the degradation of lignin, which was 27.36% in the pistachio shell with lignocellulosic structure, during the pyrolysis process. Furfural; 2-furan methanol; 2-methoxyphenol; 2-methoxy-4-methylphenol and 2,6-dimethoxyphenol compounds were found more in the composition of *PS*<sub>@400 °C</sub> tar compared to other compounds.

Table 2. FT-IR Results and Functional Groups of *PS*<sub>@400 °C</sub>

Wavenumber (1/cm )	Functional Groups	Atomic Structure and Groups	<i>PS</i> @400 °C
3600-3300	O–H stretching band	Hydroxyl, acid, phenol	3407
3040-3000	C–H stretching band	Aromatic ring	2995
2950-2800	C–H stretching band	Asymmetric and symmetric aliphatic CH <sub>3</sub> and CH <sub>2</sub>	2938
1770-1650	C=O stretching band	Carbonyl group	1711
1625-1590	C=C stretching band	Olefinic structures	1625
1600,1580,1450	C=C stretching band	Aromatic structures	1515
1450 and 1375	C–H bending band	Aliphatic CH <sub>3</sub>	1435 1364
1465	C–H bending band	Aliphatic CH <sub>2</sub>	1463
1275-1200	C–O–C stretching band	Unsaturated ethers	1214
1200-1000	C–H out-of-plane bending band	Aromatic structures	1105
1060-1020	C–O–C stretching band	Aliphatic ether/ Primary or secondary alcohol	1020
900-700		Substituents on the aromatic ring	929, 883, 812, 755



**Figure 3.** GC-MS Chromatogram of  $PS_{@400\text{ }^{\circ}\text{C}}$



**Figure 4.** Chemical Composition of the Organic Fraction  $PS_{@400\text{ }^{\circ}\text{C}}$

The results of the  $^1\text{H-NMR}$  analysis applied to illustrate the hydrogen species in the structure of  $PS_{@400\text{ }^{\circ}\text{C}}$  were represented in Table 3. According to the  $^1\text{H-NMR}$  spectrum related to the chemical shift of the proton species, it was noticed that the proportion of hydrogen bonds in aromatic and phenolic compounds, which were noteworthy in biopitch and carbon foam formation, was high. Thus, it was concluded that;

- i) Aromatic hydrogen bonds belonging to aromatics and conjugated olefins were found as 28.37% in the range of 9.0-6.0 ppm,
- ii) Allylic and vinylic hydrogen bonds defining phenols and unconjugated olefins were ascertained as 8.04% in the range of 6.0-4.0 ppm.



Table 3.  $^1\text{H-NMR}$  Analysis Results of  $PS_{@400\text{ }^\circ\text{C}}$ 

<b>Chemical shift range, <math>\delta</math> (ppm)</b>	<b>Hydrogen type</b>	<b><math>PS_{@400\text{ }^\circ\text{C}}</math></b>
<b>0.5-1.0</b>	$\text{CH}_3$ and paraffinic $\text{CH}_3$ groups in $\gamma$ or farther positions attached to the aromatic ring	2.31
<b>1.0-1.5</b>	$\text{CH}_3$ , $\text{CH}_2$ , and $\text{CH}$ in the $\beta$ position of the aromatic ring	8.66
<b>1.5-2.0</b>	$\text{CH}_2$ and $\text{CH}$ attached to naphthenes	5.21
<b>2.0-3.0</b>	$\text{CH}_3$ , $\text{CH}_2$ , and $\text{CH}$ in the $\alpha$ position of the aromatic ring	32.96
<b>0.5-3.0</b>	<b>TOTAL ALIPHATICS</b>	<b>49.15</b>
<b>3.0-4.0</b>	Hydroxyls, ring-binding methylene, methyl and methoxy	13.13
<b>4.0-6.0</b>	Phenols, non-conjugated olefins	8.04
<b>6.0-9.0</b>	Aromatics, conjugated olefins	28.37
<b>9.0-12.0</b>	Aldehydes and/or carboxylic acids	1.31

### 3.3. The Properties of Biopitch

The elemental analysis, softening point (SP) and actual density measurements, % ash and % yield calculation results of biopitch ( $PS\text{-}P50\text{-}250^\circ\text{C}\text{-}24\text{h}$ ) prepared from  $PS_{@400\text{ }^\circ\text{C}}$  were given in Table 4. Accordingly, as a result of the vacuum distillation process carried out for 24 hours at  $250\text{ }^\circ\text{C}$  and 50 mbar vacuum pressure, the biopitch with a C content of 73.785% was produced with a yield of 20.37%. Considering the C content of the raw material (47.10%), it was stated that the C content of the biopitch was ~57% higher than the raw material. Besides, the ash amount of the biopitch structure was at a negligible level of 0.181% while the ash content in the  $PS$  structure was 2.12%. The softening point of  $PS\text{-}P50\text{-}250^\circ\text{C}\text{-}24\text{h}$  was compatible with the softening points of biomass-based pitches in the literature and was measured as  $129.8\text{ }^\circ\text{C}$  (Prauchner, et al., 2004; Yargic and Ozbay, 2019).

Table 4. Biopitch Properties (T=250 °C, P=50mbar, t=24 h)

<b>Precursor</b>	<b><i>PS biopitch</i></b>
C (%)	73.785
H (%)	6.627
O (%)	18.695
N (%)	0.893
Pitch yield (%)	20.37
Ash (%)	0.181
Density (g/cm <sup>3</sup> )	1.22
SP (°C)	129.8

The functional groups in the biopitch structure, which had a complex composition and contained lignin-derived compounds, were elucidated by examining the FT-IR spectrum (Figure 5). In reference to the FT-IR spectrum, peaks of –OH and –COOH for free alcohol and phenolic compounds near 3300 cm<sup>-1</sup>, and CH stretching vibrations related to alkane structure around 2900 cm<sup>-1</sup> were detected. The existence of C≡CH alkyne stretching vibrations was proved by the peak observed in the 2100 cm<sup>-1</sup> band. Unconjugated C=O (aldehyde, ketone, carboxylic acid) stretching vibration peaks around 1700 cm<sup>-1</sup>, C=C<sub>ar</sub> stretching band indicating the presence of aromatic structures between 1600 and 1400 cm<sup>-1</sup>, CH bending band of guaiacyl- and syringyl- derivatives at 1115 cm<sup>-1</sup> and finally, the peak of C=C cis bending band close by 750 cm<sup>-1</sup> were observed (Araújo and Pasa, 2003; Araújo and Pasa, 2004; Melo and Pasa, 2003). The presence of hydroxyl and carboxyl groups referring to the existence of oxygenated derivatives such as alcohol, phenol, aldehyde, ketone, and carboxylic acid in the structure of the biopitch, which was determined to have 18.695% O content from the elemental analysis results, was supported by the FT-IR spectrum.

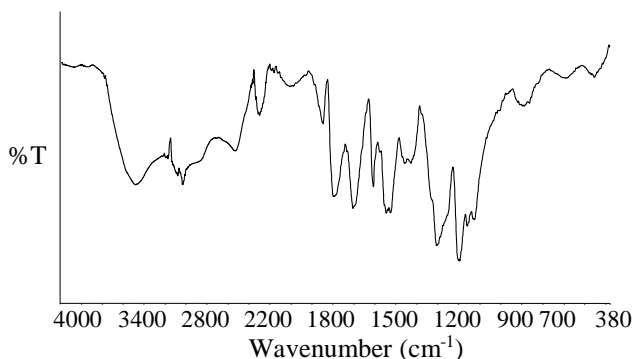


**Figure 5.** FT-IR Spectrum of *PS-P50-250°C-24h*

TG and dTG curves of the thermogravimetric analysis process performed by heating the biopitch under a nitrogen sweeping environment from room temperature to 1000 °C were shown in Figure 6. Regarding the TG curve, a residue (44%) was formed as a result of decomposition reactions that started at 200 °C and proceeded continuously up to 620 °C. The behavior of the biopitch against the heating process applied during the foaming process in the reactor was analyzed by the thermogravimetric analysis. Oxygen, which was ascertained to be ~ 19% via elemental analysis, moved away from the complex biopitch structure rich in aromatic components during the foaming process and caused 56% degradation of the biopitch as it supported self-combustion.

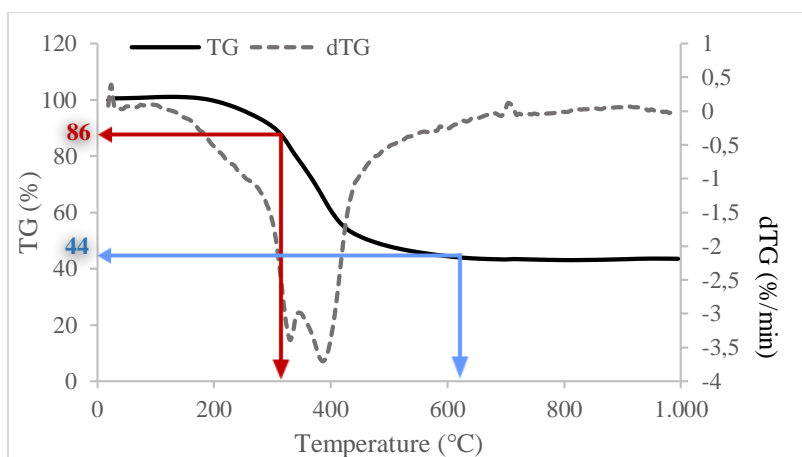


**Figure 6.** TG and dTG Curves of *PS-P50-250°C-24h*

### 3.4. The Characteristics of Carbon Foams

#### 3.4.1. Elemental analysis

Elemental analysis results of carbonized foams (*PZCF* and *PZACF*) synthesized from *PS*-based biopitch or after the activation process

were shown in Table 4. Conceiving that the *PS-P50-250°C-24h* biopitch had 73.785% C and 18.695% O contents, the C content of biopitch-based foams after carbonization increased to 91.66% and 84.046%; whereas the O content decreased inversely to 5.736% and 13.570% for *PZCF* and *PZACF*, respectively. In conclusion, higher O and lower C contents were obtained when the activation process was applied after the foaming step compared to the directly synthesized carbon foam.

Table 4. Elemental Analysis Results of Carbon Foams

Foam	C (%)	H (%)	O (%)	N (%)
<i>PZCF</i>	91.66	0.71	5.736	1.894
<i>PZACF</i>	84.046	0.552	13.570	1.832

### 3.4.2. Scanning electron microscope images

Both *PZCF* and *PZACF* had similar cell sequences at 200x magnification of SEM images (Figure 7). Although the pores of the *PZCF* carbon foam were partially closed, the pores of the *PZACF* were relatively open, and also micro-cracks formed in the material structure. It was observed clearly that the formation of windows, which allowed adjacent cells to connect, in the carbon wall developed with the KOH activation. The opening of the pores caused an enhancement in the surface area and thus a reduction in the compressive strength. While there were cells of various sizes in the range of 200-520  $\mu\text{m}$  in the structure of the non-activated foam, it was found out that smaller cells and a more regular pore network were originated in the 40-335  $\mu\text{m}$  range, thus the porosity was increased after the activation process.

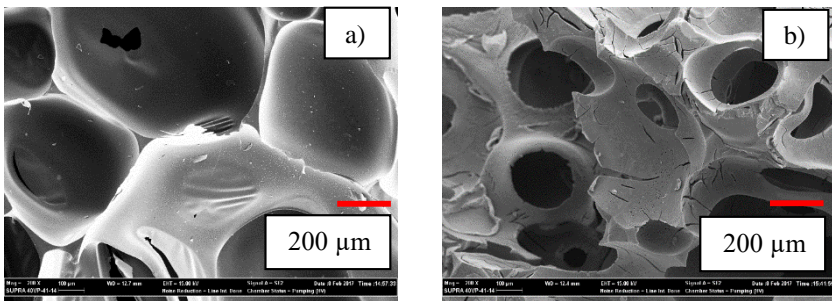
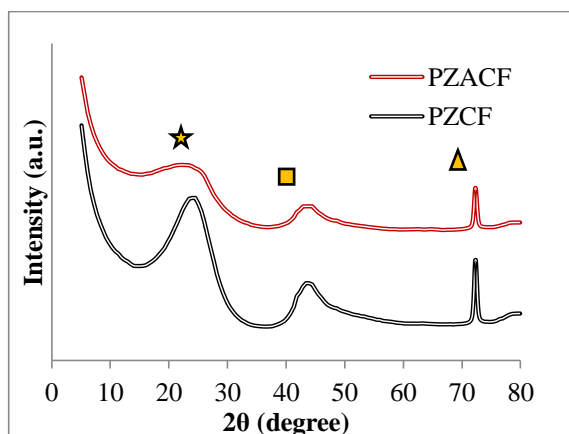


Figure 7. SEM Images of a) *PZCF* and b) *PZACF*

### 3.4.3. X-ray diffraction patterns

XRD parameters and diffraction patterns of biopitch-based non-activated and activated carbon foams were offered in Table 5 and Figure 8. In the X-ray diffraction patterns, (1 0 0) and (0 0 2) planes were specified as two characteristic planes particular to carbon-based materials.

The broadband stacked graphitic basal plane (0 0 2), the maximum value of which was around  $2\theta=23^\circ$  in XRD patterns of all carbonaceous materials and detected in the range of  $2\theta=10^\circ-30^\circ$ , was also identified in diffraction patterns of pistachio shell biopitch-based carbon foams (Apaydın-Varol & Erülken, 2015; Girgis, et al., 2002; Lopez, et al., 2013; Ozbay & Yargic, 2019; Tushar, et al., 2012; Zhang, et al., 2014). Besides, the diffraction peaks around  $2\theta=23^\circ$  and  $43^\circ$  corresponded to the planes of hexagonal carbon (0 0 2) and hexagonal graphite (1 0 0), respectively (Gamllen & White, 1976; Hull, 1926; Li, et al., 2014; Lipson and Stokes, 1942; Strano, et al., 2002; Wang, et al., 2012); and the peak around  $2\theta=72^\circ$  belonged to orthorhombic graphite (Fayos, 1999). It was proven that the thermoplastic property of the biopitch and small molecules in the structure prepossessed the structural arrangement even at a low carbonization temperature of 1050 °C and promote the development of carbon crystals (Prauchner et al., 2005).



**Figure 8.** X-Ray Diffraction Patterns of *PZCF* and *PZACF* (★ : Hexagonal Carbon, ■ : Hexagonal Graphite, ▲ : Orthorhombic Graphite)

Table 5. XRD Parameters of *PZCF* and *PZACF*

Foam	$2\theta$ (002)	$d_{002}$	$2\theta$ (100)	$d_{100}$
	(°)	(nm)	(°)	(nm)
<i>PZCF</i>	23.95	0.3713	43.38	0.2084
<i>PZACF</i>	23.01	0.3862	43.38	0.2084

#### 3.4.4. Structural analysis

Nitrogen sorption isotherms and pore size distributions, which were analyzed to elucidate the pore structures of carbon foams, were shown in Figure 9, and also BET surface area, pore-volume, and average pore

diameter values were given in Table 6. Following the SEM analysis, the surface area value (783,171 m<sup>2</sup>/g) of the carbon foam (PZACF), which had an open porous structure as a result of chemical activation, was much higher than the surface area (1,334 m<sup>2</sup>/g) of the unactivated carbon foam (PZCF). The adsorption/desorption isotherms of the carbon foams conformed to the type IV isotherm implying the presence of micro and mesopores according to the IUPAC classification. When the pore size distribution plots were investigated, it was designated that the PZCF carbon foam had an average pore diameter of 2.60 nm and showed a regular pore size distribution. It was concluded that the size of the smaller pores formed during the chemical activation process in the structure of the PZACF was not uniform, but the average pore diameter (1.22 nm) value shifted towards the micropore range, thus the surface area was improved.

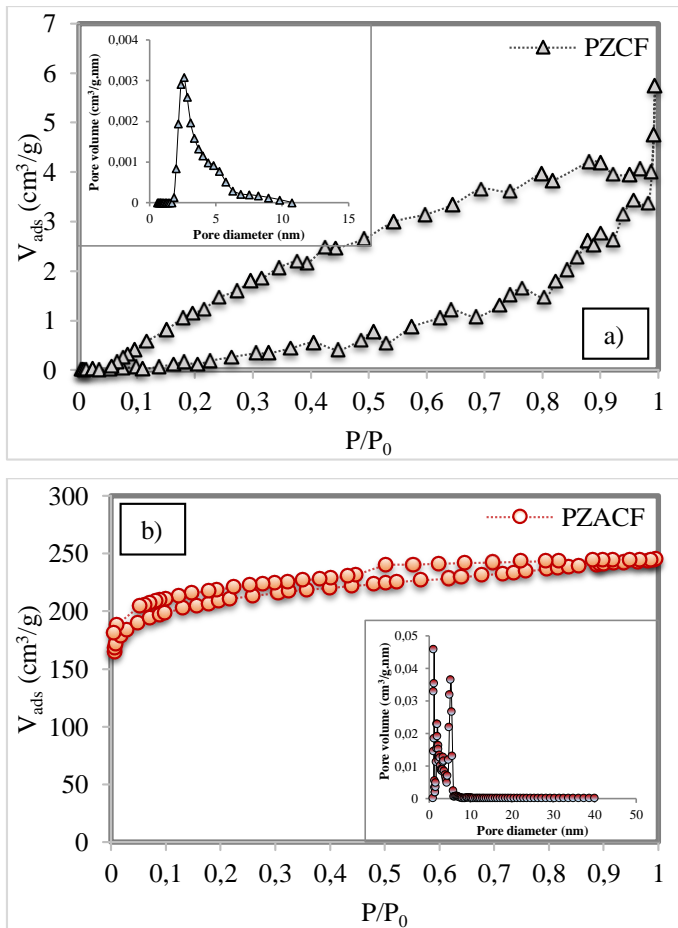


**Figure 9.** Nitrogen Sorption Isotherms and Pore Size Distribution Plots of a) PZCF and b) PZACF

Table 6. Structural Properties of Carbon Foams

<b>Foam</b>	<b>S<sub>BET</sub></b> <b>(m<sup>2</sup>/g)</b>	<b>V<sub>total</sub></b> <b>(cm<sup>3</sup>/g)</b>	<b>V<sub>micro</sub></b> <b>(cm<sup>3</sup>/g)</b>	<b>V<sub>meso</sub></b> <b>(cm<sup>3</sup>/g)</b>	<b>Average pore diameter</b> <b>(nm)</b>
<i>PZCF</i>	1.334	6.1686	0.0002	6.1684	2.60
<i>PZACF</i>	783.171	0.3623	0.3083	0.0540	1.22

### 3.4.5. Compressive strength and porosity(%)

It is known that the cell structure and density of porous carbon foam are directly related to its strength and thermal conductivity. Increasing the number of micro and mesopores in the foam structure improves porosity but diminishes its strength value (Luo, et al., 2013; Yargic & Ozbay, 2019). The porosity(%) was calculated due to the actual and bulk density values specified in Table 7. Hereunder, depending on the formation of windows connecting adjacent cells by chemical activation process, the porosity value of *PAZCF* carbon foam was calculated as 91.32% while *PACF*'s was 87.96%. However, the compressive strength test results revealed that *PZACF* strength value decreased by 71.36% compared to *PZCA* carbon foam, inversely proportional to porosity(%). The results obtained were in accordance with the scanning electron microscope images and surface area values, and the properties of the material were diversified with the chemical activation process.

Table 7. Compressive Strength and Porosity(%) Values of Biopitch-Based Carbon Foams

<b>Foam</b>	<b>Strength</b> <b>(MPa)</b>	<b>Bulk density</b> <b>(g/cm<sup>3</sup>)</b>	<b>Actual density</b> <b>(g/cm<sup>3</sup>)</b>	<b>Porosity</b> <b>(%)</b>
<i>PZCF</i>	0.887	0.1902	1.5795	87.96
<i>PZACF</i>	0.254	0.1535	1.7689	91.32

## 4. Conclusion

In recent years, studies on the selection of sustainable precursors in the production of carbonaceous materials, optimizing the synthesis conditions, and arranging the product properties to suit the application area have come to the fore. In the study, it was aimed to obtain tar from the pistachio shell, which was a household biomass waste, by pyrolysis process at 400 °C, and to evaluate the biopitch produced by vacuum distillation of tar in carbon foam production. In this context, the effects of

the chemical activation process on carbon foam properties were studied in detail. The properties of the carbon foam (CHN content, compressive strength, crystalline structure, morphology, surface area, etc.) were significantly changed due to the formation of interconnected open cells in the biopitch-based foam structure as a result of the chemical activation process. It was determined that the C content of the carbon foam (*PZCF*) synthesized without chemical activation was 9% higher than the *PZACF* foam. Considering the compressive strength values, *PZCF* carbon foam was 3.49 times more resistant than *PZACF* foam. Compared to the *PZCF* foam produced without chemical activation, the porosity of *PZACF* carbon foam was raised by 3.82%, which supported the presence of micropores in the structure and confirmed the enhancement in surface area. As a result, it is possible to synthesize high-tech materials such as carbon foam from nutshells by applying simpler and economical processes as an alternative to the high temperature/pressure conditions required in the processing of coal and petroleum-based pitches and to tailor their properties via process parameters.



## References

- Antunes, M., & Velasco, J. I. (2014). Multifunctional polymer foams with carbon nanoparticles. *Progress in Polymer Science*, 39(3), 486-509.
- Apaydın-Varol, E., & Erülken, Y. (2015). A study on the porosity development for biomass-based carbonaceous materials. *Journal of the Taiwan Institute of Chemical Engineers*, 54, 37-44.
- Araujo, R. C. S., & Pasa, V. M. D. (2003). Mechanical and thermal properties of polyurethane elastomers based on hydroxyl-terminated polybutadienes and biopitch. *Journal of applied polymer science*, 88(3), 759-766.
- Araújo, R. C. S., & Pasa, V. M. D. (2004). New Eucalyptus tar-derived polyurethane coatings. *Progress in Organic Coatings*, 51(1), 6-14.
- Chithra, A., Wilson, P., Vijayan, S., Rajeev, R., & Prabhakaran, K. (2020). Carbon foams with low thermal conductivity and high EMI shielding effectiveness from sawdust. *Industrial Crops and Products*, 145, 112076.
- Elgafy, A., & Mishra, S. (2014). A heat transfer model for incorporating carbon foam fabrics in firefighter's garment. *Heat and Mass Transfer*, 50(4), 545-557.
- Fayos, J. (1999). Possible 3D carbon structures as progressive intermediates in graphite to diamond phase transition. *Journal of Solid State Chemistry*, 148(2), 278-285.
- Gamlen, P. H., & White, J. W. (1976). Structure and dynamics of microcrystalline graphite, graphon, by neutron scattering. *Journal of the Chemical Society, Faraday Transactions 2: Molecular and Chemical Physics*, 72, 446-455.
- Gao, N., Cheng, B., Hou, H., & Zhang, R. (2018). Mesophase pitch based carbon foams as sound absorbers. *Materials Letters*, 212, 243-246.
- Girgis, B. S., Yunis, S. S., & Soliman, A. M. (2002). Characteristics of activated carbon from peanut hulls in relation to conditions of preparation. *Materials Letters*, 57(1), 164-172.
- Harker, J. H., & Backhurst, J. R. (1981). Fuel and energy. Academic Press Limited, London.
- Hull, A. (1926). *Berichte der Deutschen Chemischen Gesellschaft*. 59, 2433-2444.
- Li, W., Huang, Z., Wu, Y., Zhao, X., & Liu, S. (2015). Honeycomb carbon foams with tunable pore structures prepared from liquefied larch sawdust by self-foaming. *Industrial Crops and Products*, 64, 215-

223. Lipson, H., & Stokes, A. R. (1942). A new structure of carbon. *Nature*, *149*(3777), 328-328.
- Liu, H., Li, T., Wang, X., Zhang, W., & Zhao, T. (2014). Preparation and characterization of carbon foams with high mechanical strength using modified coal tar pitches. *Journal of Analytical and Applied Pyrolysis*, *110*, 442-447.
- Lopez, F. A., Centeno, T. A., Garcia-Diaz, I., & Alguacil, F. J. (2013). Textural and fuel characteristics of the chars produced by the pyrolysis of waste wood, and the properties of activated carbons prepared from them. *Journal of Analytical and Applied Pyrolysis*, *104*, 551-558.
- Luo, X., Mohanty, A., & Misra, M. (2013). Lignin as a reactive reinforcing filler for water-blown rigid biofoam composites from soy oil-based polyurethane. *Industrial Crops and Products*, *47*, 13-19.
- Lv, Y., Gan, L., Liu, M., Xiong, W., Xu, Z., Zhu, D., & Wright, D. S. (2012). A self-template synthesis of hierarchical porous carbon foams based on banana peel for supercapacitor electrodes. *Journal of Power Sources*, *209*, 152-157.
- Melo, B. N., & Pasa, V. M. (2003). Composites based on eucalyptus tar pitch/castor oil polyurethane and short sisal fibers. *Journal of applied polymer science*, *89*(14), 3797-3802.
- Micheli, D., Morles, R. B., Marchetti, M., Moglie, F., & Primiani, V. M. (2014). Broadband electromagnetic characterization of carbon foam to metal contact. *Carbon*, *68*, 149-158.
- Ozbay, N., & Yargic, A. S. (2019). Carbon foam production from bio-based polyols of liquefied spruce tree sawdust: Effects of biomass/solvent mass ratio and pyrolytic oil addition. *Journal of Applied Polymer Science*, *136*(11), 47185.
- Prauchner, M. J., Pasa, V. M., Molhallem, N. D., Otani, C., Otani, S., & Pardini, L. C. (2005). Structural evolution of Eucalyptus tar pitch-based carbons during carbonization. *Biomass and Bioenergy*, *28*(1), 53-61.
- Prauchner, M. J., Pasa, V. M., Otani, C., Otani, S., & de Menezes, S. M. (2004). Eucalyptus tar pitch pretreatment for carbon material processing. *Journal of applied polymer science*, *91*(3), 1604-1611.
- Rocha, J. D., Coutinho, A. R., & Luengo, C. A. (2002). Biopitch produced from eucalyptus wood pyrolysis liquids as a renewable binder for carbon electrode manufacture. *Brazilian Journal of Chemical Engineering*, *19*(2), 127-132.

- Strano, M. S., Zydney, A. L., Barth, H., Wooler, G., Agarwal, H., & Foley, H. C. (2002). Ultrafiltration membrane synthesis by nanoscale templating of porous carbon. *Journal of membrane science*, 198(2), 173-186.
- Sun, Y., & Webley, P. A. (2011). Preparation of activated carbons with large specific surface areas from biomass corncob and their adsorption equilibrium for methane, carbon dioxide, nitrogen, and hydrogen. *Industrial & engineering chemistry research*, 50(15), 9286-9294.
- Tondi, G., Pizzi, A., Delmotte, L., Parmentier, J., & Gadiou, R. (2010). Chemical activation of tannin–furanic carbon foams. *Industrial Crops and Products*, 31(2), 327-334.
- Tushar, M. S. H. K., Mahinpey, N., Khan, A., Ibrahim, H., Kumar, P., & Idem, R. (2012). Production, characterization and reactivity studies of chars produced by the isothermal pyrolysis of flax straw. *Biomass and bioenergy*, 37, 97-105.
- Tzvetkov, G., Tsyntsarski, B., Balashev, K., & Spassov, T. (2016). Microstructural investigations of carbon foams derived from modified coal-tar pitch. *Micron*, 89, 34-42.
- Velasco, L. F., Tsyntsarski, B., Petrova, B., Budinova, T., Petrov, N., Parra, J. B., & Ania, C. O. (2010). Carbon foams as catalyst supports for phenol photodegradation. *Journal of Hazardous Materials*, 184(1-3), 843-848.
- Wang, R., Li, W., & Liu, S. (2012). A porous carbon foam prepared from liquefied birch sawdust. *Journal of Materials Science*, 47(4), 1977-1984.
- Wang, Y., He, Z., Zhan, L., & Liu, X. (2016). Coal tar pitch based carbon foam for thermal insulating material. *Materials Letters*, 169, 95-98.
- Yaman, E., Yargic, A. S., Ozbay, N., Uzun, B. B., Kalogiannis, K. G., Stefanidis, S. D., Pachatouridou, E. P., Iliopoulou, E. F., & Lappas, A. A. (2018). Catalytic upgrading of pyrolysis vapours: Effect of catalyst support and metal type on phenolic content of bio-oil. *Journal of Cleaner Production*, 185, 52-61.
- Yargıç, A. Ş., Şahin, R. Z. Y., & Özbay, N (2021). Investigation of solvent type effect on the structural properties of bio-polyol-based carbon foam. *Journal of the Faculty of Engineering and Architecture of Gazi University*, 36(1), 133-146.
- Yargic, A. S., & Ozbay, N. (2019). Effect of chemical activation on the cellular structure of biopitch-derived green carbon foam. *Diamond and Related Materials*, 96, 58-66.

Zhang, S., Zheng, M., Lin, Z., Li, N., Liu, Y., Zhao, B., Pang, H., Cao, J., He, P., & Shi, Y. (2014). Activated carbon with ultrahigh specific surface area synthesized from natural plant material for lithium–sulfur batteries. *Journal of Materials Chemistry A*, 2(38), 15889–15896.




## CHAPTER II

---

# ADAPTIVE NEURO-FUZZY BASED APPROACH FOR INVERSE KINEMATICS SOLUTION OF ROBOT MANIPULATOR

**Aysun Eğrisöğüt Tiryaki**

*(Asst. Prof. Dr.), Sakarya University, Sakarya, Turkey*  
*e-mail: aysune@sakarya.edu.tr*

 ORCID 0000-0001-6440-8396

### 1. Introduction

The use of robots has become indispensable in many areas today due to factors such as rapidly developing technology, increase in mass production, industrial progress and high labour costs. In recent years, the increasing density of work processes has revealed the acceleration requirements of robotic systems by maintaining high precision and accuracy. Researchers have aimed to develop intelligent and learning robots for the solution of this problem and suggested artificial intelligence techniques for this. Some of these techniques are the artificial neural network imitated the human brain (Song et al, 2015; Luan et al, 2019; Zheng et al, 2021), particle swarm optimization algorithm inspired by the bird and fish flocking (Wang et al, 2016, Dereli and Köker, 2018), firefly algorithm inspired by the social behaviour of fireflies in the tropical (Dereli and Köker, 2019b; Sadhu et al, 2018). In parallel with these, studies are also carried out on solving the inverse kinematics. and motion planning to achieve results into shorter times in computations with high difficulty in robotics applications.

In order to control and plan the motion of robot manipulators, there is need for robot kinematics identified the relationship between Cartesian coordinates in which robot movements are expressed and joint parameters in which the control is achieved. In the inverse kinematics solution, traditional methods used geometric, iterative and algebraic methods are inadequate due to the nonlinear equations and the complexity of the robot manipulator increasing exponential with the number of joints. For example, the closed-form or analytic solutions are not guarantee by algebraic methods, and if the geometric method is used closed-form solutions of the first three joints must be geometrically. The numerical

iterative inverse kinematics solution converges to a single solving based on beginning point. Also, in these conventional solution methods, the advanced complexity in the geometrical structure of the robot can cause in a prohibitive computational cost. For this reason, researchers have suggested the alternative solution methods based on artificial intelligence techniques to solve the inverse kinematics problem, as in other problems related to robots.

Köker et al. (2004) used cubic trajectory planning and proposed the neural network to solve inverse kinematics of the three-joint robot manipulator. Bingul et al. (2005) applied backpropagation neural network for the inverse kinematics problem of 6R robot manipulator which does not exist closed form solution.

Daya et al. (2010) presented a neural network architecture, which consist of 6 sub-neural, with a back-propagation training algorithm to the inverse kinematic solution of robotic manipulators with 2 or higher degrees of freedom. Köker (2013) developed a hybrid intelligent technique by integration Artificial Neural Networks (ANN) and Genetic Algorithm (GA). This technique obtained satisfactory results in terms of position error compared to artificial neural networks. El-Sherbiny et al. (2018) compared ANN, Adaptive Neuro Fuzzy Inference System (ANFIS) and GA techniques used to solve the inverse kinematics of the five degrees of freedom (DOF) robot arm. Narayan and Singla (2017) solved the inverse kinematic of a 4-DOFs SCARA robot by using ANFIS with Gaussian membership function. Duka (2015) investigated the use of a neuro-fuzzy based solution to the inverse kinematic problem of 3-DOF planar robot.

In this study, an ANFIS model was generated by using a hybrid approach that combines the artificial neural network and fuzzy logic system to solve the inverse kinematics of a 5 DOF robot manipulator designed in a similar structure to a human arm. The ANFIS network was trained using the real data collected from the robot arm and the training performance was examined. Then, the ANFIS network, whose training was completed, was tested by using new Cartesian coordinates. Experimental data obtained from the robot arm and ANFIS test results was presented comparatively.

## **2. Robot Kinematics**

Robot kinematics analyse the motion in the robot manipulator's workspace. The kinematics solution for any multi-DOFs robotic manipulator consists of two sub problems forward and inverse kinematics (Figure 1). Forward kinematics calculate position in the Cartesian space of the robot manipulator end-effector using joint variables (length of each limb and each joint angle). In the inverse kinematics solution, which is the more difficult and complex, is calculated the joint variables from position

in the Cartesian space of the robot manipulator end effector. That is, the inverse kinematics involve conversion from Cartesian space to joint space.

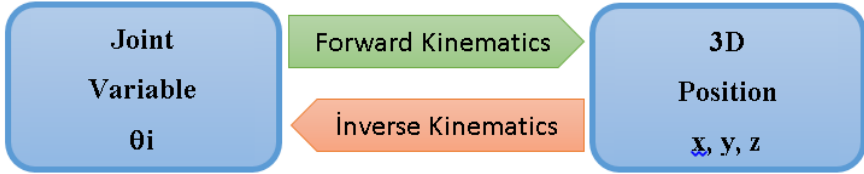


Figure 1. The forward and inverse kinematics of robot manipulator

### 3. Adaptive Neuro Fuzzy Interface System (ANFIS)

ANFIS is a network based hybrid approach which combines parallel computing and learning ability of the artificial neural network with inference features of the Sugeno-type fuzzy logic system. The method first suggested by Jang can construct an input-output mapping based on both human knowledge (as fuzzy if-then rules) and input-output datasets. He reported that the ANFIS architecture can be employed to model nonlinear functions, identify nonlinear components in a control system, and predict a chaotic time series. He also suggested to use in applications of the automatic control and signal processing (Jang, 1993).

The main purpose of ANFIS, to tune the membership function parameters of the fuzzy system by the learning algorithm of ANN using the training input-output data. This tuning is done so that there is minimum error between ANFIS output and real output.

#### 3.1. ANFIS Architecture

For simplicity, suppose that a fuzzy inference system has 2 inputs ( $x$  and  $y$ ) and single output ( $z$ ). Typical rule form for the first-order Sugeno fuzzy model, which contains two fuzzy if-then rules, is as follows (Jang, 1993; Jang and Sun, 1995):

$$\text{Rule 1: If } x \text{ is } A_1 \text{ and } y \text{ is } B_1, \text{ then } f_1 = p_1x + q_1y + r_1 \quad (1)$$

$$\text{Rule 2: If } y \text{ is } A_2 \text{ and } y \text{ is } B_2, \text{ then } f_2 = p_2x + q_2y + r_2 \quad (2)$$

where,  $x$  and  $y$  are two input variables,  $f_i$  ( $i=1,2$ ) is one output variables,  $A_j$  and  $B_j$  ( $j=1,2$ ) are linguistic variables and  $p_i$ ,  $q_i$  and  $r_i$  are consequent parameters adjusted in the training process.

ANFIS has a five-layer feed forward network architecture. The architecture of the considered ANFIS network is illustrated with two input-single output in Figure 2. In this figure, circle represents a fixed node and square represents an adaptive node. The node functions of each layer in the ANFIS structure and the operation of the layers are described in the following.



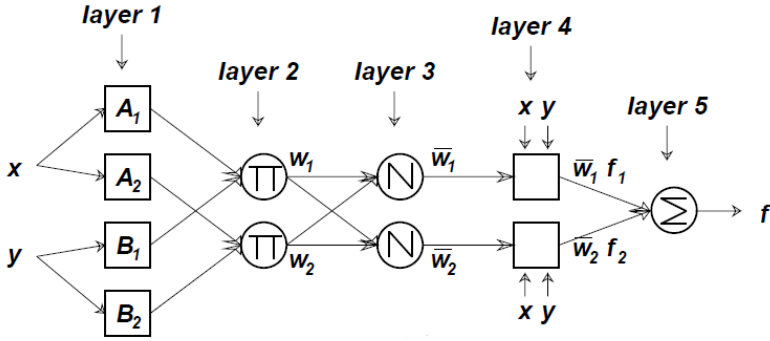


Figure 2. The schematic diagram of the ANFIS structure (Jang 1993)

*Layer 1: Fuzzification layer*

Every node  $i$  of this layer are adaptive node and its outputs consist of membership degrees depending on the membership function and the input values. Node outputs are given by:

$$Q_i^1 = \mu_{A_i}(x), (i=1,2) \quad (3)$$

where  $A_i$  is fuzzy set attached to node and  $\mu_{A_i}$  is membership function.  $Q_i^1$  is the output of node  $i$  in first layer. The same structure is considered for the second ANFIS input variable  $y$ . The most widely used parameterized membership functions are Gaussian, triangular, bell-shaped and trapezoidal. These parameters of the membership functions change shape of the function and adapted during the learning phase. For example, using the Gaussian membership function,  $\mu_{A_i}$  is as follows:

$$f(x; \sigma, c) = e^{-\frac{(x-c)^2}{2\sigma^2}} \quad (4)$$

where  $\sigma$  and  $c$  are width of the fuzzy set and centre of the Gaussian membership function, respectively and are called premise parameters.

*Layer 2: Rule layer*

The nodes in the second layer are fixed nodes and labelled with  $\Pi$ . The nodes of this layer implement the AND operator by using T-norm operation or algebraic product. The outputs of the nodes represent the firing strength  $w_i$  of each rule and is given by:

$$Q_i^2 = w_i = \mu_{A_i}(x) \times \mu_{B_i}(y), (i=1,2) \quad (5)$$

*Layer 3: Normalization layer*

This layer has fixed nodes labelled N and their outputs is normalized firing strengths. The outputs of this layer is calculated by ratio of each rule's firing strength to sum of all rule's firing strengths:

$$Q_i^3 = \bar{w}_i = \frac{w_i}{\sum_{i=1}^2 w_i}, (i=1,2) \quad (6)$$

*Layer 4: Defuzzification layer*

The nodes of this layer are adaptive nodes. The weighted consequent value of the given rule is calculated in each node. Its outputs are represented by:

$$Q_i^4 = \bar{w}_i f_i = \bar{w}_i (p_i x + q_i y + r_i), (i=1,2) \quad (7)$$

where  $\bar{w}_i$  is the output of the third layer, and  $p_i$ ,  $q_i$  and  $r_i$  are the consequent parameters.

*Layer 5: Summation (Output) layer*

There is the single fixed node in this layer, labelled with C. The node output is the overall output computed as the sum of the signals entering node and expressed as follows:

$$Q_i^5 = \sum_{i=1}^2 \bar{w}_i f_i = \frac{\sum_{i=1}^2 w_i f_i}{\sum_{i=1}^2 w_i}, (i=1,2) \quad (8)$$

### 3.2. Training of the ANFIS Model

Training ANFIS means adjusting of the premise parameters of the membership function and consequent parameters of the output polynomial in the layer 4, utilizing an optimization algorithm. In order to update the parameters of the ANFIS network, Jang (1993) proposed four methods listed as following according to computation complexities:

1. All parameters are updated only by the *gradient descent*.
2. The *Least Squares Estimation* (LSE) is used once to obtain initial values of the consequent parameters, and then the gradient descent is applied to adjust all parameters.
3. It is hybrid learning algorithm combining gradient descent and LSE.
4. All parameters are updated only by the sequential (approximate) LSE. Kalman filter algorithm is operated to adjust the parameters.

For the training process of ANFIS a hybrid learning method is used most of the applications. In the forward pass of ANFIS network, the node outputs go forward until the defuzzification layer and consequent parameters are determined by the least squares estimation technique. In the backward pass, error signals are propagated backward and backpropagation gradient descent method utilized to update the premise parameters. Table 1 summarizes the forward and backward activities. A detailed reference to ANFIS and its learning process is available in (Jang, 1993).

Table 1. The forward and backward passes in the hybrid learning process for ANFIS (Jang, 1995)

	Forward Pass	Backward Pass
<b>Premise Parameters</b>	Fixed	Gradient Descent
<b>Consequent Parameters</b>	Least Squares Estimation	Fixed
<b>Signals</b>	Node Outputs	Error signals

#### 4. Application of ANFIS to Inverse Kinematics Solution of 5 DOF Robotic Manipulator

The robotic manipulator designed similar to the human arm consists of three main parts connected to each other, namely the shoulder, upper arm and forearm and a gripper. The robotic arm has five degrees of freedom which are three at the shoulder and two at the elbow, and five revolute joints. Figure 3 shows model of the robotic arm used in this work.

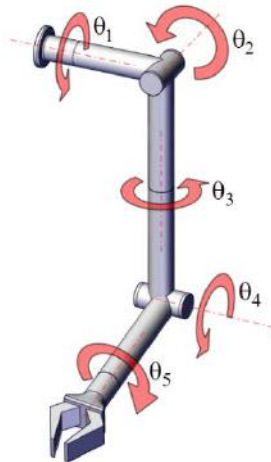


Figure 3. The 5 DOF Robotic Arm Model

ANFIS uses supervised learning method, which requires the training database consisting of example input-output pairs. In this study, all training and test data were obtained through the direct kinematic solution and real time robot arm motion. In ANFIS model designed to solve the inverse kinematic problem, the Cartesian coordinates ( $x, y, z$ ) of the robotic arm end effector is the inputs and the joint angles ( $\theta_1, \theta_2, \theta_3, \theta_4, \theta_5$ ) is the

outputs. ANFIS model consists in 5 parallel layers, one per DOF and all of layers uses the Cartesian coordinates as input. The ANFIS architecture is depicted in Figure 4.

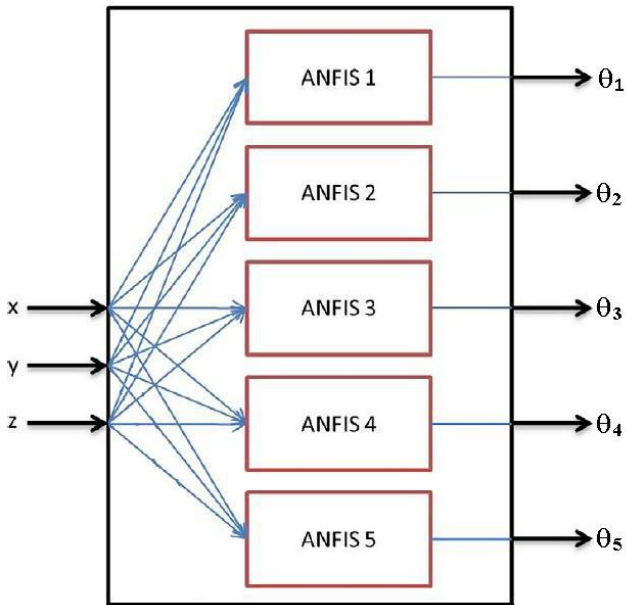


Figure 4. Proposed ANFIS architecture

The basic procedure of ANFIS approach is defined in four steps, as shown in Figure 5. In the first step, data set of the problem is loaded and inputs and output are defined. In the second step, parameters such as membership function, optimization method, the number of epochs are set. In the third, learning process start. When the training is finished, the final membership functions and training error from the training data set are produced and the system performance is evaluated. In the last step, validation occur with independent testing data. These data set do not include output value.

Each of the five ANFIS networks (ANFIS-1, ANFIS-2, ANFIS-3, ANFIS-4 and ANFIS-5) uses 3 membership functions for each of three input variables x, y and z, meaning rule base generated for each ANFIS network consists of 27 fuzzy rules. MATLAB's Fuzzy Logic Toolbox software is used to create the ANFIS model. The structure of ANFIS model is shown in Figure 6. This structure of ANFIS networks resulted after running different configurations of the fuzzy inference system. These were considered (for each network) as combinations 3, 4, 5 membership functions per input/output, different membership function types and various value of the training epochs.

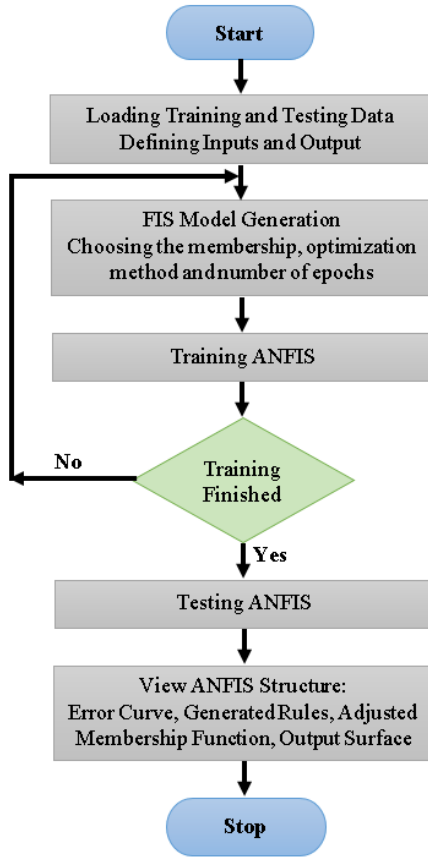


Figure 5. The flowchart of ANFIS procedure

The input membership functions were chosen as the Gaussian function dedicated in Equation (4). The output membership functions given as  $f_i$  in Equation 7 are linear. Number of nonlinear parameters called as premise parameters in Gaussian function are 18. Number of linear parameters called as consequent parameters in output membership functions are 108.

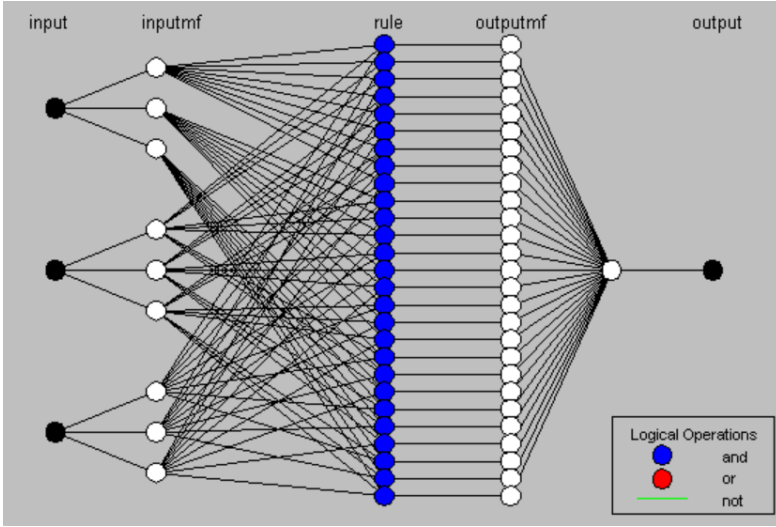
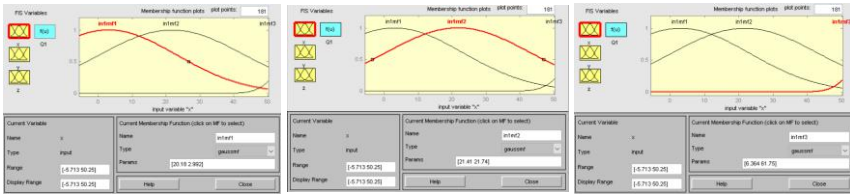


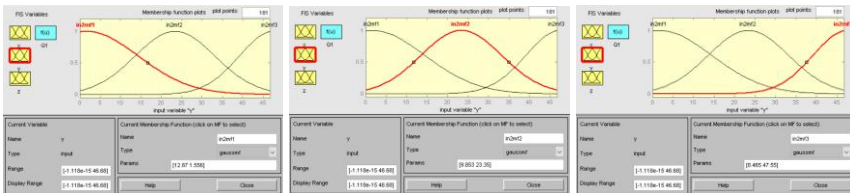
Figure 6. ANFIS structure with three inputs and one output

### 5. Results and Discussion

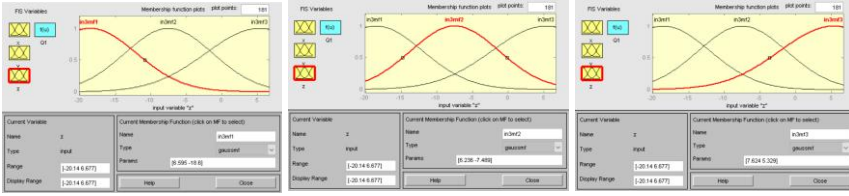
The generated each ANFIS network was trained in 2500 epochs using 447 input-output data pairs and the learning process was completed. Premise and consequent parameters were adapted during the learning process. Figure 7 show the premise parameters values and shape of membership functions after training the AFNIS-1 model. Similarly, after training of the other ANFIS models, adjusted membership functions were obtained. After training the AFNIS-1 model, adjusted consequent parameters ( $p_i, q_i, r_i, s_i$ ) values of the linear function identified as  $p_i x + q_i y + r_i z + s_i$  is presented Table 2.



(a)



(b)



(c)

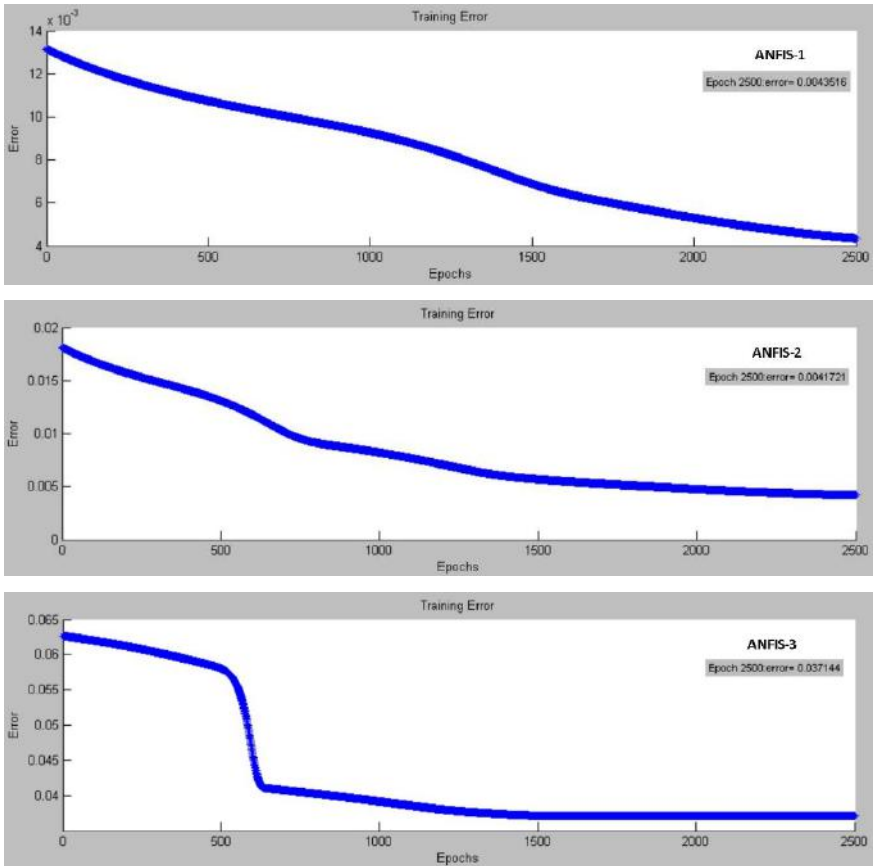
Figure 7. ANFIS-1 membership functions: a) x-coordinate, b) y-coordinate, c) z-coordinate

Table 2. The Consequent Parameters Values of the ANFIS-1 Linear Function

Rule No.	Consequent Parameters			
	p	q	r	s
1	0.1284	0.03851	0.03055	3.073
2	-0.11	-0.02774	0.03675	-0.5825
3	0.01338	0.7015	-0.06132	2.844
4	0.02064	0.03125	-0.03074	1.571
5	-0.02258	0.01661	-0.02561	1.23
6	-0.0439	0.0905	-0.01002	-3.751
7	-0.02047	0.01878	-0.05302	0.1845
8	0.0246	0.02677	-0.04372	2.067
9	0.01986	0.0229	-0.03715	2.981
10	0.0758	0.01013	0.01178	-4.736
11	-0.05524	0.0659	-0.08607	1.581
12	0.4026	-0.9031	-0.008655	-7.2
13	0.07173	0.04903	-0.06699	-5.755
14	0.03889	0.02866	-0.04796	-2.537
15	-0.01145	-0.04494	-0.03587	4.392
16	0.04576	0.08328	0.05006	-3.019
17	0.08632	0.02729	0.03871	-4.229
18	0.1017	0.06416	0.0285	-6.839
19	1.145	-1.976	3.061	-0.4262

20	-0.7825	2.335	-1.186	-0.7569
21	1.349	-7.486	-0.5749	-0.4986
22	-0.2987	-0.7347	-3.326	0.4642
23	-0.368	0.798	0.358	2.398
24	1.055	-1.159	0.2623	0.541
25	-2.091	4.604	-1.659	0.0362
26	-6.435	10.96	5.551	-0.2272
27	0.3114	0.9024	4.409	-0.2931

In Figure 8, root mean squared errors (RMSE) at each training epoch during the training of adaptive network is shown.





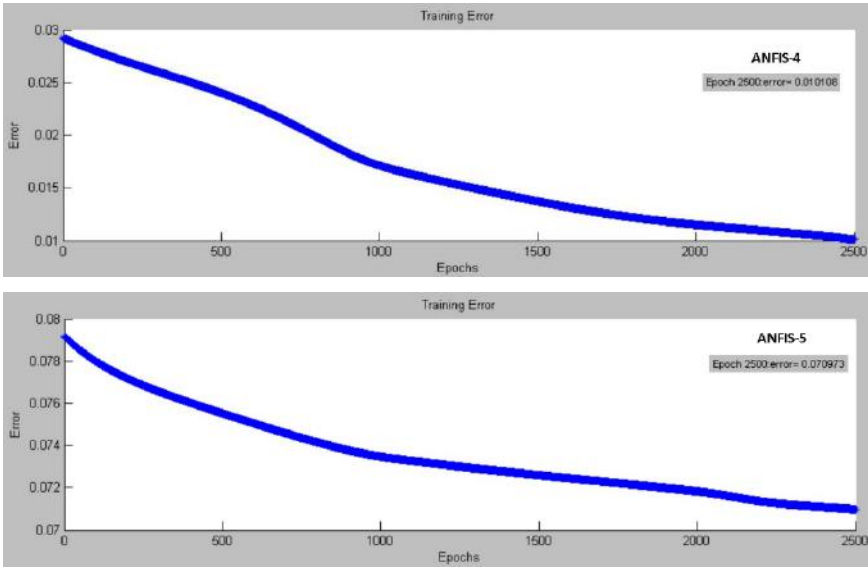
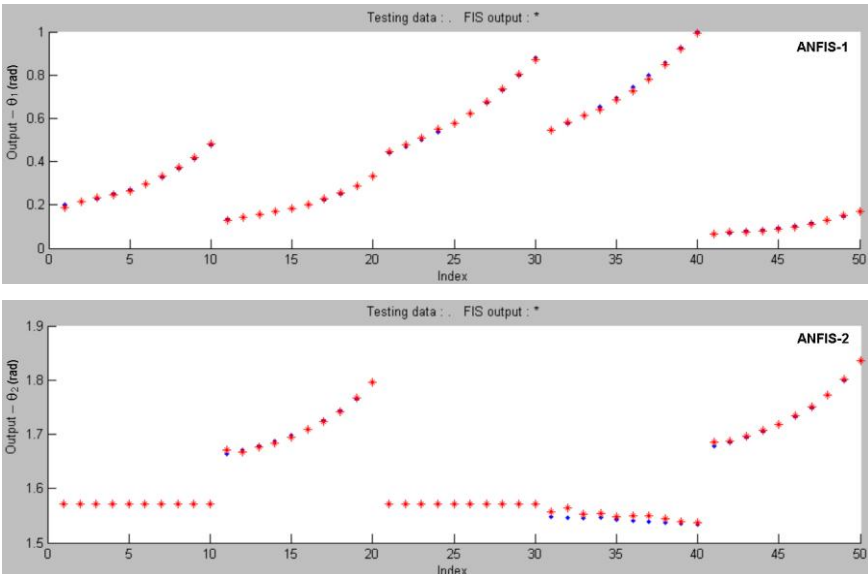


Figure 8. Error-epochs curves of the generated ANFIS models

Using a test data set, the difference between the desired and test output value has been compared to evaluate generated ANFIS structure. The comparative parity plot for test results of each ANFIS model and desired joint angles ( $\theta_1, \theta_2, \theta_3, \theta_4, \theta_5$ ) is indicates in Figure 9. As can be seen in test results, ANFIS has a very strong prediction and a good generalization on solving inverse kinematic problem.



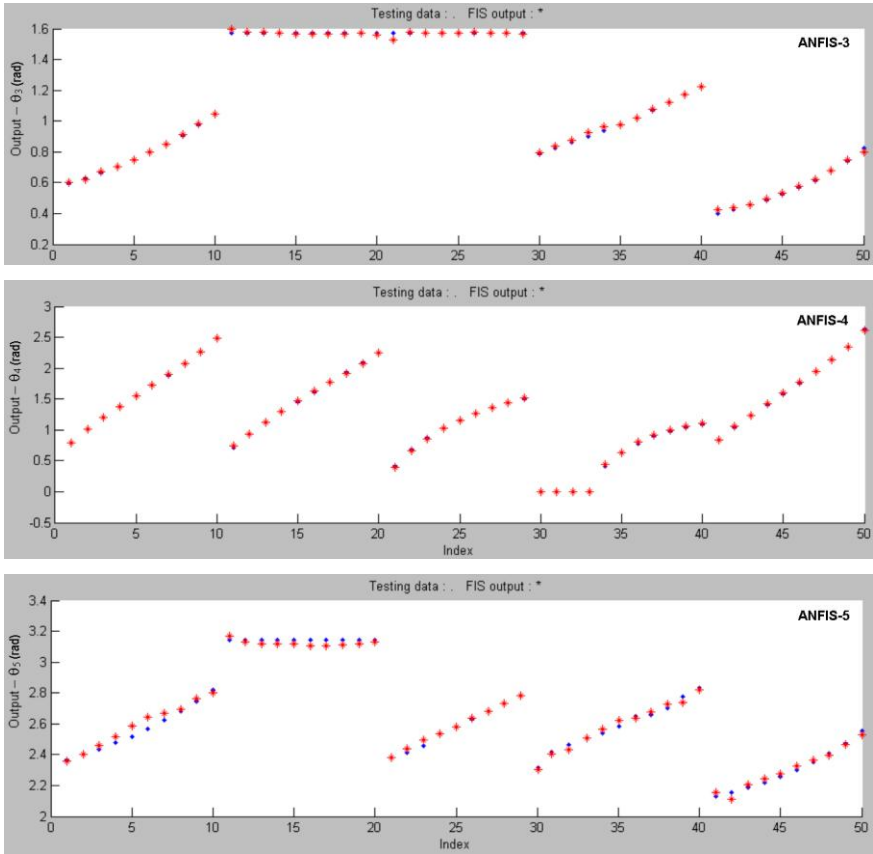


Figure 9. Desired values and ANFIS model predictions of joint angles for test data set

## 6. Conclusion

In real time control applications of the robot manipulator, one of the most important and difficult problems to solve is the inverse kinematics. Traditional methods are known to be insufficient and slow in inverse kinematics solution. In this study, ANFIS algorithm which combines of fuzzy logic and neural networks has been utilized to solve the inverse kinematics problem of a five degrees of freedom robot manipulator. When the training performance of the ANFIS network was evaluated a high correlation was obtained. Test results showed that the absolute fit of ANFIS models to the reference was good. In addition, this work has shown that the proposed ANFIS model can generate an alternative solution to the inverse kinematics problem with minimum analytical effort and much lower computational cost respect to the traditional approaches.

## References

- Bingul, Z., Ertunç, H.M. and Oysu, C. (2005). Applying neural network to inverse kinematic problem for 6r robot manipulator with offset wrist. 7th International Conference on Adaptive and Natural Computing Algorithms, 112-115.
- Daya, B., Khawandi, S. and Akoum, M. (2010). Applying neural network architecture for inverse kinematics problem in robotics. *Journal of Software Engineering and Applications*, 3, 230-239.
- Dereli, S. and Köker, R. (2018). IW-PSO Approach to the Inverse Kinematics Problem Solution of a 7-DOF Serial Robot Manipulator, *Sigma Journal of Engineering and Natural Sciences*, 36, 77-85.
- Dereli, S. and Köker, R. (2020). Calculation of the inverse kinematics solution of the 7-DOF redundant robot manipulator by the firefly algorithm and statistical analysis of the results in terms of speed and accuracy, *Inverse Problems in Science and Engineering*, 28, 601-613.
- Duka, A.V. (2015). ANFIS Based Solution to the Inverse Kinematics of a 3DOF Planar Manipulator, *Procedia Technology*, 19, 526-533.
- El-Sherbiny, A., Elhosseini, M.A. and Haikal, A.Y. (2018). A comparative study of soft computing methods to solve inverse kinematics problem. *Ain Shams Engineering Journal*, 9(4), 2535-2548.
- Jang, J. S. R. (1993). ANFIS: Adaptive network-based fuzzy inference systems. *IEEE Trans. Syst., Man. and Cybern*, 23, 665-685.
- Jang, J. S. R. and Sun, C.T. (1995). Neuro-Fuzzy modeling and control. *Proceedings of the IEEE*, 83(3), 378-406.
- Köker, R. (2013). A genetic algorithm approach to a neural-network-based inverse kinematics solution of robotic manipulators based on error minimization, *Information Sciences*, 222, 528-543.
- Köker, R., Öz, C., Çakar, T. and Ekiz, H. (2004). A study of neural network based inverse kinematics solution for a three-joint robot. *Robotics and Autonomous Systems*, 49, 227-234.
- Luan, F., Na, J., Huang, Y. and Gao, G. (2019). Adaptive neural network control for robotic manipulators with guaranteed finite-time convergence. *Neurocomputing*, 337, 153-164.
- Narayan, J. and Singla A. (2017). ANFIS Based Kinematic Analysis of a 4-DOFs SCARA Robot. 4th International Conference on Signal Processing, Computing and Control, 205-211, Solan, India.

- Sadhu, A.K., Konar, A., Bhattacharjee, T. and Das, S. (2018). Synergism of Firefly Algorithm and Q-Learning for Robot Arm Path Planning, *Swarm and Evolutionary Computation*, 43, 50-68.
- Song, C., Xie, S., Zhou, Z. and Hu, Y. (2015). Modeling of pneumatic artificial muscle using a hybrid artificial neural network approach. *Mechatronics*, 31, 124-131.
- Wang, Y., Shi, Y., Ding, D. and Gu, X. (2016). Double global optimum genetic algorithm–particle swarm optimization-based welding robot path planning, *Engineering Optimization*, 48, 299-316.
- Zheng, K., Zhang, Q., Hu, Y. and Wu, B. (2021). Design of fuzzy system-fuzzy neural network-backstepping control for complex robot system. *Information Sciences*, 546, 1230-1255.




## CHAPTER III

---


# INVESTIGATION OF COLOR REMOVAL FROM DAIRY INDUSTRY WASTE WATER USING NF270 MEMBRANE\*

**Ayman Alkhatab<sup>1</sup> & Duygu Kavak<sup>2\*</sup>**

<sup>1</sup>*Eskişehir Osmangazi University, Eskişehir, Turkey, e-mail: ayman89kat@gmail.com*

 ORCID 0000-0001-6504-9022

<sup>2</sup>*(Prof. Dr.), Eskişehir Osmangazi University, Eskişehir, Turkey  
e-mail: dbayar@ogu.edu.tr*

 ORCID 0000-0002-1189-3110

\* *Corresponding author: dbayar@ogu.edu.tr*

### 1. Introduction

In dairy industry technology, water is used throughout all steps including cleaning, sanitization, heating, cooling, and floor washing, generating large volumes of effluents which are mostly white waters. Dairy wastewater has high biochemical oxygen demand (BOI) and chemical oxygen demand (COD) contents, high levels of dissolved or suspended solids including fats, oils, and grease, nutrients such as ammonia or minerals and phosphates, milk components like lactose and proteins, and cleaning chemicals and detergents. Therefore, it must be treated by appropriate methods before being discharged (Kertész et al., 2015; Formentini-Schmitt et al., 2013). In case of insufficient treatment, dyes in the wastewater cause the formation of color and toxic substances in the receiving environment. Although color poses an aesthetic problem at first glance, it prevents photosynthesis by decreasing the light transmittance in natural waters when it reaches high levels (Çapar, 2004).

Various membrane processes have been proposed for dairy wastewater treatment to produce purified water for water reuse or recover nutrients (Ivnitsky et al. 2005; Boussu et al. 2007). Unlike conventional methods, membrane technology is tolerant to variable levels of pollutants in the upstream and is four times smaller than conventional wastewater treatment plant (Bae et al. 2003). Membrane technology, which is known to be environmental friendly, has ease of construction and control, low consumption of energy, no requirement of chemical

---

\* It is produced from the thesis titled "Treatment of Dairy Industry Wastewater by Nanofiltration Process".

substances to be added and is feasible for recovery of valuable metals (Licinio et al., 2015).

One-stage experiments such as ultrafiltration (UF), nanofiltration (NF) and reverse osmosis (RO) used in dairy wastewater treatment were investigated (Gong et al. 2012, Sarkar et al. 2006, Frappart et al. 2008). Among these membrane methods, nanofiltration uses membranes with very small pores (<1 nm) and requires operating pressures in the 10-50 bars range (Gherasim and Mikulášek 2014). There are two ways to operate nanofiltration process. While in dead-end filtration, all of the solution is directed towards the membrane area under applied pressure, in cross-flow filtration entire solution is directed parallel to the membrane surface (Tsibranska and Tytkowski 2013). The cross-flow is rather low to reduce concentration polarization and fouling as much as possible suitable (Koyuncu et al., 2018; Scott, 1995).

Nanofiltration process (NF) is used as a intermediate process of reverse osmosis and ultrafiltration which has advantages such as the effectiveness in removing the dissolved solutes, including multivalent ions and organic components with high molar mass with lower pressure requirements and higher fluxes than reverse osmosis. Studies indicate that NF is an effective process for secondary and tertiary treatment of wastewater in order to generate water for industrial, agricultural and indirect drinking reuse. However, evaluating the optimal operating conditions for each NF system allows enhancing the overall process performance, both in terms of permeation quality and fouling control quality (Andrade et al. 2014).

In this study, color removal from dairy industry wastewater was investigated by nanofiltration method. In order to determine the effect of filtration pressure (10, 15 and 20 bars) and feed temperature (25°C and 35°C) on color removal, dairy waste water was passed through NF270 membrane.

## **2. Materials and Methods**

In this study, thin film composite nanofiltration membrane NF270 was tested. NF270 is a flat sheet type membrane and the effective filtration area of this flat sheet membrane is 150 cm<sup>2</sup>. The properties of the membrane is given in Table 1.

Waste water used in this study was provided from the dairy industry in Eskişehir. The waste water obtained from the factory was taken the day before the experimental work was started and stored in the refrigerator in the laboratory to ensure that the properties of the waste water did not change. Table 2. shows the characteristics of the raw wastewater collected from a dairy plant.

Table 1. Properties of NF270 Membrane (Anonymous, 2020)

Membrane	NF270
Type	Organics Removal, Softening
pH Range	2-11
MgSO <sub>4</sub> Rejection	99,2%
Pore size/MWCO	200-400 Da
Flux (GFD)/psi	72-98/130
Polymer	Polyamide-TFC

Table 2. Properties of Wastewaters Used in Experimental Study

Parameters	Dairy wastewater
Max. Absorbance (nm)	320
A <sub>0</sub> (nm)	0.184
Conductivity (μs/cm)	1384
pH	6.90
COD (mg/L)	561
TSS (mg/L)	55

Sterlitech-SEPA CF cross-flow nanofiltration system was used in the experimental study. A schematic representation of the system is given in Figure 1. The cross-flow membrane filtration system was operated for 120 minutes for each pressure value of 10, 15 and 20 bar pressures for the treatment of collected dairy wastewater. The experiments were repeated at 25°C and 35°C. This system consists of a membrane module, feed tank, pressure pump, scales, flowmeter, computer, thermostat and necessary fasteners. The effective area of the membrane in the system is 150 cm<sup>2</sup> (Kavak, 2017a, Kavak, 2017b). Temperature control is provided by WiseCircu heater in the system. This heater is used to keep the waste water in the supply tank at the desired temperature levels. During each experiment, samples were taken from the permeate into UV cuvettes for 5, 15, 30, 45, 60, 90 and 120 minutes of filtration time. Color was analyzed using the Hach Lange DR 3900 UV-vis spectrophotometer at the λ<sub>max</sub> value of 320 nm.



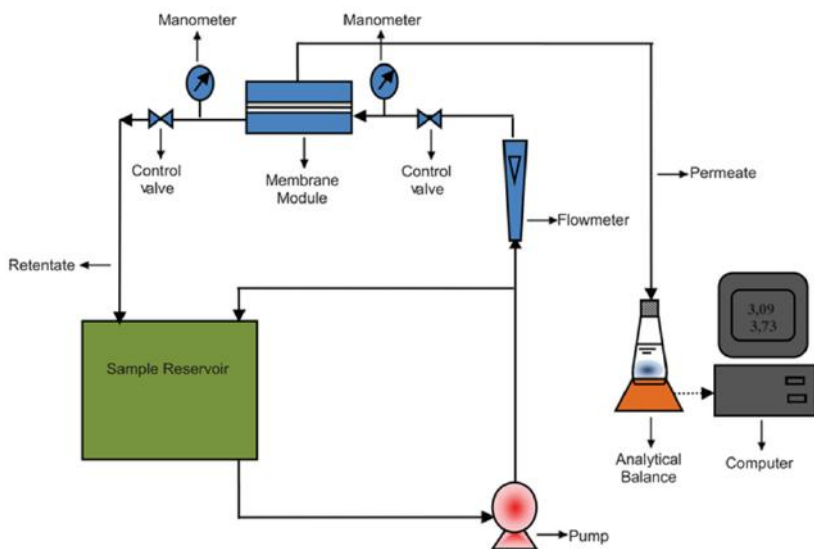


Figure 1: Schematic Diagram of the Cross-Flow NF Experimental Set Up.



(a)

(b)



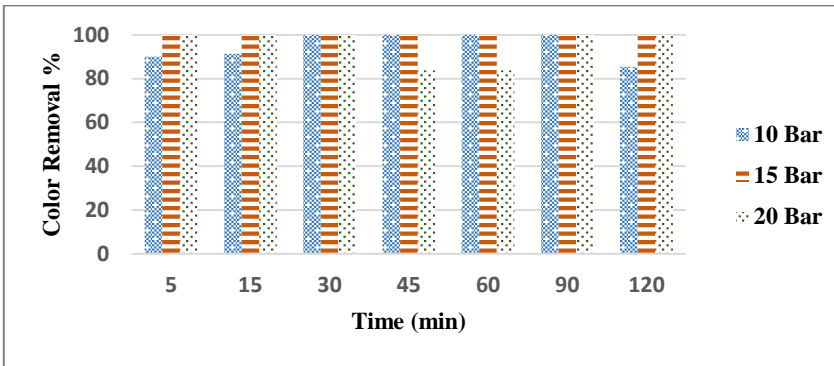
Figure 2: Cross Flow Membrane Filtration System

Color removal efficiency ( $E_F$ , %) was calculated by Eq. (1) based on the concentrations of a determined species in the permeate ( $C_P$ , mg/L) and in the feeding ( $C_F$ , mg/L).

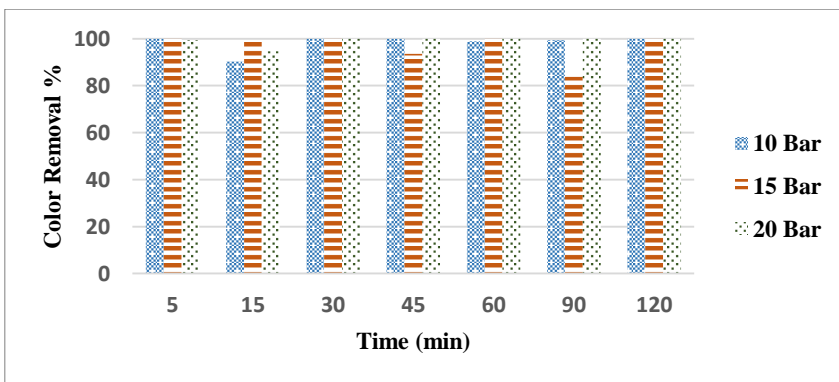
$$E_F = \frac{C_F - C_P}{C_F} \times 100 \quad (1)$$

### 3. Results and Discussion

The color removal performance of the NF270 membrane is shown in Fig.3. Very high percentage of color rejections were observed at all pressure and temperature values. At the end of 120 minutes color removal percentages were obtained as 85.3%, 100% and 100% for 10, 15 and 20 bar pressures at 25°C temperature, respectively. At 35°C temperature; color removal percentages were obtained as 100% for 10,15 and 20 bar pressures.



(a)



(b)

Figure 3: Color removal efficiencies of NF270 at pressures of 10, 15 and 20 bar for (a) 25°C and (b) 35°C

As can be seen from Fig. 3, At 25 °C; color removal increases with an increase in membrane pressure at the end of 120 minutes. The maximum color removal was obtained as 100% for 15 and 20 bar pressures.

At 10 bar; as the feed temperature was increased from 25°C to 35°C at the end of 120 minutes, the color removal increased from 85.3% to 100%, respectively. At 15 and 20 bar; with the increase of temperature, the color removal of NF270 membrane did not change. At 35°C, increasing pressure did not affect color rejection. Very high color removals were obtained under low pressure conditions. This result is very positive in terms of energy efficiency.

Ong et al. (2012) studied the decolorization and salt reduction of dyeing solution treated by NF270 and NF90 membranes. With respect to color removal, it is found that NF270 demonstrated greater stability in maintaining its separation efficiency (between 94 and 98% rejection) regardless of the feed properties and number of operation cycles (Ong et al., 2012).

#### **4. Conclusions**

In this study, performance of a NF270 membrane has been studied to treatment of dairy industry wastewater by cross-flow NF at different operating conditions. Effects of operating pressure and feed temperature were investigated on color removal. NF270 membrane used under different operating conditions of temperature and pressure showed high color removal efficiency. At the end of 120 minutes, the decolorization efficiency of NF270 membrane varied between 85.3-100%. The maximum color removal was obtained as 100% at 25°C and 35°C after 120 min of NF. According to the experimental results, NF270 membrane is efficient for color removal dairy industry wastewater.

#### **Acknowledgements**

In this study, devices and tools bought by Eskişehir Osmangazi University Research Foundation were used (Project Number: 201215031).

## References


- Andrade, L. H., Mendes, F. D. S., Espindola, J. C., and Amaral, M. C. S. (2014), Nanofiltration as tertiary treatment for the reuse of dairy wastewater treated by membrane bioreactor, *Separation and Purification Technology*, 126, 21–9.
- Anonymous (2020). <https://www.sterlitech.com>. Access Date 12.12.2020
- Bae, T. H., Han, S. S. and Tak, T. M. (2003). Membrane sequencing batch reactor system for the treatment of dairy industry wastewater. *Process Biochemistry*, 39, 221–231.
- Boussu, K., Kindts, C., Vandecasteele, C. and Van der Bruggen, B. (2007), Surfactant fouling of nanofiltration membranes: measurements and mechanisms, *Physical Chemistry Chemical Physics*, 8, 1836–1845.
- Çapar, G., Yetiş, Ü. ve Yılmaz, L. (2004), Halı boyama atıksularının membran prosesleri ile arıtımı, *Sosyal Siyaset Konferansları Dergisi*, 14(2) 9-15.
- Formentini-Schmitt, D.M, Alves, Á.C.D., Veit, M.T., Bergamasco, R., Vieira, A.M.S and Fagundes-Klen, M.R. (2013), Ultrafiltration Combined with Coagulation/Flocculation/Sedimentation Using *Moringa oleifera* as Coagulant to Treat Dairy Industry Wastewater, *Water Air Soil Pollution*, 224, 1682.
- Frappart, M., Jaffrin, M. and Ding, L. H. (2008), Reverse osmosis of diluted skim milk: comparison of results obtained from vibratory and rotating disk modules, *Separation and Purification Technology*, 60, 321–329.
- Gherasim, C-V. and Mikulášek, P. (2014), Influence of operating variables on the removal of heavy metal ions from aqueous solutions by nanofiltration, *Desalination*, 343, 67-74.
- Gong, Y.W, Zhang, H.X and Cheng, X.N. (2012), Treatment of dairywastewater by two-stage membrane operation with ultrafiltration and nanofiltration, *Water Science and Technology*, 65.5, 915-919.
- Ivnitsky, H., Katza, I., Minzc, D., Shimonid, E. and Dosoretz, C. G. (2005), Characterization of membrane biofouling in nanofiltration processes of wastewater treatment, *Desalination*, 185, 255–268.
- Kavak D. (2017a), Treatment of dye solutions by DL nanofiltration membrane, *Desalination and Water Treatment*, 69(1), 116-122.
- Kavak D. (2017b), Removal of Iron, Copper and Zinc Mixtures from Aqueous Solutions by Cross Flow nanofiltration, *Fresenius Environmental Bulletin*, 26(1a), 1101-1107.

- Kertész, S., Veszprémi, Á., László, Z., Csanádi, J., KeszthelyiSzabó, G and Hodúr, C. (2015), Investigation of module vibration in ultrafiltration, *Desalination and Water Treatment*, 55 2836–2842.
- Koyuncu, İ., vd., (2018), *Su/Atıksu Arıtılması ve Geri Kazanılmasında Membran Teknolojileri ve Uygulamalar*, Çevre ve Şehircilik Bakanlığı, s. 554.
- Licínio M. Gando-Ferreira Joana C. Marques and Quina M. J., (2015), Integration of ion-exchange and nanofiltration processes for recovering Cr(III) salts from synthetic tannery wastewater, *Environmental Technology*, 36(18) 2340–2348.
- Ong, C. S., Lau, W. J., and Ismail, A. F., 2012, Treatment of dyeing solution by NF membrane for decolorization and salt reduction, *Desalination and Water Treatment*, 50(1–3), 245–53.
- Sarkar, B., Chakrabarti, P.P., Vijaykumar, A. and Kale, V. (2006), Wastewater treatment in dairy industries-Possibility of reuse, *Desalination*, 195, 141–152.
- Scott, K., (1995), *Handbook of Industrial Membranes*, Elsevier Advanced Technology, p. 912.
- Tsibranska, I.H. and Tylkowski, B. (2013), Concentration of ethanolic extracts from *Sideritis SSP. L.* by nanofiltration: Comparison of dead-end and cross-flow modes, *Food and Bioproducts Processing* 91, 169-174.


# EFFECTS of INDUSTRIAL REFINING STAGES ON CORN OIL's QUALITY AND BIOACTIVE COMPONENTS DETERMINED USING GAS CHROMATOGRAPHY AND INDUCTIVELY COUPLED PLASMA ATOMIC EMISSION SPECTROSCOPY

**Erman Duman<sup>1</sup> & Musa Haslak<sup>2</sup>**

<sup>1</sup>(Asst. Prof. Dr.), Afyon Kocatepe University, Afyon, Turkey,  
e-mail: erman17@mynet.com.tr

 ORCID 0000-0003-3405-9572

<sup>2</sup>(Food Eng.), Afyon Kocatepe University, Afyon, Turkey,  
e-mail: Mshhaslak@hotmail.com

 ORCID 0000-0002-9811-2654

### 1. Introduction

To be able to use crude corn oil as an edible food, its ingredients, including free fatty acids, coloring agents, waxes, aldehydes, and ketones, must be extracted and the oil must then be refined. Refining is the process by which adhesive agents, soap, color substances, wax, aldehydes, and ketones in the crude oil are removed through treatments that neutralize, bleach, winterize, and deodorize the oil (El-Mallah, El-Shami, Hassanien, & Abdel-Razek, 2011; Yemişçiöğlü, Özdikicierler, & Gümüşkesen, 2016). During the chemical refining process, after removing the adhesive agents in the crude oil with water, the free fatty acidity in the oil is decreased by adding phosphoric acid and caustic, and then the color of the oil is lightened by bleaching the soil. Pearlite is then added while cooling to winterize the product. Finally, a vacuum is used at high temperatures to separate the aldehydes and ketones to deodorize the oil (Ortega-Garcia et al., 2006; Yıldırım, Erdoğan, & Yorulmaz, 2019).

The adhesive agents in the corn oil are composed of phospholipids; the coloring agents are carotene, xanthophyll, and chlorophyll. Waxy substances are formed by stearins, and effluvial substances are composed of aldehydes and ketones (Hamm, & Hamilton, 2000). It has been reported that pressure, temperature, steam flow, and time parameters applied during the refining process cause reductions in the oil's components (e.g.,

tocopherols, sterols, and vitamins) (Ruiz-Mhdez, Mirquez-Ruiz, & Dobarganes, 1997).

Viscosity, one physical property of vegetable oils, is an important parameter of the rheological properties in fluid foods such as oils, as well as in the design and process of reactors, and pipes (Abramovic, & Klofutar, 1998; Rodenbush, Hsieh, & Viswanath, 1999). Moreover, the fatty acid composition of vegetable oils is significant for human health and changes during the refining processes (Mohdaly et al., 2017). Some of these that affect health are oleic, linoleic, and linolenic unsaturated fatty acids, which are also available in corn oil (Karaca, ve Aytaç, 2011).

Furthermore, phytosterols, which are bioactive components in vegetable oils, protect the oils against oxidation and are also beneficial for human health. Phytosterols have antibacterial, antifungal, anti-inflammatory, and antitumor properties, and are also used to determine adulterations by using the sterol composition of vegetable oils (Yıldırım, Erdoğan, & Yorulmaz, 2019). In the neutralizing stage of refining, the sterols are substantially the non-saponifiers (Ferrari et al., 1996). The aim of this study was to determine the effects of the chemical refining stages (neutralizing, bleaching, winterizing, and deodorizing) on the quality characteristics and bioactive components of corn oil, such as free fatty acidity, peroxide value, iodine number, viscosity, color, saponification value, and the amount of unsaponifiable matter, and the composition of fatty acids, sterols, and minerals.

## **2. Materials and Methods**

### **2.1. Materials**

The corn oil samples used in this study were obtained from an oil refinery that is operated as a continuous system of neutralizing, bleaching, winterizing, and deodorizing stages, respectively, to the same samples of crude oil. Our study investigated the changes of nine properties comprising seven quality characteristics and different bioactive components in each of the five samples studied with three parallels after each stage.

### **2.2. Methods**

#### **2.2.1. Physico-Chemical Analyses**

Free fatty acidity, peroxide value, viscosity, saponification value, and the amount of unsaponifiable matter in the corn oil samples were analyzed according to American Oil Chemists' Society (AOCS) methods (Anonymous, 1990).

### **2.2.2. Color Analyses**

The corn oil samples used were filtered through filter paper and readings were done on a Lovibond PFX 880L tintometer using 1- and 5.25-inch cuvettes (Mehlenbacher, Walker, Walker R., & Link, 1985).

### **2.2.3. Analyses of Fatty Acid Composition**

The fatty acid compositions in the corn oil samples were determined based on the AOCS method. The samples were first treated with potassium hydroxide and n-heptane to esterify them after which 1  $\mu$ L was taken from the esterified samples. Gas chromatography (GC) using the Shimadzu GC-2025 (Shimadzu Corporation, Kyoto, Japan) was applied to determine the fatty acid composition after each refining stage under the following conditions (Hıŝıl, 2004): flame ionization detector, RTX-230; column, 60 m long with an inner diameter of 0.25 mm; and film thickness, 0.20  $\mu$ m. The column temperature was 180°C, the injection temperature was 200°C, and the detector temperature was 200°C. The flow of gases was as follows: carrier gas (N<sub>2</sub>), 30 mL/min; combustible gas (H<sub>2</sub>), 28 mL/min; dry air, 220 mL/min; and injection, 1  $\mu$ L.

### **2.2.4. Sterol Analyses**

The sterol composition in each corn oil sample was determined using the method of Lencher et al. (1999). The Shimadzu GC-2025 gas chromatography system (HP-5, column length, 30 m, column diameter, 0.25 mm, and film thickness, 0.25  $\mu$ m) was used. The flow rate of all gases was set at 45 mL/min. The column temperature was first increased from 0 to 60°C, then from 60 to 220°C, and the results were read at 220°C.

### **2.2.5. Mineral Substance Analyses**

Corn oil samples (0.5 g) were put into the heating container after which 15 mL pure HNO<sub>3</sub> was added and heated to 200°C in a microwave oven. The solution was then diluted with 100 mL ultrapure water and filtered through ashless filter paper (Macherey-Nagel MN 640W, black band, 110-mm diameter). The concentrations of the mineral substances were determined by reading the prepared samples on the ICP-AES (Varian Vista) (Skujins, 1998).

### **2.2.6. Statistical Analyses**

The data obtained in the study were analyzed using SPSS ver. 22.0 (IBM Corp., Armonk, NY, USA). In evaluating the data, the mean  $\pm$  standard deviation was used as the descriptive statistical result and the one-way analysis of variance and Duncan's multiple range test were used to compare quantitative continuous data between more than two independent groups (Püskülcü, & İkiç, 1998; Soysal, 1998).



### 3. Results and Discussion

The quality characteristics of the chemically refined corn oil are shown in Table 1. As seen in the table, free fatty acid content varied between 2.50 (crude oil) and 0.08% (deodorized oil) and peroxide values ranged from 3.13 meq O<sub>2</sub>/kg (crude oil) to 0 meq O<sub>2</sub>/kg (deodorized oil). We determined that the free fatty acid levels significantly decreased after the neutralizing stage and the peroxide value considerably decreased after the deodorizing stage. In a study by Aksoy (2015) the acidity in crude corn oil was determined to be 2.20, 0.12, 0.10, and 0.09% after the neutralizing, bleaching, winterizing, and deodorizing stages, respectively. In addition, Jung Yoon and Min (1989), Young (1983), Loft (1990), and Moo et al. (1995) have reported that free fatty acid levels and peroxide values decreased after vegetable oils were refined. It has been reported that the amount of oil loss increased with increasing free fatty acids during the refining process and the rancidity increased with increasing peroxide values (Tekin, 2005).

**Table 1.** Changes in the Quality Characteristics of Corn Oil During Chemical Refining.

Process Stages	Acidity (%)	Peroxide value (meqO <sub>2</sub> /kg)	Iodine number (mgI <sub>2</sub> /100 g)	Saponification (mgKOH/g)	Amount of unsaponifiable material (mgKOH/g)
Crude oil	2.50 <sup>a</sup> ± 0.03	3.13 <sup>a</sup> ± 0.30	119.94 <sup>c</sup> ± 0.71	207.48 <sup>a</sup> ± 0.03	1.91 <sup>a</sup> ± 0.03
Neutralizing	0.09 <sup>d</sup> ± 0.03	2.58 <sup>b</sup> ± 0.20	120.28 <sup>b c</sup> ±0.45	206.19 <sup>b</sup> ± 0.02	0.69 <sup>d</sup> ± 0.02
Bleaching	0.11 <sup>c</sup> ± 0.02	1.54 <sup>c</sup> ± 1.00	122.97 <sup>b</sup> ± 0.29	204.89 <sup>c</sup> ± 0.01	1.29 <sup>c</sup> ± 0.01
Winterizing	0.14 <sup>b</sup> ± 0.01	0.92 <sup>d</sup> ± 0.20	122.26 <sup>b</sup> ± 0.62	203.52 <sup>d</sup> ± 0.03	1.40 <sup>b</sup> ± 0.02
Deodorizing	0.08 <sup>d</sup> ± 0.02	0.0 <sup>e</sup> ± 0.00	124.29 <sup>a</sup> ± 0.88	202.88 <sup>c</sup> ± 0.04	0.23 <sup>c</sup> ± 0.03
Crude oil	2.50 <sup>a</sup> ± 0.03	3.13 <sup>a</sup> ± 0.30	119.94 <sup>c</sup> ± 0.71	207.48 <sup>a</sup> ± 0.03	1.91 <sup>a</sup> ± 0.03
Neutralizing	0.09 <sup>d</sup> ± 0.03	2.58 <sup>b</sup> ± 0.20	120.28 <sup>b c</sup> ±0.45	206.19 <sup>b</sup> ± 0.02	0.69 <sup>d</sup> ± 0.02
Process Stages	Viscosity (Pa-s)	Color			
		Red	Yellow	Blue	Dark
Crude oil	8.16 <sup>a</sup> ± 0.30	9.8 <sup>a</sup> (1'')	70.0 <sup>a</sup>	0.0 <sup>a</sup>	0.9 <sup>a</sup>
Neutralizing	7.25 <sup>b</sup> ± 0.20	3.6 <sup>c</sup> (1'')	70.0 <sup>a</sup>	0.0 <sup>a</sup>	0.1 <sup>bc</sup>

Bleaching	7.13 <sup>c</sup> ± 0.10	5.4 <sup>b</sup> (5.25'')	70.0 <sup>a</sup>	0.0 <sup>a</sup>	0.0 <sup>c</sup>
Winterizi ng	7.13 <sup>c</sup> ± 0.20	5.5 <sup>b</sup> (5.25'')	70.0 <sup>a</sup>	0.0 <sup>a</sup>	0.2 <sup>bc</sup>
Deodorizi ng	6.84 <sup>d</sup> ± 0.02	3.1 <sup>d</sup> (5.25'')	46.0 <sup>b</sup>	0.0 <sup>a</sup>	0.6 <sup>b</sup>

Notes: <sup>a-e</sup> values marked with different letters are statistically different from each other ( $p < 0.005$ ).

The viscosity of corn oil after refining varied between 8.16 (crude oil) and 6.84 Pa-s (deodorized oil) at 22°C. The highest change in viscosity was observed at the end of the neutralizing stage, and the crude corn oil became more fluid than that after this stage. In a study conducted by Nouredini et al. (1992) viscosity levels changed in the refined corn oil with temperature changes and were reported to be 52.3, 30.8, 22.7, 15.7, and 9.28 Pa-s at 23.9, 37.8, 48.9, 60, and 62.2°C, respectively. In the same study, the viscosity values for refined soybean oil were determined to be 54.3, 31.8, 23.3, 16.1, and 9.51 Pa-s, respectively, at the same temperatures. In another study on the chemical refining process of sunflower oil, viscosity levels were reported to be 7.03, 7.18, 8.00, 6.67, and 6.58 Pa-s for crude, neutralized, bleached, winterized, and deodorized oils, respectively (Ergönül, 2013).

Color is an important parameter in vegetable oil technology. The color values of refined corn oil were determined to be 9.8 red, 70.0 yellow, and 0.9 dark for crude oil and 3.1 red, 46 yellow, and 0.6 dark for deodorized oil; the color of the corn oil was the lightest at the end of bleaching stage. On the other hand, Aksoy (2015) has examined the changes in red corn oil during the refining stages and reported it as 16 in crude oil, 9 after neutralizing, 5.2 after bleaching, 5 after winterizing, and 2.7 after deodorizing.

The saponification number for corn oil varied between 207.48 (crude oil) and 202.88 mg KOH/g (deodorized oil) and decreased gradually during the refining process. The amount of unsaponifiable material increased and decreased within a range of 1.91 (crude oil) and 0.23 g/kg (deodorized oil) depending on the refining stage. The highest decrease in the amount of unsaponifiable corn oil was observed during the deodorizing stage. It was stated that during vegetable oil refining, the free fatty acid, peroxide value, and saponification number decreased, while the amount of unsaponifiable material increased from the crude to the refined oil (Onyema, & Ibe, 2016).

As seen in Table 2, when examining the changes in fatty acid composition during the corn oil refining, the total saturated fatty acids varied between 13.77 (crude oil) and 12.44% (deodorized oil), and total unsaturated fatty acids varied between 86.22 (crude oil) and 87.55%

(deodorized oil). Palmitic and stearic saturated fats and oleic and linoleic unsaturated fats were the dominant fatty acids in corn oil. It was determined that the fatty acid composition of the corn oil did not change with refining. In their study on corn oil, Ferrari et al. (1996) have determined that the palmitic acid concentration is 13.1, 12.4, 12.8, and 12.5% at the neutralizing, bleaching, winterizing, and deodorizing stages, respectively. The palmitoleic acid content was calculated as 0.2% at all stages of refining. Among the unsaturated fatty acids, the amount of oleic acid was determined to be 34.1% in the crude oil and 34.6, 34.6, 34.9, and 34.8% at the neutralizing, bleaching, winterizing, and deodorizing stages respectively.

**Table 2.** Changes in the Fatty Acid Concentrations of Corn Oil During Chemical Refining.

SFA	Crude oil (%)	Neutralizing (%)	Bleaching (%)	Winterizing (%)	Deodorizing (%)
Myristic	0.03	0.03	0.03	0.03	0.04
Palmitic	11.15	11.08	10.01	10.27	9.44
Stearic	1.98	1.97	2.33	2.23	2.41
Arachidic	0.43	0.43	0.38	0.39	0.35
Lignoceric	0.18	0.15	0.16	0.16	0.17
Σ	13.77 <sub>a</sub>	13.67 <sup>a</sup>	12.94 <sup>b</sup>	13.10 <sup>ab</sup>	12.44 <sup>c</sup>
<b>MUFA</b>					
Palmitoleic	0.06	0.06	0.06	0.06	0.05
Heptadecanoic	0.04	0.04	0.03	0.04	0.03
Oleic	33.23	33.22	31.38	31.91	30.49
Nervonic	0.01	0.01	0.01	0.01	0.01
<b>PUFA</b>					
Linoleic	52.70	52.78	55.25	54.59	56.58
Linolenic	0.01	0.09	0.09	0.08	0.01
Cis-11,14-eicosadienoic	0.09	0.12	0.25	0.21	0.32
Arachidic	0.05	0.05	0.05	0.05	0.04
Σ	86.22 <sub>c</sub>	86.32 <sup>bc</sup>	87.06 <sup>a</sup>	86.90 <sup>b</sup>	87.55 <sup>a</sup>

Notes: <sup>a-c</sup> values marked with different letters are statistically different from each other (p < 0.005).

SFA: Saturated Fatty Acids, MUFA: Monounsaturated Fatty Acids, PUFA: Polyunsaturated Fatty Acids

It has been reported in studies conducted on corn and other vegetable oils that there is no significant change in the fatty acid composition during the refining process (Wilding, Rice, & Mattil, 1963; Morrison, & Robertson, 1978; Jinsuk, & Seung, 1993; Çalışkan, 2008; Aksoy, 2015). On the other hand, it has been reported that the total amount of monounsaturated fatty acids increases and the amount of saturated fatty acids decreases as a result of the refining process (Taşan, 1999; Mohdaly et al., 2017).

**Table 3.** Changes in the Sterol Composition of Corn Oil During Chemical Refining.

Sterol Composition	Crude Oil	Neutralizing	Bleaching	Winterizing	Deodorizing
1- Campesterol (%)	25.87 <sub>b</sub>	27.25 <sup>a</sup>	21.73 <sup>c</sup>	25.46 <sup>b</sup>	9.00 <sup>d</sup>
2- Stigmasterol (%)	6.46 <sup>c</sup>	6.92 <sup>b</sup>	6.13 <sup>c</sup>	6.76 <sup>b</sup>	12.63 <sup>a</sup>
3- $\Delta$ 5.23-Stigmastadienol (%)	nd.	nd.	nd.	nd.	0.80 <sup>a</sup>
4-Cholesterol (%)	0.45 <sup>c</sup>	0.43 <sup>c</sup>	0.45 <sup>c</sup>	0.53 <sup>b</sup>	0.84 <sup>a</sup>
5- $\beta$ -sitosterol (%)	67.21 <sub>b</sub>	65.39 <sup>c</sup>	61.25 <sup>d</sup>	67.22 <sup>b</sup>	71.87 <sup>a</sup>
6- $\Delta$ 5-Avenasterol (%)	nd.	nd.	4.01 <sup>a</sup>	nd.	nd
7- $\Delta$ 5.24-Stigmastadienol (%)	nd.	nd.	0.60 <sup>a</sup>	nd.	nd.
8- $\Delta$ 7-Stigmastenol (%)	nd.	nd.	5.08 <sup>a</sup>	nd.	4.82 <sup>b</sup>
9- $\Delta$ 7-Avenasterol (%)	nd.	nd.	0.72 <sup>a</sup>	nd.	nd.

Notes: <sup>a-d</sup> values marked with different letters are statistically different from each other ( $p < 0.005$ ). nd. Not detected.

As seen in Table 3, campesterol, stigma sterol, cholesterol, and  $\beta$ -sitosterol were determined at all stages of the refining process and that  $\Delta 5.23$ -stigmastadienol,  $\Delta 5$ -avenasterol,  $\Delta 5.24$ -stigmastadienol,  $\Delta 7$ -stigmastenol, and  $\Delta 7$ -avenasterol were determined in different amounts at different stages of the refining process. The concentration of  $\beta$ -sitosterol was highest, changing from 67.21 (crude oil) to 71.87% (deodorized oil). The chemical refining process was statistically ( $p < 0.005$ ) effective on the sterol composition of the corn oil. The studies in the literature have indicated that the refining process has affected the sterol composition of vegetable oils. The results of a study conducted on corn, soybean, and rapeseed oil showed that the total amount of sterols in all three oils decreases by 36, 18, and 24%, respectively, as a result of the refining process (Ferrari et al., 1996).

**Table 4.** Changes in the Mineral Composition of Corn Oil During Chemical Refining.

Mineral	Crude Oil (ppm)	Neutralization (ppm)	Bleaching (ppm)	Winterization (ppm)	Deodorization (ppm)
Li	0.028 <sup>a</sup>	0.000 <sup>b</sup>	0.000 <sup>b</sup>	0.000 <sup>b</sup>	0.000 <sup>b</sup>
B	0.000 <sup>c</sup>	0.040 <sup>b</sup>	0.110 <sup>a</sup>	0.123 <sup>a</sup>	0.080 <sup>b</sup>
Na	0.000 <sup>e</sup>	764.74 <sup>a</sup>	109.61 <sup>d</sup>	141.75 <sup>b</sup>	130.68 <sup>c</sup>
Mg	16.693 <sup>a</sup>	6.773 <sup>b</sup>	2.145 <sup>c</sup>	1.976 <sup>d</sup>	1.790 <sup>e</sup>
Al	0.000 <sup>e</sup>	0.446 <sup>d</sup>	1.133 <sup>c</sup>	2.212 <sup>a</sup>	1.163 <sup>b</sup>
Si	20.312 <sup>e</sup>	37.30 <sup>d</sup>	39.15 <sup>c</sup>	43.84 <sup>a</sup>	39.78 <sup>b</sup>
P	165.41 <sup>e</sup>	1029.32 <sup>d</sup>	1084.56 <sup>b</sup>	1202.45 <sup>a</sup>	1046.08 <sup>c</sup>
K	19.451 <sup>a</sup>	0.000 <sup>b</sup>	0.000 <sup>b</sup>	0.000 <sup>b</sup>	0.000 <sup>b</sup>
V	0.000 <sup>b</sup>	0.001 <sup>a</sup>	0.000 <sup>b</sup>	0.001 <sup>a</sup>	0.00 <sup>b</sup>
Cr	0.000 <sup>e</sup>	0.018 <sup>d</sup>	0.040 <sup>b</sup>	0.066 <sup>a</sup>	0.039 <sup>c</sup>
Mn	0.283 <sup>a</sup>	0.062 <sup>c</sup>	0.081 <sup>b</sup>	0.081 <sup>b</sup>	0.043 <sup>d</sup>
Co	0.000 <sup>c</sup>	0.000 <sup>c</sup>	0.002 <sup>b</sup>	0.011 <sup>a</sup>	0.002 <sup>b</sup>
Cu	0.045 <sup>b</sup>	0.000 <sup>c</sup>	0.000 <sup>c</sup>	0.049 <sup>b</sup>	0.071 <sup>a</sup>
Ga	0.000 <sup>a</sup>	0.000 <sup>a</sup>	0.000 <sup>a</sup>	0.001 <sup>a</sup>	0.001 <sup>a</sup>
As	0.001 <sup>c</sup>	0.001 <sup>c</sup>	0.011 <sup>b</sup>	0.020 <sup>a</sup>	0.013 <sup>b</sup>

Se	12.94 <sup>b</sup>	12.07 <sup>b</sup>	11.99 <sup>c</sup>	14.40 <sup>a</sup>	11.98 <sup>c</sup>
Rb	0.006 <sup>a</sup>	0.000 <sup>a</sup>	0.000 <sup>a</sup>	0.000 <sup>a</sup>	0.000 <sup>a</sup>
Sr	0.018 <sup>b</sup>	0.022 <sup>a</sup>	0.024 <sup>a</sup>	0.023 <sup>a</sup>	0.025 <sup>a</sup>
Pd	0.000 <sup>b</sup>	0.000 <sup>b</sup>	0.000 <sup>b</sup>	0.002 <sup>a</sup>	0.000 <sup>b</sup>
Ag	0.000 <sup>c</sup>	0.000 <sup>c</sup>	0.000 <sup>c</sup>	0.021 <sup>a</sup>	0.003 <sup>b</sup>
Cd	0.054 <sup>a</sup>	0.027 <sup>b</sup>	0.000 <sup>c</sup>	0.000 <sup>c</sup>	0.000 <sup>c</sup>
In	0.000 <sup>d</sup>	0.000 <sup>d</sup>	0.048 <sup>b</sup>	0.063 <sup>a</sup>	0.043 <sup>c</sup>
Sn	0.000 <sup>e</sup>	4.998 <sup>d</sup>	32.42 <sup>b</sup>	40.34 <sup>a</sup>	25.78 <sup>c</sup>
Sb	0.000 <sup>e</sup>	0.002 <sup>b</sup>	0.002 <sup>b</sup>	0.021 <sup>a</sup>	0.001 <sup>c</sup>
Te	0.000 <sup>b</sup>	0.008 <sup>a</sup>	0.000 <sup>b</sup>	0.000 <sup>b</sup>	0.000 <sup>b</sup>
Ba	0.000 <sup>e</sup>	0.004 <sup>c</sup>	0.022 <sup>b</sup>	0.046 <sup>a</sup>	0.024 <sup>b</sup>
Pb	0.000 <sup>d</sup>	0.000 <sup>d</sup>	0.005 <sup>c</sup>	0.055 <sup>a</sup>	0.014 <sup>b</sup>

Notes: <sup>a-c</sup> values marked with different letters are statistically different from each other ( $p < 0.001$ ).

As seen in Table 4, the elements with the highest composition in the corn oil samples were Mg, Si, P, K, and Se as a result of the chemical refining process and their compositions were 16.693 (crude oil) and 1.790 ppm (deodorized oil) for Mg, 20.312 (crude oil) and 39.78 ppm (deodorized oil) for Si, 165.41 (crude oil) and 1046.08 ppm (deodorized oil) for P, 19.451 (crude oil) and 0 ppm (deodorized oil) for K, and 12.94 (crude oil) and 11.98 ppm (deodorized oil) for Se; therefore, the chemical refining process was statistically significant ( $p < 0.001$ ) on the mineral composition in the corn oil. Ostric et al. (1980) have reported that the amounts of Fe and Cu in sunflower oil are 0.75 and 0.70 ppm after neutralizing and 0.70 and 0.63 ppm after bleaching, respectively. Aksoy (2015) has examined Na, Mg, K, P, Ca, and Fe levels based on the refining stages and determined them to be 37.75, 21.15, 12.97, 107.36, 107.48, and 4.68 ppm, respectively, in the crude oil. These values were found to be 9.84, 1.12, 1.14, 1.04, 31.13, and 3.12 ppm, respectively, after the neutralizing stage; 9.69, 0.29, 6.38, 0.91, 36.61, and 1.46 ppm, respectively, after the bleaching stage; 8.24, 0.91, 10.27, 1.09, 54.80, and 0.77 ppm, respectively, after the winterizing stage; and 8.26, 1.38, 9.82, 0.20, 8.11, and 0.54 ppm, respectively, after the deodorizing stage. Several researchers who have determined the effect of the refining process on the mineral composition of corn and other oils (Crapiste, Brevedan, & Carelli, 1999; Dimic, Karlovic, & Turkulov 1994; Kamyshin & Derevyanko, 1972:

İskander, 1993: Yüksel, 2010: Lepri et al., 2011: De Leonardis, Macciola, & Felice 2000) have indicated that the levels of minerals in the oils change with the refining process and that this change is the result of the chemical structure of the oilseed, the contents of the wash water, and the process applied during refining.

During the refining stages of the corn oil, acidity, peroxide value, viscosity, color, and saponification number decreased, while the number of unsaponifiable materials increased or decreased depending on the refining stage. No dominant changes in fatty acid composition were determined. During the refining stages, palmitic, stearic, and oleic acids were observed in higher amounts in the corn oil compared to levels of other fatty acids. Sterol levels in the corn oil varied depending on the refining stage. Accordingly, stigmasterol and  $\beta$ -sitosterol contents increased, while campesterol decreased. Mg, K, Mn, Se, and Rb concentrations decreased in the refined corn oil, while Na, Al, Si, P, Cr, Sr, and Ba increased. According to our results, the chemical refining process had different effects on the quality and bioactive components of corn oil, such as the acidity, peroxide value, viscosity, color, saponification number, and on the number of unsaponifiable materials, sterols, and minerals.

### **Acknowledgments**

This article has been produced from the titled master's thesis ‘‘The Detection of Impurities in Nanoscale and Physico-Chemical Changes Occuring in Refined Stages Of Corn Oil’’by Food Engineer Musa Haşlak at Afyon Kocatepe University, Institute of Science. Since this study is supported by the project numbered AKÜ BAP 18th Science. 35, the authors have thanks applied to Afyon Kocatepe University BAP Coordinatorship and Dr. Sabire Duman for her support

## Refecenses

- Abramovič, H., & Klofutar, C. (1998). The temperature dependence of dynamic viscosity for some vegetable oils. *Acta Chimica Slovenica*, 1(45), 69-77.
- Aksoy, A. S. (2015). Kimyasal rafinasyonun mısır yağının bazı element içerikleri ile bazı kalite özelliklerine etkileri (Master's thesis, Namık Kemal Üniversitesi).
- Anonymous, AOCS, (1990). Official methods and recommended practices, 4th ed vol.1, American Oil Chemists' Society Champaign.
- Crapiste, G. H., Brevedan, M. I., & Carelli, A. A. (1999). Oxidation of sunflower oil during storage. *Journal of the American Oil Chemists' Society*, 76(12), 1437.
- Çalışkan, T. Y., Tekin, A. T. D. Rafinasyon İşlemlerinin Bitkisel Yağlarda İzomeri Oluşumu ve Oksidatif Stabilité Üzerine Etkisi (*Doctoral Dissertation*, Ankara Üniversitesi Fen Bilimleri Enstitüsü Gıda Mühendisliği Anabilim Dalı).
- De Leonardis, A., Macciola, V., & De Felice, M. (2000). Copper and iron determination in edible vegetable oils by graphite furnace atomic absorption spectrometry after extraction with diluted nitric acid. *International journal of food science & technology*, 35(4), 371-375.
- Dimic, E., Karlovic, D. J., & Turkulov, J. (1994). Pretreatment efficiency for physical refining of sunflowerseed oil. *Journal of the American Oil Chemists' Society*, 71(12), 1357-1361.
- El-Mallah, M. H., El-Shami, S. M., Hassanien, M. M. M., & Abdel-Razek, A. G. (2011). Effect of chemical refining steps on the minor and major components of cottonseed oil. *Agric. Biol. JN Am*, 2, 341-349.
- Ergonul, P. G. (2013). The effect of refining step on the changes in viscosity values of vegetable oils. *Pak. J. Agri. Sci*, 50(3), 421-425.
- Erickson, D. R. (1990). Edible Fats and Oils Processing Basic Principles and Modern Practices. In *World Conference on Edible Fats and Oils Processing: Basic principles and Modern Practices Oct 1-2, 1989Maastricht-Holanda* (No. L-0200). AOCS.
- Ferrari, R. A., Schulte, E., Esteves, W., Brühl, L., & Mukherjee, K. D. (1996). Minor constituents of vegetable oils during industrial processing. *Journal of the American Oil Chemists' Society*, 73(5), 587-592.
- Hamm, W, Hamilton, R. J. (2000). Edible oil processing, Sheffield Academic Press, Sheffield.



- Han, J. S., & Ahn, S. Y. (1993). Effects of oil refining processes on oil characteristics and oxidation stability of sesame oil. *Applied Biological Chemistry*, 36(4), 284-289.
- Hışıl, Y. (2004). Enstrümantal Gıda Analizleri. Ege Üniversitesi Mühendislik Fakültesi İzmir-39s.
- Im, M. H., Choi, J. D., & Choi, K. S. (1995). The oxidation stability and flavor acceptability of oil from roasted soybean. *Applied Biological Chemistry*, 38(5), 425-430.
- Iskander, F. Y. (1993). Determination of seventeen elements in edible oils and margarine by instrumental neutron activation analysis. *Journal of the American Oil Chemists' Society*, 70(8), 803-805.
- Jung, M. Y., Yoon, S. H., & Min, D. B. (1989). Effects of processing steps on the contents of minor compounds and oxidation of soybean oil. *Journal of the American Oil Chemists' Society*, 66(1), 118-120.
- Kamyshin, K., Derevyanko, K. (1972). Changes in ash content of sunflower seed oil during refining, *Maslozhirovaya Promyshlennost*, 37 (7), 12-14.
- Karaca, E., & Aytaç, S. (2007). Yağ bitkilerinde yağ asitleri kompozisyonu üzerine etki eden faktörler. *Anadolu Tarım Bilimleri Dergisi*, 22(1), 123-131.
- Lechner, M, Reiter, B, Lorbeer, E. (1999). Determination of tocoferols and sterols in vegetable oils by solid phase extraction and subsequent capillary gas chromatography analysis, *J. Chrom, A*, 857, 231-238.
- Lepri, F. G., Chaves, E. S., Vieira, M. A., Ribeiro, A. S., Curtius, A. J., DeOliveira, L. C., & DeCampos, R. C. (2011). Determination of trace elements in vegetable oils and biodiesel by atomic spectrometric techniques—a review. *Applied Spectroscopy Reviews*, 46(3), 175-206.
- Mehlenbacher, V. C., Walker, R.O., Walker, R. and Link, W. E. (1985). Lovibond Method. official methods and recommended practices of the American Oil Chemists Society.
- Mohdaly, A. A. E. R., Seliem, K. A. E. H., Maher, A. E. M., EL-Hassan, A., Mahmoud, A. A. T. (2017). Effect of refining process on the quality characteristics of soybean and cotton seed oils. *International Journal of Current Microbiology and Applied Sciences* 6, 207-222.
- Morrison, W. H., & Robertson, J. A. (1978). Hydrogenated sunflowerseed oil: Oxidative stability and polymer formation on heating. *Journal of the American Oil Chemists' Society*, 55(5), 451-453.

- Noureddini, H., Teoh, B. C., & Davis Clements, L. (1992). Viscosities of vegetable oils and fatty acids. *Journal of the American Oil Chemists' Society*, 69(12), 1189-1191.
- Onyema, C. T., & Ibe, K. K. (2016). Effects of refining processes on the physicochemical properties of some selected vegetable oils. *Chemical Science International Journal*, 1-7.
- Ortega-García, J., Gámez-Meza, N., Noriega-Rodriguez, J. A., Dennis-Quiñonez, O., García-Galindo, H. S., Angulo-Guerrero, J. O., & Medina-Juárez, L. A. (2006). Refining of high oleic safflower oil: effect on the sterols and tocopherols content. *European Food Research and Technology*, 223(6), 775-779.
- Ostrić-Matijasević, B., Turkulov, J., & Karlović, D. (1980). Quality of sunflower oil bleached during deodorization. *Journal of the American Oil Chemists Society*, 57(10), 323-325.
- Püskülcü, H, İkiz, F. (1998). Introduction to statistic, Bornova, Bilgehan Press.
- Rodenbush, C. M., Hsieh, F. H., & Viswanath, D. S. (1999). Density and viscosity of vegetable oils. *Journal of the American Oil Chemists' Society*, 76(12), 1415-1419.
- Ruiz-Méndez, M. V., Márquez-Ruiz, G., & Dobarganes, M. C. (1997). Relationships between quality of crude and refined edible oils based on quantitation of minor glyceridic compounds. *Food chemistry*, 60(4), 549-554.
- Skujins, J. (1998). Handbook for ICP-AES (Varian-Vista), A short Guide to Vista Series ICP-AES Operation, Switzerland.
- Soysal, M. İ. (1998). Biometrinin Temel Prensipleri. Trakya Üni. Ziraat Fak. Yayınları, Tekirdağ.
- Taşan, M. (1999). Farklı rafinasyon yöntemlerinin (kimyasal ve fiziksel) ayçiçek yağı bileşimine ve oksidatif stabilitesi üzerine etkileri, Doktora Tezi, Trakya Üniversitesi, Fen Bilimleri Enstitüsü, 1-51 s., Tekirdağ.
- Tekin, A. (2005). Margarinler ve bitkisel yağların kalite kriterleri, Dünya Ticaretinde Palm Yağının Yeri ve Önemi Konferansı, Malasian Palm Oil Promotion Council, Ankara. (2005).
- Wilding, M. D., Rice, E. E., & Mattil, K. F. (1963). The effect of processing conditions upon the nutritional quality of vegetable oils. *Journal of the American Oil Chemists' Society*, 40(2), 55-57.


- Yemiřciođlu, F., Özdikicierler, O., & Gümüřkesen, A. S. (2016). Bitkisel Yađ Rafinasyonunda Yeni Bir Yaklařım: Minimal Rafinasyon. *Academic Food Journal/Akademik GIDA*, 14(2).
- Yıldırım, A., Erdoğan, Ö., & Yorulmaz, A. Rafinasyon İşlem Basamaklarının Ayçiçek Yađının Yađ Asidi, Sterol Ve Uçucu Bileřen Kompozisyonuna Etkisi. *Çukurova Tarım Ve Gıda Bilimleri Dergisi*, 34(2), 109-118.
- Young, F. V. K. (1983). Palm kernel and coconut oils: analytical characteristics, process technology and uses. *Journal of the American Oil Chemists' Society*, 60(2Part2), 374-379.
- Yüksel, E. (2010). Çeřitli rafine bitkisel yađlarda ve kahvaltılık margarinlerde bazı element içeriklerinin belirlenmesi (*Master's thesis*), Namık Kemal Üniversitesi

## CHAPTER V


# TEMPERATURE CHARACTERIZATION OF LIGHT SOURCES SUCH AS LOW-POWER LASER, INTENSE PULSED LIGHT (IPL) AND LIGHT EMITTING DIODE (LED) USED FOR THERAPEUTIC PURPOSES ON TISSUE-MIMICKING MATERIALS

Hüseyin Okan Durmuş<sup>1,\*</sup> & Emel Çetin Arı<sup>2</sup> & Baki Karaböce<sup>3</sup>  
MirHasan Yu. Seyidov<sup>4</sup>


<sup>1</sup>*Gebze Technical University, Physics Department,  
Gebze-Kocaeli, Turkey, e-mail: hokandurmus@gtu.edu.tr,*

 ORCID 0000-0003-0973-0643


<sup>2</sup>*(Dr.), TUBITAK National Metrology Institute (TUBITAK UME),  
Medical Metrology Laboratory, Kocaeli, Turkey, e-mail: emel.cetin@tubitak.gov.tr,*

 ORCID 0000-0003-1144-1584

<sup>3</sup>*(Assoc. Prof. Dr.), TUBITAK National Metrology Institute (TUBITAK UME),  
Medical Metrology Laboratory, Kocaeli, Turkey, e-mail: baki.karaboce@tubitak.gov.tr,*

 ORCID 0000-0002-5814-3157

<sup>4</sup>*(Prof. Dr.), Gebze Technical University, Physics Department,  
Gebze-Kocaeli, Turkey, e-mail: smirhasan@gtu.edu.tr*

 ORCID 0000-0003-4901-7674

**\*Corresponding author:** hokandurmus@gtu.edu.tr, huseyinokan.durmus@tubitak.gov.tr

### 1. Introduction

Phantoms are artificial materials that simulate human tissues, defined in the literature as tissue-mimicking materials (TMMs) or tissue-equivalent materials. From the research and development phase of new systems to the calibration and quality control of existing devices, tissue-simulating objects are required for defined test conditions. These "phantoms" or standards are fixed measurement objects that exhibit defined properties in the dimensions to be measured and always give the same result. Besides, phantoms are commonly used to develop and characterize imaging systems or algorithms in medical imaging. Although phantoms are frequently used in ionizing radiation and ultrasonic imaging, they are now used extensively in scientific researches, such as magnetic resonance imaging, photoacoustic imaging, biophotonics, etc. due to their

ability to simulate biological soft tissues (Cook, Bouchard, and Emelianov 2011; Culjat et al. 2010; Netz, Toelsner, and Bindig 2011).

In the medical field, lasers are used in a wide variety of diagnoses and treatments. In surgical treatment applications such as incision, burning, or destroying tissue, lasers use an intense beam of light, while low-intensity laser treatments include healing practices. A few examples of laser applications in the medical field can be given as follows:

- removal of spots, tattoos and unwanted hair on the body,
- removal of acne scars and wrinkles on the body,
- skin rejuvenation and skin renewal,
- cleaning of tooth decay and teeth whitening,
- removal of tumorous tissues,
- correction of astigmatism, myopia and hyperopia in the eye,
- lithotripsy (breaking of kidney stones),
- physical therapy etc.

Biostimulation lasers, also called as Low-Level Laser Therapy (LLLT), cold lasers, soft lasers, or laser acupuncture devices, were approved by the FDA (U.S. Food and Drug Administration) as adjunctive devices for the temporary relief of pain (Biostimulation Laser).

LLLT or photobiomodulation (PBM) is a relatively novel technique, which is noninvasive, very low cost, effective, with no evident side effects, and a non-pharmacological adjuvant or complementary therapy (Elmer 2019; Li, Wang, and Cao 2019; Madani et al. 2020; Mazur 2019; Moghadam 2019; Poojar et al. 2017; Rigonato-Oliveira et al. 2019; Sinesi et al. 2019).

LLLT involves the local application of a high-density, monochromatic, narrow-band light source, works in the range of 390 nm and 1100 nm wavelength (visible to the near infrared spectral band) and power as 1 mW and 500 mW without generation of heat. In contrast to many other medical laser treatments, such as operative lasers, LLLT does not emit heat, sound, or vibration. Instead of producing a thermal effect, it is assumed that LLLT works by stimulating photochemical reactions in cells. Besides, LLLT irradiation refers to the use of red-beam (Diker et al. 2019; Ma and Xu 2019; Musstaf, Jenkins, and Jha 2019; Olejnik, Ślebioda, and Dorocka-Bobkowska 2019).

A wide variety of therapy lasers are used in medical treatments. For example, LLLT is a photobiostimulation therapy for treating a wide variety of conditions in physiotherapy practice and is preferred because of its effectiveness, noninvasive, safe, and cost effective. LLLT modulates biological processes, including differentiation, cell proliferation, cell

growth, apoptosis, and angiogenesis. It also helps improve blood flow and collagen synthesis. Increased microcirculation and increased ATP, RNA and DNA production (hence improving cellular oxygenation, nutrition and regeneration) are the most prominent bio-stimulatory effects of LLLT (Durmus et al. 2020).

Intense Pulsed Light (IPL) is a non-thermal electro-optical technology that works from UV to IR in a broad range and emits short-lived and high-power pulses (Jeon et al. 2019). IPLs emit incoherent polychromatic light, usually between 400 nm and 1200 nm. Because of this property, it can operate with distinct therapeutic alternatives on distinct chromophores (González-Rodríguez and Lorente-Gual 2015). IPL is a technique that is non-laser (Daoud et al. 2019). To generate light pulses of a specified length, intensity and spectral distribution, IPL devices use flash lamps, computer-controlled power supplies and bandpass filters (Ciocon, Boker, and Goldberg 2009). Various lasers have been introduced for different applications in the early 1990s, from tattoo removal, wound healing, cosmetic rejuvenation to epilation in the dermatology field. Unlike a monochromatic laser, the IPL is a high-power broadband light source (Ash et al. 2017). It appeared as an alternative to existing laser sources in the mid-1990s. However, broadband IPL technology emerged as a strong competitor in the new millennium and challenged the laser's market dominance (Ash et al. 2017). In general, IPL technologies give equal results to laser treatments (Goldberg 2012). There are many variations between lasers and IPL, whereas a laser emits monochromatic light, an IPL emits a variety of wavelengths from about 250 nm to 1200 nm, and the cutting filters subsequently reduce this variety (Stangl, Hadshiew, and Kimmig 2008). IPL is one of the non-invasive optical medical devices that use a light source for skin treatment for infection or vascular and pigmented lesion (Lee et al. 2017). The method of the IPL is known as photothermolysis selective (Soltes 2010). IPL light can be selectively absorbed into the skin by a specific chromophore, destroying the destination chromophore and leaving the surrounding tissues unharmed (Gold 2007). Since various wavelengths are transferred, the same light exposure can be applied to various chromophores such as hemoglobin, melanin, water and collagen. For example, melanin absorbs light wavelengths between 250 nm and 1200 nm, oxyhemoglobin absorption peaks are 418 nm, 542 nm and 577 nm, and collagen foams absorb light between 400 nm and 600 nm (Ciocon, Boker, and Goldberg 2009). Melanin and other chromophores emit and absorb optical energy with appropriate wavelengths, which are constantly increased by heaters that heat the actively growing hair shaft and hair bulb to a temperature 65 °C to 70 °C. Unfortunately, global standards for IPL devices are not presently in practice, although the hair removal sector is estimated to be worth

around \$10 billion annually and many firms are anticipated to launch fresh light-based hair loss equipment (Town and Ash 2010).

The term LED is composed of the initial letters of the Light Emitting Diode. LEDs were discovered in 1962. They convert the electric current, i.e., electric energy, into incoherent, narrow-spectrum light energy. In other words, they emit light when connected to the electric circuit. LEDs are the most widely used optical semiconductor diodes placed on a reflective surface. LEDs are safe, low cost, long lasting, more accurate and can give clear images and can illuminate larger surfaces, can be produced in various spectra, need low power requirement therefore have low electricity consumption, low power density, high brightness and a new light source having a single specific wavelength (Feehan et al. 2018; Mota et al. 2018; Oh and Jeong 2019; Oshima et al. 2011). LEDs and hence LED devices are available in a wide wavelength range changing from ultraviolet (UV) to visible light zone and infrared (NIR) bandwidth (247 nm to 1300 nm) (Mota et al. 2018; Oshima et al. 2011).

In the 1990s, the National Aeronautics and Space Administration (NASA, USA) developed the first LEDs with a very narrow light spectrum under the space medicine program. Research with the developed LEDs showed that light at a certain wavelength accelerates plant growth. Due to insufficient healing of the submarine Navy Commandos' wounds under high sea pressure and astronauts under zero gravity field conditions, NASA investigated the use of LED therapy in wound healing and received positive results from this research. These results led to the investigation of non-thermal treatments, particularly in dermatology, and approval by the U.S. Food and Drug Administration (FDA) as an insignificant risk procedure for humans. Later studies have shown that LEDs can be used in treatment procedures. As a result of these investigations, LEDs are now used for various health problems, from cosmetic indications to skin cancer treatment (as a photodynamic therapy light source). Today, the use of LEDs has increased significantly due to a better understanding of photobiology in clinical practice and the increasing demand for minimally invasive but effective dermatological treatments (Barolet 2008; Mota et al. 2018; Oh and Jeong 2019; Opel et al. 2015; Oshima et al. 2011; Trelles, Allones, and Mayo 2006).

LED therapies use a single specific wavelength light, which is typically characterized by color. The most common modalities are blue and red LED treatments (Feehan et al. 2018). LED photobiomodulation is a low-cost and newest category of nonthermal light treatments (Barolet 2008; Nascimento et al. 2019).

Although a person's normal body temperature varies according to the health condition, age, gender, environmental temperature, time of day

and similar factors, it is generally around 37 °C (Body temperature norms; Geneva et al. 2019).

It has been reported in the literature that there are important relationships between tissue temperatures and tissue health. For example, temperatures between 35 °C and 40 °C in tissues cause photochemical effects, that is, biostimulation effects, temperatures between 40 °C and 48 °C cause thermal effects, temperatures between 48 °C and 60 °C create photoablation effects, and temperatures beyond 60 °C has been reported to cause permanent damage (Kim and Glen Calderhead 2011; Peng et al. 2008; Pradeep Kumar Gupta, Mahesh Kumar Swami n.d.). It has been also reported that temperature increases up to 10 °C affect blood flow changes and vascular permeability, and trigger enzyme activity. Temperatures below 40 °C, called photoactivation, are explained by cellular activation. At temperatures between 40 °C and 48 °C, some molecular and tissue reactions occur, such as protein structure changes, hydrogen bond breakage and retraction. This photothermal event is classified as reversible variations. After 48 °C, photothermal effects cause serious structural changes in proteins (denaturation) and this change is called irreversible damage (Gupta, P. K., Swami, M. K., & Patel 2013; Kim and Glen Calderhead 2011; Peng et al. 2008).

It is vitally important to ensure the measurement reliability and accuracy of the therapy devices used in the health field. Unfortunately, most of the devices used in the healthcare field do not have an established "measurement traceability chain". There is a big gap in this area. This situation poses a great risk for every segment of the health system. In the health sector, measurement devices are used in a wide range and the variety, and use of these devices are increasing day by day. It is a legal obligation to ensure the measurement accuracy of the devices, performance controls and calibrations. In this context, it is aimed to make thermal measurements of light therapy devices such as Laser, IPL and LED used in the health sector due to the light effects.

This study's ultimate goal is to provide temperature characterization of devices used extensively for medical treatment such as Laser, IPL and LED. Health problems caused by the unsafe use of these devices in the public may also be reported from time to time. Thus, another aim is to investigate the temperature effects of these light therapy devices with scientific methods and find new approaches and new methods.

Phantoms are used extensively in medical scientific research as test objects due to their ability to simulate tissues. In this chapter, the effects of a low-power laser, IPL and LED lights used in light therapies have been characterized in different phantoms. As far as investigated from the literature, no work has been done on these light sources using phantoms



(tissue-mimicking materials). Because of this feature, this study is unique and can pave the way for many other research studies in the future.

## 2. Materials and Methods

### 2.1 Tissue-Mimicking Materials (TMMs) or Phantoms

In this study, three different phantoms will be mentioned. These are “Agar”, “Zerdine” and “Muscle” phantoms.

Agar is an important polysaccharide derived from Agarose (Nayar et al. 2012). It is insoluble in water at room temperature but soluble in boiling water. When cooled to a temperature of about 30 °C - 40 °C, it forms a gel structure. Agar phantoms are widely used for ultrasound imaging (ultrasonography) and hyperthermia applications (Culjat et al. 2010).

The Zerdine phantom is prepared according to the method described by Zerhouni and Rachedine in the patent document (Rachedine 1993). The Zerdine phantom is generally used as a reference test material in the quality control of ultrasonic imaging systems.

Muscle phantom was produced by a method similar to the method described by Gutierrez et al. The muscle phantom was prepared with 125 mL of distilled water, 2.3 g of agar, 10.7 g of aluminum oxide and 10 mL of glycerin (Gutierrez et al. 2016). Again muscle phantom is one of the tissue phantom used in ultrasonic studies.

### 2.2 Laser

Optotronics brand VA-I-400-635 model red-colored solid-state diode laser with 635 nm wavelength was used as an optical source for the low-power laser measurements mentioned in this chapter. A picture of the laser used in the study can be seen in Figure 1.



Figure 1. A picture of the laser used in the study

### 2.3 IPL (Intense Pulsed Light)

IPL experiments were carried out by Philips brand, Lumea Prestige model IPL therapy (hair removal treatment) device. The Philips Lumea Prestige IPL device's operating range, shown in Figure 2, was between 560 nm and 1200 nm. As a piece of important information, it should also be noted that the IPL device is equipped with a color tone detection sensor and does not work if the color tone is not recognized in contact with the skin.



Figure 2. IPL therapy device and its usage.

### 2.4 LED (Light Emitting Diode)

LED measurements were carried out by the Tristar One brand LED therapy device. The LED therapy device had four basic lights. These were red, green, blue and yellow. Red LED was operating at 640 nm wavelength, Blue LED was operating at 423 nm wavelength, Green LED was operating at 532 nm wavelength and Yellow LED was operating at 583 nm wavelength. Besides, different colors could be obtained by opening two colors at the same time. In this study, measurements were also taken under two mixed light colors. It must be turned on the yellow and red LED lights together to obtain orange color, and red and blue LED lights to get the purple color. The Tristar One brand LED therapy device used in the study can be seen in Figure 3.

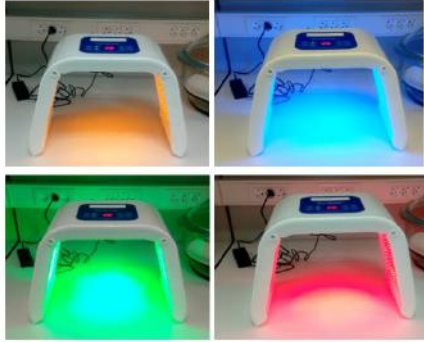


Figure 3. The Tristar One brand LED therapy device.

### 2.5 Temperature Characterization

The thermocouple used in TMM for IPL and LED measurements was T-Type Metronic commercial thermocouple. This thermocouple was made of a silicon-insulated, Cu-CuNi tin coated with Teflon/FEP and the maximum diameter of this thermocouple was 2.7 mm.

A PC-based Data Acquisition and Monitoring Interface were developed for multi-channel temperature measurements in TMM. This is called the DBK83 temperature measurement system. Hardware components of the measurement system include a PCI data acquisition board (IOtech's Daqboard 2000), a signal conditioner module (IOtech's DBK83) for thermocouple signals (Analog In) and a PC. The PC-based temperature measurement system for IPL and LED can be seen in Figure 4 and Figure 5 respectively.



Figure 4. The PC-based temperature measurement system used for the IPL phantom experiment.



Figure 5. The temperature measurement system and its components for the LED experiment.

Two different thermocouples and two different temperature measurement systems were used for low-power laser measurements. The first temperature measurement system used was the DBK83 temperature measurement system and the thermocouple used in this system was a T-type ultra-thin thermocouple. A PC-based Data Acquisition and Monitoring Interface have been developed for multi-channel temperature measurements in the phantom for the DBK83 temperature measurement system. This T-type thermocouple is Physitemp Ultra Fine IT Series Flexible Micro Probe IT-24P. The maximum outer diameter is 0.23 mm and the insulated tip has a cross section of 0.13 mm x 0.07 mm. This ultra-thin thermocouple is very fragile but reacts very quickly (4 ms). A picture of this system can be seen in Figure 6. The second temperature measurement system used was the UME MEDMET temperature measurement system developed by UME Medical Metrology Laboratory and the thermocouple used in this system was the NTC-type thermistor temperature system. UME MEDMET temperature measurement device had five connectable 10 k $\Omega$  NTC type thermistor temperature sensors. The sensitivity of the temperature sensors was 0.5%. A picture of this system can be seen in Figure 7.

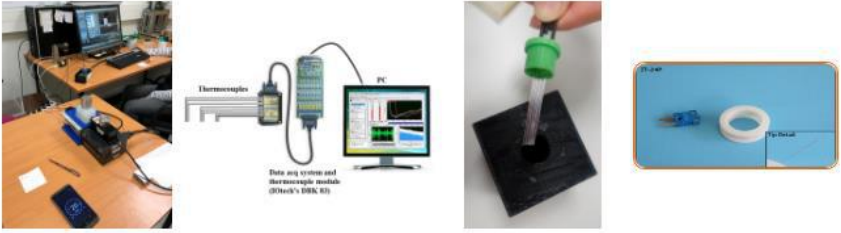


Figure 6. A picture of the DBK83 temperature measurement system and T-Type thermocouple used in this system



Figure 7. A picture of the UME MEDMET temperature measurement system and NTC-Type thermocouple used in this system

### 3. Results and Discussion

The temperature measurements done by using the DBK83 system and Physitemp T-type ultra-thin thermocouples can be seen schematically from Figure 8. The laser beam was set as the target in the "center" thermocouple in all experiments.

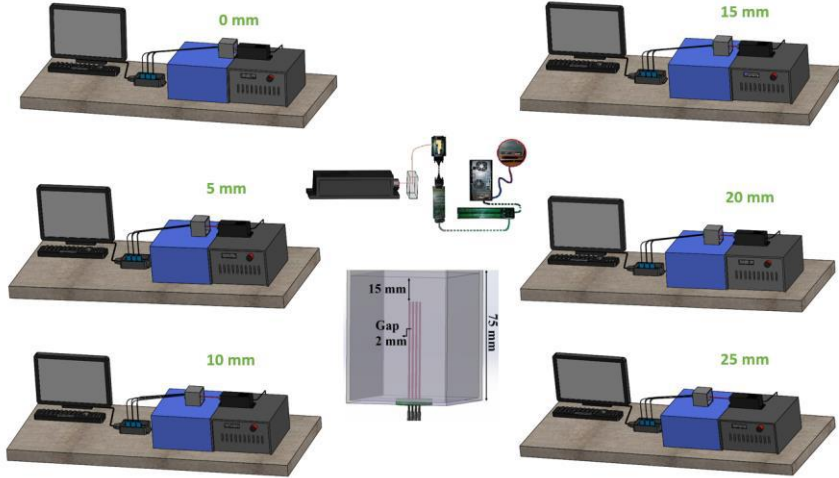


Figure 8. An illustration picture of DBK83 temperature measurement system with Physitemp T-type ultra-thin thermocouples.

Measurements were taken as follows in the experiments. All experiments done for temperature measurements were carried out under controlled laboratory ambient conditions (Temperature range was  $23\text{ }^{\circ}\text{C} \pm 3\text{ }^{\circ}\text{C}$ ). First, when the laser light was off, the internal temperatures were determined by the temperature measurement system using the thermocouples within the Zerdine phantom. The laser light was then operated separately for 20 s, 40 s, 60 s and 80 s at 0 mm (in contact with the Zerdine phantom), 5 mm, 10 mm, 15 mm, 20 mm, 25 mm distances and the temperatures caused by the laser light were determined. The detected maximum temperatures and temperature differences (maximum temperature with laser light - maximum temperature without laser light) can be seen in Table 1 in the following.

Table 1. The detected maximum temperatures and temperature differences caused by the low-power laser beam applied at different times (20 s, 40 s, 60 s and 80 s) and from different distances to Zerdine phantom's surface by using DBK83 temperature measurement system and Physitemp T-type ultra-thin thermocouples.

20 s	5 mm	10 mm	15 mm	20 mm	25 mm
Max. Temperature (°C)	26.95	26.71	25.77	25.01	25.26
Temperature Difference (°C)	2.16	2.06	1.26	0.96	1.03
40 s	5 mm	10 mm	15 mm	20 mm	25 mm
Max. Temperature (°C)	27.3	26.81	25.8	25.04	25.32
Temperature Difference (°C)	2.55	2.23	1.33	1.03	1.07
60 s	5 mm	10 mm	15 mm	20 mm	25 mm
Max. Temperature (°C)	27.47	26.88	25.82	25.1	25.33
Temperature Difference (°C)	2.74	2.36	1.36	1.07	1.15
80 s	5 mm	10 mm	15 mm	20 mm	25 mm
Max. Temperature (°C)	27.63	27.16	25.91	25.37	25.33
Temperature Difference (°C)	2.91	2.63	1.47	1.12	1.14

As for the second laser experiment, the current ambient temperatures within the muscle phantom were first recorded before applying the laser. Later, the laser was applied from suitable predetermined distances to the muscle phantom container for 20 s, 40 s, 60 s and 80 s separately. Thermistor type temperature sensors recorded temperatures for each period (20 s, 40 s, 60 s and 80 s). Later, the differences between the maximum temperatures seen while the laser was working and the maximum ambient temperatures detected while the laser was not working were determined for each different distance. Table 2 shows the average temperatures determined for different distances and the different laser application durations, while Table 3 shows the maximum temperatures differences determined for different distances and the different laser application times.

As you see, the average temperature increases as the laser application time increases.

Table 2. The average temperatures determined for different distances and the different laser application durations

Detected Average Temperatures (°C)				
Distance (cm)	20 s	40 s	60 s	80 s
<b>1</b>	21.81 ± 0.16	22.57 ± 0.34	22.79 ± 0.47	24.12 ± 0.47
<b>1.3</b>	21.00 ± 0.07	21.74 ± 0.12	21.61 ± 0.16	22.18 ± 0.20
<b>1.8</b>	20.97 ± 0.03	21.56 ± 0.05	21.35 ± 0.05	21.81 ± 0.07
<b>2.3</b>	21.17 ± 0.02	21.74 ± 0.03	21.57 ± 0.04	21.96 ± 0.04
<b>2.8</b>	21.63 ± 0.02	22.04 ± 0.03	21.91 ± 0.03	22.22 ± 0.03

Table 3. The maximum temperatures differences determined for different distances and the different laser application times

Maximum Temperature Differences (°C)				
Distance (cm)	20 s	40 s	60 s	80 s
<b>1</b>	0.66	1.05	1.40	2.40
<b>1.3</b>	0.18	0.42	0.55	0.64
<b>1.8</b>	0.08	0.17	0.20	0.20
<b>2.3</b>	0.13	0.15	0.25	0.17
<b>2.8</b>	0.12	0.15	0.24	0.13

The IPL therapy device examined in this study for agar phantom generated an average temperature of  $22.59\text{ }^{\circ}\text{C} \pm 0.61\text{ }^{\circ}\text{C}$  for 15.4 mm in depth and  $21.19\text{ }^{\circ}\text{C} \pm 0.05\text{ }^{\circ}\text{C}$  for 35.3 mm in depth. When the temperature differences before and after applying IPL at different power levels were evaluated together, it was seen that the IPL device created an average temperature of  $1.59\text{ }^{\circ}\text{C} \pm 0.61\text{ }^{\circ}\text{C}$  within the phantom at a depth of 15.4 mm. Likewise, the average temperature created by the IPL device at a depth of 35.3 mm was  $0.19\text{ }^{\circ}\text{C} \pm 0.05\text{ }^{\circ}\text{C}$ . It can be easily said that these temperatures rise differences are not very significant in terms of photothermal effects.



The average internal temperature for all different color LEDs has been found as  $18.24\text{ }^{\circ}\text{C} \pm 0.82\text{ }^{\circ}\text{C}$ . The average internal temperature rise difference within the phantom between light-off and light-on conditions has been found as  $0.31\text{ }^{\circ}\text{C} \pm 0.22\text{ }^{\circ}\text{C}$ . The temperature rise differences found are not very significant in terms of photothermal effects. The temperature rise differences found are again not effective and dangerous for human skin.

As a result, the average temperatures and maximum temperature increase differences determined in all phantom studies made with the light sources used in this study can be seen in Table 4.

Table 4. The detected maximum temperature differences and average temperatures caused by the different light sources

Light Source	Phantom (TMM)	Thermocouple Type	Depth of Thermocouple (mm)	Max Temperature Differences ( $^{\circ}\text{C}$ )	Average Temperature Detected ( $^{\circ}\text{C}$ )
<b>Laser</b>	Zerdine	T-Type Physitemp Ultra Fine	5	2.91	$27.47 \pm 0.16$
<b>Laser</b>	Muscle	NTC type thermistor temperature sensor	10	2.40 (for 80 s)	$24.12 \pm 0.47$ (for 80 s)
<b>IPL</b>	Agar	T-Type Metronic	15.4	1.59	$22.59 \pm 0.61$
<b>LED</b>	Agar	T-Type Metronic	31.2	0.31	$18.24 \pm 0.82$

Since the human body temperature is around  $37\text{ }^{\circ}\text{C}$ , the maximum temperature differences found in the study can increase the body temperature up to a maximum of approximately  $40\text{ }^{\circ}\text{C}$  when all thermocouples are considered. Therefore, these temperatures will produce photochemical effects, i.e., biostimulation. In other words, it can be deduced that the used laser will not have irreversible effects on living tissues.

#### 4. Conclusions

In this study, the effects of a low-power laser, IPL and LED lights used in various therapies using Zerdine, Muscle and Agar phantoms were characterized.

Firstly, laser-sourced temperature measurement studies within the Zerdine phantom were performed using two different thermocouples and two different temperature measurement systems. The temperatures and temperature differences found are mostly of the kind that triggers photochemical processes rather than photothermal effects. At the same time, it has been shown that the laser with 400 mW power is safe to use on humans up to 80 s and a minimum approach distance of 25 mm (15 mm inner + 10 mm outer distance). This study also investigated how much temperature effect a low-level laser source used for therapeutic purposes exerts on a muscle phantom. It was concluded that the temperature increases caused by the low-power laser beam applied on the muscle phantom for 20 s, 40 s, 60 s and 80 s are safe and suitable for thermal therapy.

Secondly, it was investigated whether an IPL device, which is one of the devices that emit instant intense light and used for treatment, is safe in terms of temperature effect by using agar phantom. It was found that the IPL therapy device examined in this study produced an average temperature of  $22.59\text{ }^{\circ}\text{C} \pm 0.61\text{ }^{\circ}\text{C}$  for a depth of 15.4 mm and  $21.19\text{ }^{\circ}\text{C} \pm 0.05\text{ }^{\circ}\text{C}$  for a depth of 35.3 mm for agar phantom. Again, the temperature difference caused by the IPL therapy device was  $1.59\text{ }^{\circ}\text{C} \pm 0.61\text{ }^{\circ}\text{C}$  for 15.4 mm depth and  $0.19\text{ }^{\circ}\text{C} \pm 0.05\text{ }^{\circ}\text{C}$  for 35.3 mm depth. The temperature values found in the light of the literature's data are not very important in terms of photothermal effects. Also, these measured temperature values indicate that the IPL therapy device is indeed a non-thermal therapy device. Furthermore, this study confirms that such devices found in the literature are safe and harmless in terms of adverse temperature effects.

Thirdly, it was also investigated whether an LED device, which is one of the light-emitting devices and can emit light in different colors and used for treatment, is safe in terms of temperature effect with agar, which is also a tissue-like material. It was found that the LED therapy device produced an average of  $19.72\text{ }^{\circ}\text{C} \pm 1.01\text{ }^{\circ}\text{C}$  on the phantom surface and  $18.24\text{ }^{\circ}\text{C} \pm 0.82\text{ }^{\circ}\text{C}$  in the agar phantom. Again, the temperature difference caused by the LED therapy device was  $0.31\text{ }^{\circ}\text{C} \pm 0.22\text{ }^{\circ}\text{C}$  in the phantom and  $0.74\text{ }^{\circ}\text{C} \pm 0.25\text{ }^{\circ}\text{C}$  in the phantom surface. These temperature values found are not very important in terms of photothermal effects in the light of the literature's data. Thus, these measured temperature values indicate that the LED therapy device is indeed a non-thermal therapy device. Although there is no new research on the safety of such devices in the

literature, the results of this study confirm the information available in the literature that such devices are safe and harmless.

As a result, it was shown in this study that these light sources have a character that stimulates photochemical reactions in cells, rather than producing a thermal or ablation effect. In addition to this, the following recommendations can be made regarding these studies;

- In the future, these studies can be carried out using different types of phantoms for lasers with different powers and light emitting therapy devices such as IPL and LED.
- In the future, these studies can be expanded with multiple thermocouples positioned differently within the phantom.
- This method of phantom studies can be used as a tool for safety assessments of light-emitting devices and treatment suitability.
- In the future, these studies could be improved with more accurate temperature sensors.
- Test laboratories or research institutes can work on phantoms as a verification method for such therapy devices.
- This study can also provide a data entry for future coverage assessment of energy-based medical devices.

## References

- Ash, Caerwyn et al. 2017. "Lasers and Intense Pulsed Light (IPL) Association with Cancerous Lesions." *Lasers in Medical Science* 32(8): 1927–33.
- Barolet, Daniel. 2008. "Light-Emitting Diodes (LEDs) in Dermatology." *Seminars in Cutaneous Medicine and Surgery* 27(4): 227–38.
- "Biostimulation Laser." <https://wayback.archive-it.org/7993/20180424190505/https://www.fda.gov/Radiation-EmittingProducts/ResourcesforYouRadiationEmittingProducts/ucm252757.htm> (September 11, 2019).
- "Body Temperature Norms." <https://medlineplus.gov/ency/article/001982.htm> (September 11, 2019).
- Ciocon, David H., Andreas Boker, and David J. Goldberg. 2009. "Intense Pulsed Light: What Works, What's New, What's Next." *Facial Plastic Surgery* 25(5): 290–300.
- Cook, Jason R., Richard R. Bouchard, and Stanislav Y. Emelianov. 2011. "Tissue-Mimicking Phantoms for Photoacoustic and Ultrasonic Imaging." *Biomedical Optics Express* 2(11): 3193.
- Culjat, Martin O., David Goldenberg, Priyamvada Tewari, and Rahul S. Singh. 2010. "A Review of Tissue Substitutes for Ultrasound Imaging." *Ultrasound in Medicine and Biology* 36(6): 861–73.
- Daoud, Alexander A. et al. 2019. "Efficacy of Combined Intense Pulsed Light (IPL) With Fractional CO<sub>2</sub>-Laser Ablation in the Treatment of Large Hypertrophic Scars: A Prospective, Randomized Control Trial." *Lasers in Surgery and Medicine* 51(8): 678–85.
- Diker, Nurettin et al. 2019. "Evaluation of the Effects of Low-Level Laser Therapy on Diabetic Bone Healing." *Journal of Craniofacial Surgery* 30(7): 1994–98.
- Durmus, Huseyin Okan et al. 2020. "Investigation of Basic Optical Properties of Tissue Phantoms under 635 Nm Low-Level Laser Irradiation." *IEEE Medical Measurements and Applications, MeMeA 2020 - Conference Proceedings*: 2–7.
- Elmer, Corey J. 2019. "Is Low-Level Laser Therapy ( LLLT ) Effective in Reducing Pain and Ulcer Size in Diabetic Patients with Foot Ulcers ?"
- Feehan, Jack et al. 2018. "Therapeutic Applications of Polarized Light: Tissue Healing and Immunomodulatory Effects." *Maturitas* 116(June): 11–17.

- Geneva, Ivayla I., Brian Cuzzo, Tasaduq Fazili, and Waleed Javaid. 2019. "Normal Body Temperature: A Systematic Review." *Open Forum Infectious Diseases* 6(4): 1–7.
- Gold, Michael H. 2007. "Photodynamic Therapy with Lasers and Intense Pulsed Light." *Facial Plastic Surgery Clinics of North America* 15(2): 145–60.
- Goldberg, David J. 2012. "Current Trends in Intense Pulsed Light." *Journal of Clinical and Aesthetic Dermatology* 5(6): 45–53.
- González-Rodríguez, A. J., and R. Lorente-Gual. 2015. "Current Indications and New Applications of Intense Pulsed Light." *Actas Dermo-Sifiliograficas* 106(5): 350–64. <http://dx.doi.org/10.1016/j.adengl.2015.04.001>.
- Gupta, P. K., Swami, M. K., & Patel, H. 2013. *Light–Tissue Interactions. In Handbook of Photomedicine*. Boca Raton, FL: CRC Press.
- Gutierrez, M. I., S. A. Lopez-Haro, A. Vera, and L. Leija. 2016. "Experimental Verification of Modeled Thermal Distribution Produced by a Piston Source in Physiotherapy Ultrasound." *BioMed Research International* 2016.
- Jeon, Min Sik et al. 2019. "Effect of Intense Pulsed Light on the Deactivation of Lipase: Enzyme-Deactivation Kinetics and Tertiary Structural Changes by Fragmentation." *Enzyme and Microbial Technology* 124(July 2017): 63–69. <https://doi.org/10.1016/j.enzmictec.2019.02.001>.
- Kim, Won Serk, and R. Glen Calderhead. 2011. "Is Light-Emitting Diode Phototherapy (LED-LLLT) Really Effective?" *Laser Therapy* 20(3): 205–15.
- Lee, Seung Youl et al. 2017. "Development of Evaluation Methods for the Approval and Review of Intense Pulsed Light (IPL)." *Proceedings of the Annual International Conference of the IEEE Engineering in Medicine and Biology Society, EMBS*: 4525–28.
- Li, Bohan, Xiao Wang, and Lin Cao. 2019. "Low-Level Laser Therapy (LLLT) Promotes Facial Nerve Regeneration after Crush-Injury in Rats." *International Journal of Clinical and Experimental Medicine* 12(6): 7257–63.
- Ma, Yuke, and Xiangang Xu. 2019. "Multi Wavelength Low Level Lasers Transmeatal Irradiation (MWLLLTI) for Motion Sickness." *OALib* 06(02): 1–5.
- Madani, Azamsadat, Farzaneh Ahrari, Amir Fallahrastegar, and Naemeh Daghestani. 2020. "A Randomized Clinical Trial Comparing the

- Efficacy of Low-Level Laser Therapy (LLLT) and Laser Acupuncture Therapy (LAT) in Patients with Temporomandibular Disorders.” *Lasers in Medical Science* 35(1): 181–92.
- Mazur, Carolina Eurich. 2019. “Crohn ’ s Disease : Low-Level Laser Therapy ( LLLT ) as an Adjuvant Treatment of Oral Lesions Abstract :” : 1–5.
- Moghadam, Manijeh Yousefi. 2019. “Low Level Laser Therapy: A Promising Adjunct Therapeutic Modality for Pain Control after Coronary Artery Bypass Graft Surgery.” *Korean Journal of Pain* 32(1): 51–52.
- Mota, Lidiane Rocha et al. 2018. “Efficacy of Phototherapy to Treat Facial Ageing When Using a Red versus an Amber LED: A Protocol for a Randomised Controlled Trial.” *BMJ Open* 8(5).
- Musstaf, Ruwaidah A., David F.L. Jenkins, and Awadhesh N. Jha. 2019. “Assessing the Impact of Low Level Laser Therapy (LLLT) on Biological Systems: A Review.” *International Journal of Radiation Biology* 95(2): 120–43. <https://doi.org/10.1080/09553002.2019.1524944>.
- Nascimento, LÍzia Daniela E.Silva, KÁrita Francisca E.Silva Nascimento, Diego Rodrigues Pessoa, and Renata Amadei Nicolau. 2019. “Effects of Therapy with Light Emitting Diode (LED) in the Calcaneal Tendon Lesions of Rats: A Literature Review.” *Scientific World Journal* 2019.
- Nayar, V. T., J. D. Weiland, C. S. Nelson, and A. M. Hodge. 2012. “Elastic and Viscoelastic Characterization of Agar.” *Journal of the Mechanical Behavior of Biomedical Materials* 7: 60–68. <http://dx.doi.org/10.1016/j.jmbbm.2011.05.027>.
- Netz, Uwe J., Jan Toelsner, and Uwe Bindig. 2011. “Calibration Standards and Phantoms for Fluorescence Optical Measurements.” *Medical Laser Application* 26(3): 101–8. <http://dx.doi.org/10.1016/j.mla.2011.05.002>.
- Oh, Phil Sun, and Hwan Jeong Jeong. 2019. “Therapeutic Application of Light Emitting Diode: Photo-Oncomic Approach.” *Journal of Photochemistry and Photobiology B: Biology* 192(November 2018): 1–7. <https://doi.org/10.1016/j.jphotobiol.2019.01.003>.
- Olejniak, Maria, Zuzanna Ślebioda, and Barbara Dorocka-Bobkowska. 2019. “Low-Level Laser Therapy (LLLT) in the Treatment of Recurrent Aphthous Stomatitis (RAS) – A Promising Treatment Option: A Report of Two Cases.” *Dental and Medical Problems* 56(3): 317–21.


- Opel, Daniel R. et al. 2015. "Light-Emitting Diodes: A Brief Review and Clinical Experience." *Journal of Clinical and Aesthetic Dermatology* 8(6): 36–44.
- Oshima, Yasushi et al. 2011. "Effect of Light-Emitting Diode (LED) Therapy on the Development of Osteoarthritis (OA) in a Rabbit Model." *Biomedicine and Pharmacotherapy* 65(3): 224–29. <http://dx.doi.org/10.1016/j.biopha.2011.02.011>.
- Peng, Qian et al. 2008. "Lasers in Medicine." *Reports on Progress in Physics* 71(5).
- Poojar, Basavaraj et al. 2017. "Methodology Used in the Study." *Asian Journal of Pharmaceutical and Clinical Research* 7(10): 1–5.
- Pradeep Kumar Gupta, Mahesh Kumar Swami, Harishankar Patel. *Light–Tissue Interactions from: Handbook Of Photomedicine*. CRC Press.
- Rachedine, M. B. Zerhouni and M. 1993. "Ultrasonic Calibration Material and Method."
- Rigonato-Oliveira, Nicole Cristine et al. 2019. "Effect of Low-Level Laser Therapy (LLLT) in Pulmonary Inflammation in Asthma Induced by House Dust Mite (HDM): Dosimetry Study." *International Journal of Inflammation* 2019.
- Sinesi et al. 2019. "A Refractory Labial Fissured Cheilitis Treated with Low Level Laser Therapy (L.L.L.T)." *Proceedings* 35(1): 73.
- Soltes, Barbara. 2010. "Intense Pulsed Light Therapy." *Obstetrics and Gynecology Clinics of North America* 37(4): 489–99. <http://dx.doi.org/10.1016/j.ogc.2010.09.005>.
- Stangl, Sabine, Ina Hadshiew, and Wolfgang Kimmig. 2008. "Side Effects and Complications Using Intense Pulsed Light (IPL) Sources." *Medical Laser Application* 23(1): 15–20.
- Town, Godfrey, and Caerwyn Ash. 2010. "Are Home-Use Intense Pulsed Light (IPL) Devices Safe?" *Lasers in Medical Science* 25(6): 773–80.
- Trelles, Mario A., Inés Allones, and Esther Mayo. 2006. "Combined Visible Light and Infrared Light-Emitting Diode (LED) Therapy Enhances Wound Healing after Laser Ablative Resurfacing of Photodamaged Facial Skin." *Medical Laser Application* 21(3): 165–75.

## CHAPTER VI


### SAFETY ASSESSMENT OF A 635 NM LOW-POWER SOLID-STATE MEDICAL LASER ON ZERDINE PHANTOM

Hüseyin Okan Durmuş<sup>1,\*</sup> & Emel Çetin Arı<sup>2</sup> & Baki Karaböce<sup>3</sup>  
MirHasan Yu. Seyidov<sup>4</sup>


<sup>1</sup>*Gebze Technical University, Physics Department,  
Gebze-Kocaeli, Turkey, e-mail: hokandurmus@gtu.edu.tr,*

 ORCID 0000-0003-0973-0643


<sup>2</sup>*(Dr.), TUBITAK National Metrology Institute (TUBITAK UME),  
Medical Metrology Laboratory, Kocaeli, Turkey, e-mail: emel.cetin@tubitak.gov.tr,*

 ORCID 0000-0003-1144-1584

<sup>3</sup>*(Assoc. Prof. Dr.), TUBITAK National Metrology Institute (TUBITAK UME),  
Medical Metrology Laboratory, Kocaeli, Turkey, e-mail: baki.karaboce@tubitak.gov.tr,*

 ORCID 0000-0002-5814-3157

<sup>4</sup>*(Prof. Dr.), Gebze Technical University, Physics Department,  
Gebze-Kocaeli, Turkey, e-mail: smirhasan@gtu.edu.tr*

 ORCID 0000-0003-4901-7674

**\*Corresponding author:** hokandurmus@gtu.edu.tr, huseyinokan.durmus@tubitak.gov.tr

#### 1. Introduction

Although lasers are now commonly used in all aspects of our lives, medical lasers may be seen to be the most effective, intensive and widely applied devices. Today medical lasers are used in several processes such as removal of port wine stains (van Raath et al. 2019), dark spots (Grevelink, J. M., González, S., Bonoan, R., Vibhagool, C., & Gonzalez 1997), tattoos (Hardy et al. 2020), acne scars (Schoenberg et al. 2019), blemishes (Zaidi, Hussain, and Sudhakaran 2019), hair removal (Bray, F. N., Falto-Aizpurua, L., Griffith, R. D., Simmons, B., Rajabi-Estarabadi, A., & Nouri 2019), treatment of wrinkles (Koren et al. 2020), skin resurfacing (Cuzalina, L. A., & Rhyne 2019), skin rejuvenation (Kaya and Guvenc 2019), tooth whitening (Ahmed M Elmarakby et al. 2019), removing dental decay (Chan and Fried 2019), removing tissue in eye surgery (include removing tumors, cataracts, or proliferating blood vessels common to diabetic retinopathy) (Firoz MV, Vishal Gupta N, and Sandeep K 2019), correcting astigmatism, nearsightedness, and farsightedness (T. im Kim et al. 2019), reshaping the cornea and focusing images correctly



on the retina (Grewal, A. M., Grewal, S. S., Thakur, A., Gupta, A., & Malhotra 2019), lithotripsy (Becker, Gross, and Netsch 2019), laser angioplasty (Stanek 2019), laser cancer diagnosis (Ghasemi, Parvin, and Lotfi 2019), laser cancer treatment (Kefayat et al. 2020; van Luijtelaar et al. 2019), laser imaging/laser doppler holography (Puyo, L., Paques, M., Fink, M., Sahel, J. A., & Atlan), laser scanning microscopy (Chaigneau, Roche, and Charpak 2019), and usage in a general/plastic surgery operations (Khalkhal et al. 2019).

Lasers are categorized according to their energy density as high and low-power lasers. High-power lasers are referred to as thermal lasers; and low-power lasers are referred to as therapy lasers. This definition can also be split into "Ablative Laser Systems" and "Nonablative Laser Systems" based on their intensity (Boyras and Yıldız 2016).

Tissue-mimicking materials or phantoms are widely used in medical research fields due to their ability to simulate biological soft tissues. In addition, phantoms are also used in preclinical testing for medical applications as reference test objects. The ability to repeatedly use phantoms to mimic the properties of living tissues, particularly in medical science, offers great advantages. The use of tissue-mimicking materials in biophotonics is also very common (Cetin, E., Karaboce, B., Durmus; Çetin et al. 2019; Cook, Bouchard, and Emelianov 2011; C. Kim et al. 2008; Konugolu Venkata Sekar et al. 2019; Shah et al. 2008; Srinivasan, Kumar, and Singh 2001).

Low-level laser therapy (LLLT), photobiomodulation (PBM therapy) or cold laser is a light therapy using lasers or LEDs to enhance tissue healing, decrease the pain and inflammation wherever the beam is applied. And it is usually applied by a doctor, therapist or technician.

For several years, PBM has been used on sports injuries, arthritic joints, syndromes of neuropathic pain, back and neck pain. Scientific evidence confirms that lower intensity lasers (Class 3B lasers) is more effective for inflammation and healing. However, high intensity lasers is ideal for analgesia.

This reference (What is Cold Laser Therapy?) gives the general acceptance chronological date of Photobiomodulation Therapy as follows.

- 2019 - Multinational Association for Supportive Care in Cancer (MASCC) guidelines recommend PBM treatment for the prevention of oral mucositis.

- 2018 - National Institute of Health and Care Excellence (NICE) guidance for the UK NHS recommends laser therapy for oral mucositis.
- 2017 - UK NIHR funded RCT on the Clinical and Cost Effectiveness of Low Level Laser in the Management of Oral Mucositis in Head and Neck Cancer Irradiation, 10 NHS hospitals, 380 patients in progress.
- 2017 – Low-Level Laser improves survival of head and neck cancer patients.
- 2017 - American College of Physicians Guidelines include a "strong recommendation" for Low-Level Laser Therapy as a non-invasive Treatments for Acute, Subacute & Chronic Low Back Pain.
- 2016 - BMJ PBM for chronic non-specific low back pain: a systematic review and meta-analysis of randomised controlled trials found "moderate quality of evidence" and "clinically important benefits" in the short term.
- 2014 - 30% reduction of the costs of hospitalisation in PBM Oral Mucositis patients.
- 2014 - MASCC guideline revisions recommend use of PBM to reduce the incidence and severity of Oral Mucositis.
- 2013 - Journal Applied Oral Science. TMJ Systematic review "it seems clear that the use of laser brings benefits when properly applied and administered".
- 2012 - Multinational Association for Supportive Cancer Care (MASSC) systematic review recommends PBM for oral mucositis.
- 2011 - European Society for Medical Oncology (ESMO) systematic review suggest PBM for reducing duration and severity of oral mucositis.
- 2011 - British Medical Journal (BMJ) Clinical Guidelines for tennis elbow "Likely to be beneficial for short-term pain relief & improvement of function".
- 2010 - The International Association for the Study of Pain (Global Task Force on musculoskeletal pain) recommend laser for myofascial pain syndrome.
- 2010 - British Journal of Sports Medicine, systematic review of surgical and conservative interventions for frozen shoulder found "strong evidence" for PBM.
- 2010 - American Physical Therapy Association guidelines recommend PBM for Achilles tendonitis.
- 2009 - The Lancet "PBM reduces pain immediately after treatment in acute neck pain and for up to 22 weeks in patients with chronic neck pain".

- 2008 - World Health Organisation (Bone and Joint Task Force) recommended PBM for neck pain.

Furthermore, significant associations between tissue temperature and tissue health have been documented in the literature. For instance, temperatures in a tissue range from 35 °C and 40 °C cause photochemical effects, i.e. biostimulation effects; thermal impacts between 40 °C and 48 °C; photoablation effects between 48 °C and 60 °C; and temperatures above 60 °C has been reported to cause permanent damages (W. S. Kim and Glen Calderhead 2011; Peng et al. 2008; Pradeep Kumar Gupta, Mahesh Kumar Swami). It has also been documented that temperature increases up to 10 °C influence blood flow changes and vascular permeability, and activity of enzymes. Cellular activation is clarified by temperatures below 40 °C, called photoactivation.

Some molecular and tissue reactions such as changes in protein structure, hydrogen bond breakage and retraction occur at temperatures between 40 °C and 48 °C. This photothermal phenomenon known as reversible changes. After 48 °C, photothermal effects cause serious structural changes in proteins (denaturation) and this change is called irreversible damage (Gupta, P. K., Swami, M. K., & Patel 2013; W. S. Kim and Glen Calderhead 2011; Peng et al. 2008; Pradeep Kumar Gupta, Mahesh Kumar Swami).

Laser energy used in the health should be applied to a degree that would not harm the patient. Therefore, laser instruments, and hence beams, must undergo significant safety checks before being used on the patient. This energy needs to be administered from a distance not harming the patient in laser systems used for treatment. The distance at which it is safe to be exposed to a laser beam is unique for each laser type. In this context, the term “Maximum Permissible Exposure (MPE)” is used in the literature. MPE is the highest amount of laser radiation that a human can be exposed to without adverse consequences or biological modifications to the skin or eye. The MPE is determined by the laser’s wavelength, the associated energy and the time of exposure. The evaluation of lasers in terms of human health is defined in IEC 60825-1 and ANSI Z136.1 standards. The Zerdine phantom was used as the laser device’s test object in this study. The temperatures caused by the laser application at different distances from the outside phantom surface was determined by thermocouples located at 15 mm from the inner surface of Zerdine phantom for 20 s, 40 s, 60 s and 80 s. In this chapter, the results of the temperature measurement studies, which is created by the 635 nm red colored solid-state diode laser in the Zerdine phantom, will be shared and these determined temperatures

will be evaluated in terms of MPE for the eye and skin contact on the basis of the ANSI Z136.1 standard.

## 2. Materials and Methods

### 2.1 Tissue-Mimicking Materials

Zerdine phantom was used as a test object in the study. The Zerdine phantom is generally used in the quality control of ultrasonic imaging systems as a reference test material. The Zerdine® phantom was produced in a rectangular container using the formulation stated in the patents of Zerhouni and Rachedine (M. B. Zerhouni and M. Rachedine 1993). A picture of the Zerdine phantom specimen and test set-up can be seen in Figure 1.



Figure 1. A picture of the Zerdine phantom under test

### 2.2 Laser

Optotronics brand VA-I-400-635 model red colored solid-state diode laser with 635 nm wavelength was used as a measurement optical source. A picture of the laser used in the study can be seen in Figure 2.



Figure 2. A picture of the laser used in the study

### 2.3 Temperature Characterization

The DBK83 temperature measurement system and Physitemp T-type ultra-thin thermocouple were used in this study. A PC based, multi-channel Data Collection and Monitoring Interface has been developed for temperature measurements. Hardware components of this measurement system include a PCI data acquisition card (IOtech's Daqboard 2000), a signal conditioning module for thermocouple signals (IOtech's DBK83), and a PC. For temperature measurements, Physitemp brand ultra fine IT series flexible micro thermocouple IT-24P was used. These thermocouples have a maximum outer diameter of 0.23 mm, and also a thin, insulated tip with a cross-section of 0.13 mm x 0.07 mm. The ultra-thin thermocouple is fragile, but responds very quickly (4 ms) due to its ultra-thin nature. A picture of this system can be seen in Figure 3.

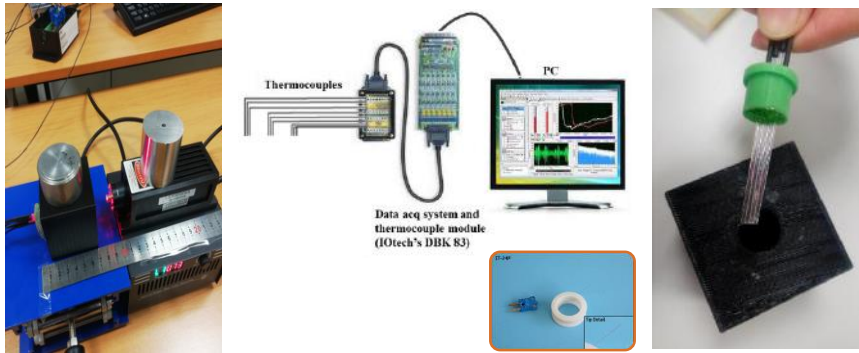


Figure 3. A picture of the DBK83 temperature measurement system and T-Type thermocouple used in this system

For internal temperature measurements, Physitemp T-type ultra-thin thermocouples were placed at 15 mm inside the phantom surface. The distance of the thermocouples is 2 mm away from each other. Placement of thermocouples within the phantom used in temperature measurement can be seen from Figure 4.

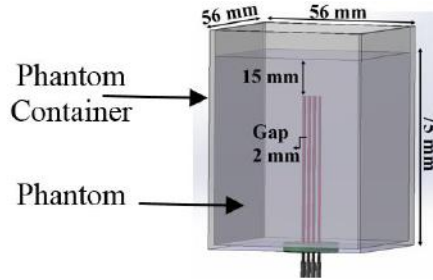


Figure 4. A picture of placement of thermocouples within the phantom

#### 2.4 Thermal Camera and Surface Temperature Measurements

Optris PI infrared thermal camera as shown in Figure 5 and its PC software were used for surface temperature measurements. The declared uncertainty budget for the infrared camera was  $\pm 2\text{ }^{\circ}\text{C}$  as stated in the product catalog.

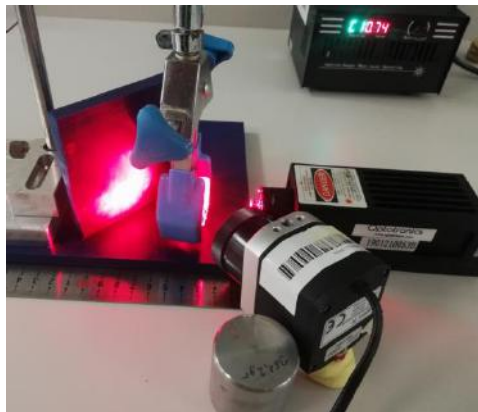


Figure 5. A picture surface temperature measurement set-up for Zerdine phantom with infrared thermal camera

#### 2.5 The Optical Power Meter and Laser Power Density Measurement

Ophir brand StarBright model optical power meter and Ophir brand 3A type thermal sensor were used for optical power measurements. The optical power meter and measurement picture can be seen in Figure 6 (a) and (b). Before starting the experiments, laser power density characterization has been performed as per different distances for maximum power set-up (400 mW) as seen in Figure 6 (c).

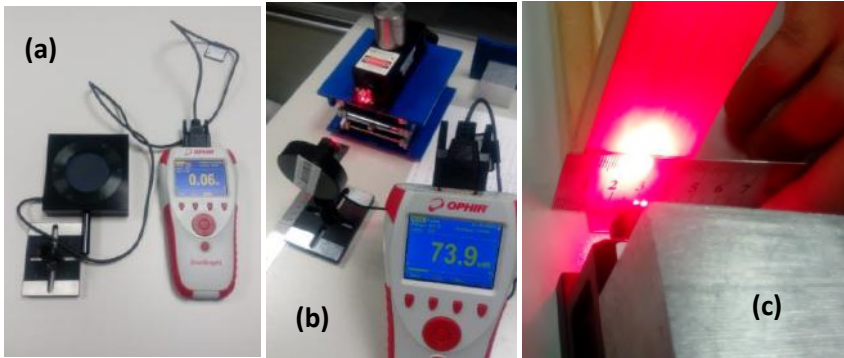


Figure 6. The used optical power meter and laser power density characterization.

### 2.6 Laser Safety Evaluation

For laser safety evaluation, the term “Maximum Permissible Exposure (MPE)” is used in the literature. MPE is the maximum amount of laser radiation a person can be exposed to without dangerous effects or biological changes in the eye or skin. MPE is determined by the wavelength of the laser, the associated energy and the exposure time. The evaluation of lasers in terms of human health is defined in IEC 60825-1 and ANSI Z136.1 standards. The safety evaluation of the laser used in this study was made according to the ANSI Z136.1 Standard. Table 5a of the ANSI Z136.1 standard allows the calculation of the safe limit values for the ocular exposure at different times, while Table 6 and Table 7 of the this standard allow the calculation of the limit values for different durations for the skin. For example, for ocular exposure, MPE is  $1.8 \times t^{0.75} \times 10^{-3} \text{ J/cm}^2$  from  $18 \times 10^{-6} \text{ s}$  to  $10 \text{ s}$  in the visible region between  $0.400 \mu\text{m}$  and  $0.700 \mu\text{m}$  wavelength and MPE is  $1 \times 10^{-3} \text{ W/cm}^2$  from  $10 \text{ s}$  to  $3 \times 10^4 \text{ s}$  in the visible region between  $0.500 \mu\text{m}$  and  $0.700 \mu\text{m}$  wavelength. Again, for skin exposure, MPE is  $1.1 \times CA \times t^{0.25}$  from  $10^{-7} \text{ s}$  to  $10 \text{ s}$  in the visible region between  $0.400 \mu\text{m}$  and  $1.400 \mu\text{m}$  wavelength and MPE is  $0.2 \times CA \text{ W/cm}^2$  from  $10 \text{ s}$  to  $3 \times 10^4 \text{ s}$  in the visible region between  $0.400 \mu\text{m}$  and  $1.400 \mu\text{m}$  wavelength. CA is 1.0 for wavelength region between  $0.400 \mu\text{m}$  and  $0.700 \mu\text{m}$ .

### 3. Results and Discussion

The temperature measurements performed by using the DBK83 system and Physitemp T-type ultra-thin thermocouples can be seen schematically from Figure 7. The laser beam was set to the target in the "center" thermocouple in all experiments.

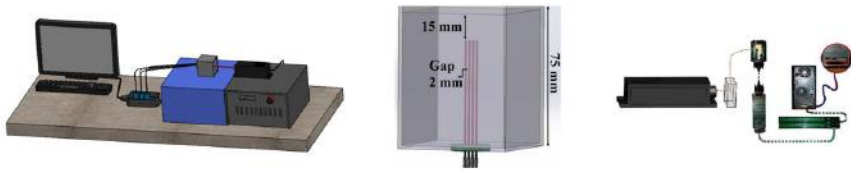


Figure 7. A picture of the DBK83 temperature measurement system with Physitemp T-type ultra-thin thermocouples.

The temperature measurements from the zero distance, that is, when the laser beam is in contact with the phantom surface, to the varying distances (5 mm, 10 mm, 15 mm, 20 mm and 25 mm) were taken for 20 s, 40 s, 60 s and 80 s durations. Application of 635 nm red-color diode laser from "0" mm distance to the phantom surface for 20 s duration, and minimum, maximum and the detected temperature difference at different thermocouple locations can be seen from Figure 8 and Figure 9 respectively.

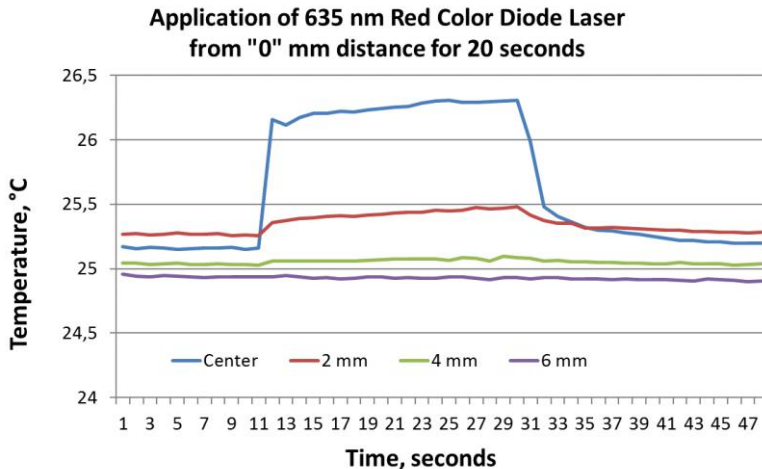


Figure 8. Application of 635 nm red color diode laser from "0" mm distance to the phantom surface for 20 s duration



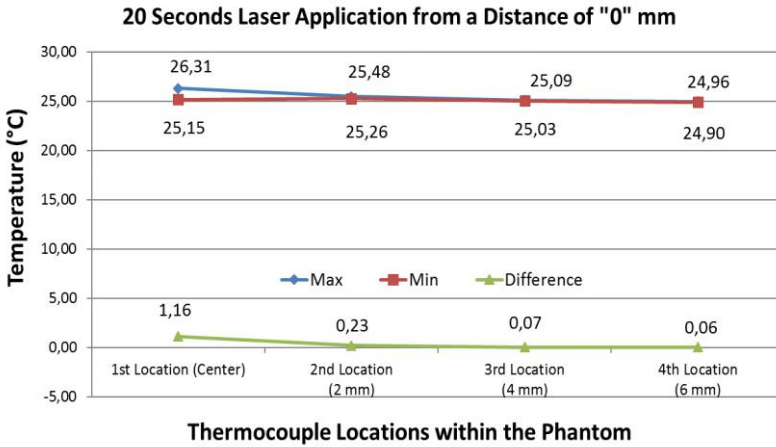


Figure 9. Minimum, maximum and temperature differences detected at different thermocouple locations for 20 s duration.

By plotting the temperature differences measured from thermocouples according to their locations, the following graphs for 20 s are obtained in between Figure 10 and Figure 13.

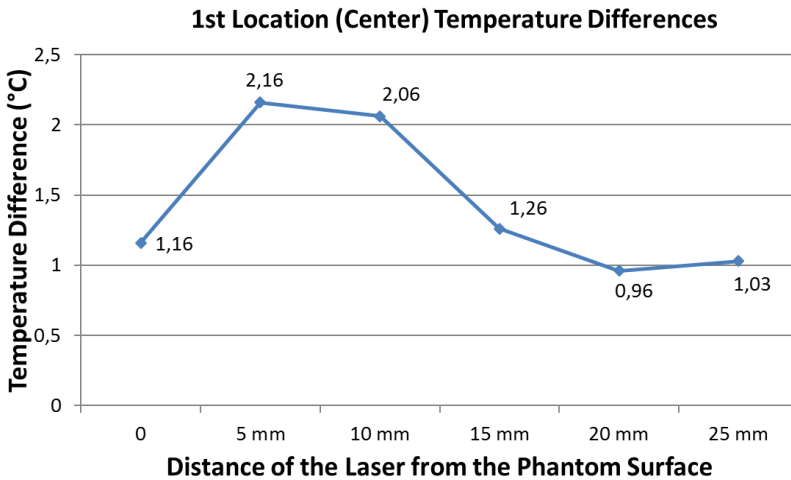


Figure 10. Temperature difference values of 20 s laser beam applied from "0" mm to 25 mm distance measured by 1st located (center) thermocouples

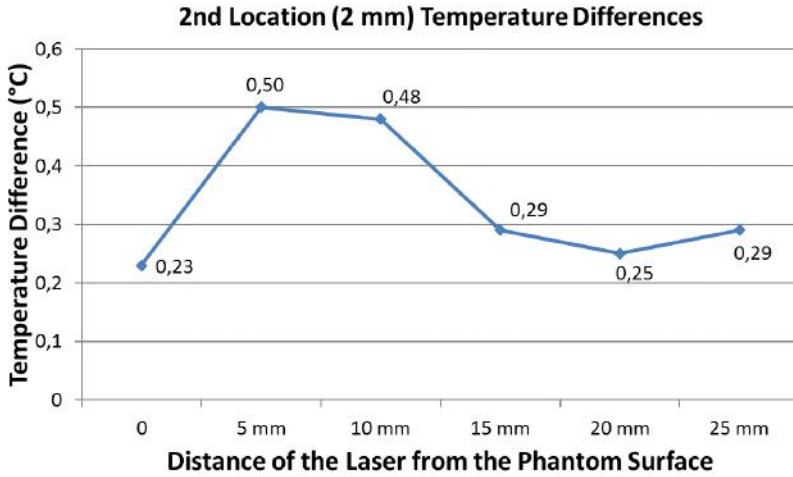


Figure 11. Temperature difference values of 20 s laser beam applied from “0” mm to 25 mm distance measured by 2nd located thermocouples

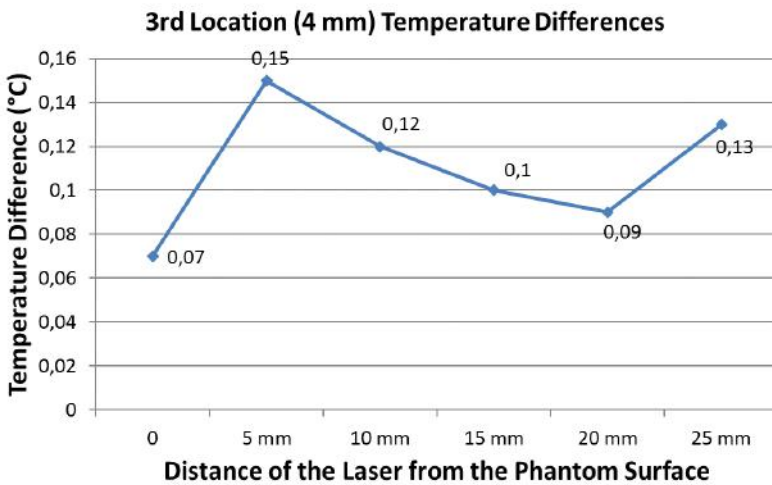


Figure 12. Temperature difference values of 20 s laser beam applied from “0” mm to 25 mm distance measured by 3rd located thermocouples

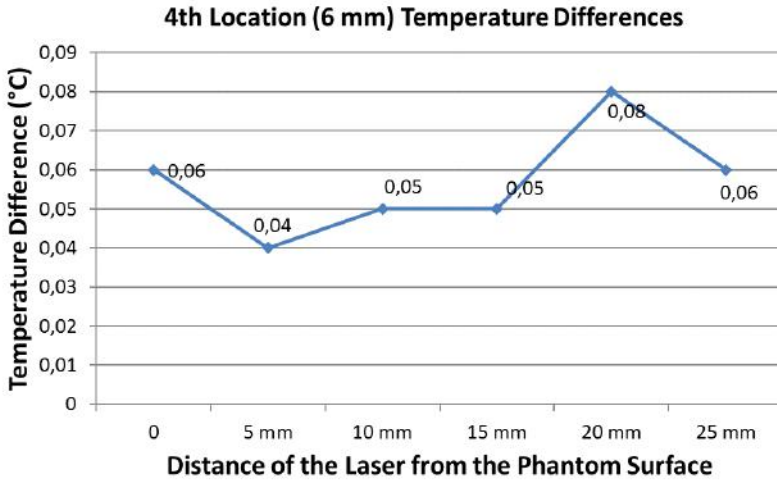


Figure 13. Temperature difference values of 20 s laser beam applied from “0” mm to 25 mm distance measured by 4th located thermocouples

When the laser was taken closer to zero distance to the phantom surface (i.e. at the “0” mm point), the temperature value was observed to be lower. This situation was also found to be the same for all periods of time (20 s, 40 s, 60 s and 80 s). This may be attributed to the vast amount of scattering, absorption or reflection on the phantom surface or within of the phantom, which may result in lowering the temperature value. So when this last one doesn’t include, namely the zero point, the temperature differences graphs show much more meaningful results. In other words, the temperature differences reduces as the laser beam moves away from the phantom surface. Therefore, it will be more meaningful to evaluate results starting from 5 mm for all graphs of 20 s, 40 s, 60 s and 80 s. It can be seen the graphs of the temperature differences caused by 20 s laser beam applied from a distance of 5 mm to 25 mm for 20 s from the figures in between Figure 14 and Figure 17.

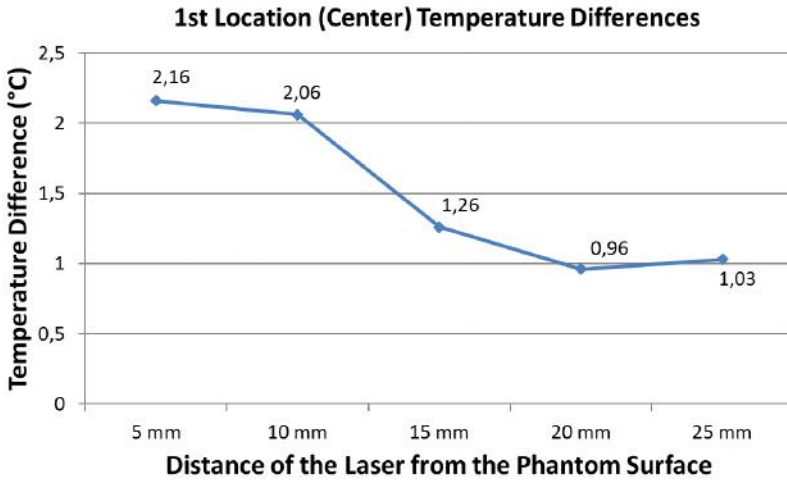


Figure 14. Temperature difference values of 20 s laser beam applied from 5 mm to 25 mm distance measured by 1st located (center) thermocouples

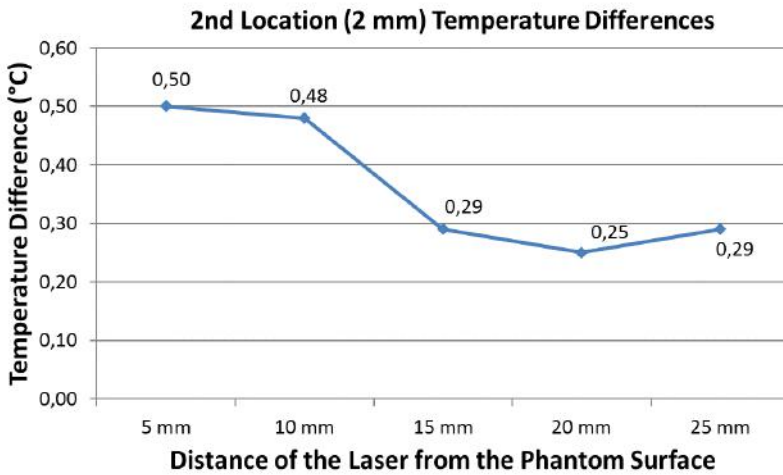


Figure 15. Temperature difference values of 20 s laser beam applied from 5 mm to 25 mm distance measured by 2nd located thermocouples

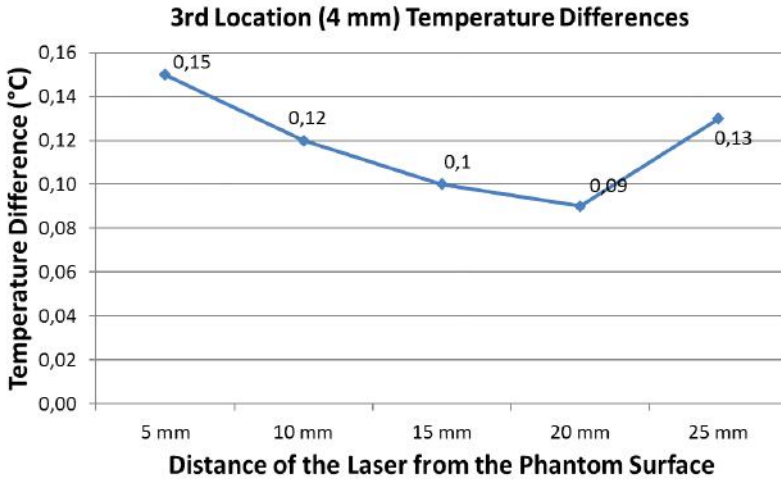


Figure 16. Temperature difference values of 20 s laser beam applied from 5 mm to 25 mm distance measured by 3rd located thermocouples

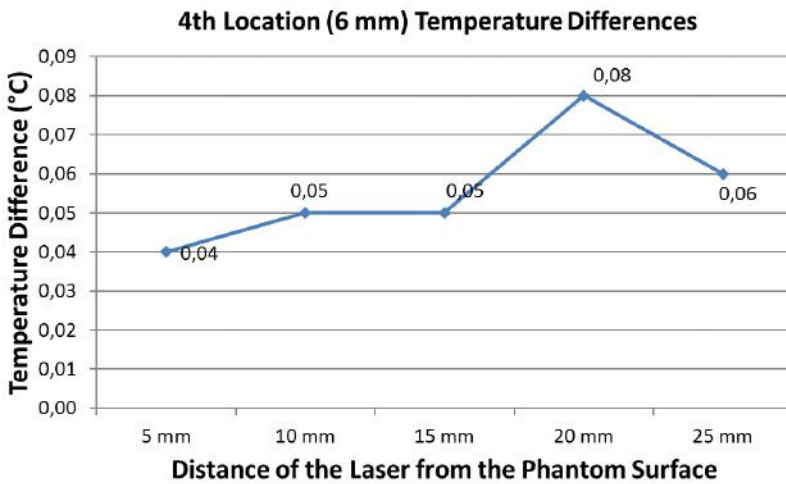


Figure 17. Temperature difference values of 20 s laser beam applied from 5 mm to 25 mm distance measured by 4th located thermocouples

When the same evaluation is performed separately for the Zerdine Phantom for 40, 60 and 80 s, just as it was made for 20 s, the following Table I appears.

Table 1. The detected maximum temperatures and temperature differences caused by the laser beam applied at different times (20 s, 40 s, 60 s and 80 s) and from different distances to Zerdine phantom surface by using the DBK83 temperature measurement system and Physitemp T-type ultra-thin thermocouples.

<b>20 s</b>	<b>5 mm</b>	<b>10 mm</b>	<b>15 mm</b>	<b>20 mm</b>	<b>25 mm</b>
<b>Max. Temperature (°C)</b>	<b>26.95</b>	26.71	25.77	25.01	25.26
<b>Temperature Difference (°C)</b>	<b>2.16</b>	2.06	1.26	0.96	1.03
<b>40 s</b>	<b>5 mm</b>	<b>10 mm</b>	<b>15 mm</b>	<b>20 mm</b>	<b>25 mm</b>
<b>Max. Temperature (°C)</b>	<b>27.3</b>	26.81	25.8	25.04	25.32
<b>Temperature Difference (°C)</b>	<b>2.55</b>	2.23	1.33	1.03	1.07
<b>60 s</b>	<b>5 mm</b>	<b>10 mm</b>	<b>15 mm</b>	<b>20 mm</b>	<b>25 mm</b>
<b>Max. Temperature (°C)</b>	<b>27.47</b>	26.88	25.82	25.1	25.33
<b>Temperature Difference (°C)</b>	<b>2.74</b>	2.36	1.36	1.07	1.15
<b>80 s</b>	<b>5 mm</b>	<b>10 mm</b>	<b>15 mm</b>	<b>20 mm</b>	<b>25 mm</b>
<b>Max. Temperature (°C)</b>	<b>27.63</b>	27.16	25.91	25.37	25.33
<b>Temperature Difference (°C)</b>	<b>2.91</b>	2.63	1.47	1.12	1.14

The highest temperature difference for the Zerdine phantom was observed as 2.91 °C for 80 s using the T-Type thermocouple and 635 nm red-colored diode laser with a maximum power of 400 mW.

The highest temperature and temperature difference was discovered at the nearest distance to the phantom surface, which can be seen from the Table I. Since the human body temperature is 37 °C, the found maximum temperature increase can increase the body temperature maximum to  $40 \pm 1$  °C at most for 80 s if we consider maximum 1 °C uncertainty value. So, this observation lets us understand the photobiostimulation effect more clearly. That's why, these temperatures will create photochemical effects

to a great extent, i.e. biostimulation. In other words, the used laser will not create permanent damage to the living tissue.

After measuring internal temperatures with the Zerdine phantom, The surface temperatures were also detected. In measuring surface temperatures, each distance measurement was realized as follows. The laser was triggered firstly, after an elliptical location marker had been used to determine the spot point of the white laser beam on the screen. The laser was then cooled and reference temperatures were recorded with the laser turned off. Then the laser was turned on and the temperatures at the end of one minute were recorded. This process was repeated at least three times and it was waited for one minute before each repetition. Significant temperature increases in surface temperatures were not observed for the Zerdine phantom. Because the Zerdine phantom has crystal clear color, it was concluded that the laser beam passes through on it and to verify this, another phantom surface was painted in different colors and the measurements were repeated and temperature increases were observed this time. For this reason, surface temperature measurements were carried out on a special blue colored absorber material, which is used as an absorber in ultrasonic studies, to determine the surface temperatures caused by the laser. The measurement of surface temperatures with the absorber was made by increasing the distance between the absorber surface and the laser by half cm from 0.5 cm (5 mm) to 5 cm (50 mm).

The graph of the surface temperature differences detected at each distance during 80 s is given in Figure 18.

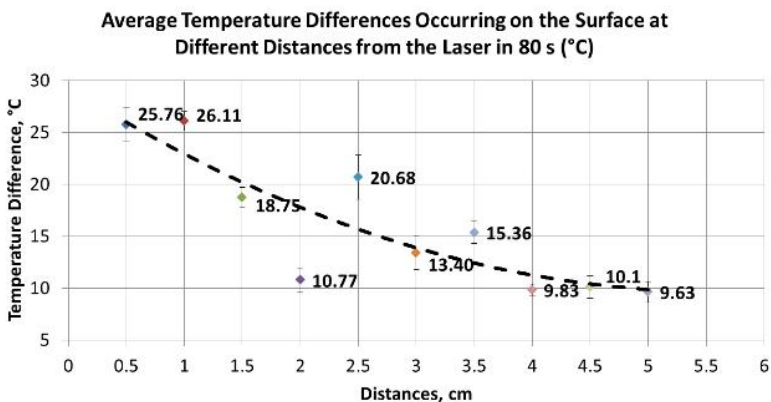


Figure 18. The surface temperature differences detected at each distance during 80 s

Before starting the experiments, laser power density characterization had also been performed as per different distances for maximum power set-up (400 mW). One can see the characterization calculation of the used laser in Table II.

Table 2. The irradiance ( $\text{mW}/\text{cm}^2$ ) measurement, and calculation of the used laser as per optical power measurement

Mesafe (cm)	W/cm <sup>2</sup>	mW/cm <sup>2</sup>
0,5	1,774	1774
1	1,061	1061
1,5	0,4087	408,7
2	0,2907	290,7
2,5	0,1509	150,9
3	0,1164	116,4
3,5	0,0784	78,4
4	0,0555	55,5
4,5	0,0413	41,3
5	0,0241	24,1
5,5	0,024	24
6	0,0155	15,5
6,5	0,0161	16,1
7	0,0102	10,2
7,5	0,0106	10,6
8	0,0073	7,3
8,5	0,0075	7,5
9	0,0051	5,1
9,5	0,0055	5,5
10	0,0036	3,6
10,5	0,0037	3,7
11	0,0028	2,8
11,5	0,0028	2,8
12	0,002	2
12,5	0,0021	2,1
13	0,0016	1,6
13,5	0,0016	1,6
14	0,0012	1,2
14,5	0,0013	1,3
15	0,001	1

The calculated MPE values for the laser used up to 10 s are as follows in Table III.

Table 3. Calculated MPE values for the laser used up to 10 s.

Calculated Energy Density for 10 s	For Ocular Exposure	For Skin Exposure
	1 $\text{mW}/\text{cm}^2$	200 $\text{mW}/\text{cm}^2$



As a result, the 635 nm red-colored diode laser with 400 mW max power should be viewed from a distance of at least 15 cm and should be in contact with the skin from a maximum distance of 2.5 cm as per ANSI Z136.1 Standard. In terms of temperature evaluation, average temperatures (approximately 10 °C) found at a distance of 5 cm are also within the range of thermal reversible variations (37+10=47 °C).

#### **4. Conclusions**

In this study, laser-caused internal and surface temperature measurements of the tissue-mimicking material called as Zerdine phantom were conducted. Based on the findings, it was examined whether the laser had a photoablation effect or not, and the laser's safety assessment was carried out.

The found temperature differences (max. 3 °C) in internal temperature measurements are of the kind that trigger photochemical processes rather than photothermal effects. Temperature differences (in average 10 °C up to 5 cm distance) found in surface temperature measurement are also of the thermal kind processes rather than photoablation effects.

The safety evaluation of the laser used was carried out in compliance with the ANSI Z136.1 standard. According to the MPEs allowed by the standard, a laser with a power of 400 mW should be visually viewed for 10 s from a distance of at least 15 cm and contacted with the skin for 10 s from a distance of at least 25 mm. In other words, it has been demonstrated in this study that a laser with a maximum optical power of 400 mW can be used safely in humans up to 80 s and a minimum approach distance of 25 mm.

In the future, these experiments can again be performed utilizing various forms of phantoms on the basis of the dose concept and temperature measurement in terms of ocular and skin evaluation for different low-power lasers.

## References

- Ahmed M Elmarakby et al. 2019. "Review Article Teeth Bleaching: A Closer View." *Ec Dental Science* 7(June 2019): 1677–83.
- Becker, Benedikt, Andreas J. Gross, and Christopher Netsch. 2019. "Ho:YAG Laser Lithotripsy: Recent Innovations." *Current Opinion in Urology* 29(2): 103–7.
- Boyras, İsmail, and Ahmet Yıldız. 2016. "Lazer Çeşitleri ve Yüksek Yoğunluklu Lazer Kullanımı." *Journal of Contemporary Medicine* 6(0): 104–9.
- Bray, F. N., Falto-Aizpurua, L., Griffith, R. D., Simmons, B., Rajabi-Estarabadi, A., & Nouri, K. 2019. "Lasers for Hair Removal." *Pediatric Dermatologic Surgery*: 273–87.
- Cetin, E., Karaboce, B., Durmus, H.O. "Doku – Benzeri Malzemelerin Akustik Parametrelerinin Belirlenmesi." In *13. Ulusal Akustik Kongresi ve Sergisi, TAKDER*, 8.
- Çetin, Emel, Hüseyin Okan Durmuş, Baki Karaböce, and Nuran Kavaklı. 2019. "Acoustical Characterization of Tissue - Mimicking Materials." *Medical Measurements and Applications, MeMeA 2019 - Symposium Proceedings*: 1–5.
- Chaigneau, Emmanuelle, Morgane Roche, and Serge Charpak. 2019. "Unbiased Analysis Method for Measurement of Red Blood Cell Size and Velocity with Laser Scanning Microscopy." *Frontiers in Neuroscience* 13(JUN): 1–9.
- Chan, Kenneth H., and Daniel Fried. 2019. "Selective Ablation of Dental Caries Using Coaxial Co 2 (9.3-Mm) and near-IR (1880-Nm) Lasers." *Lasers in Surgery and Medicine* 51(2): 176–84.
- Cook, Jason R., Richard R. Bouchard, and Stanislav Y. Emelianov. 2011. "Tissue-Mimicking Phantoms for Photoacoustic and Ultrasonic Imaging." *Biomedical Optics Express* 2(11): 3193.
- Cuzalina, L. A., & Rhyne, C. H. 2019. *Office-Based Maxillofacial Surgical Procedures. Laser Skin Resurfacing*. Springer, Cham.
- FIROZ MV, VISHAL GUPTA N, and SANDEEP KANNA. 2019. "THE CURRENT TRENDS AND TREATMENTS IN DIABETIC RETINOPATHY." *Asian Journal of Pharmaceutical and Clinical Research* 12(7): 27–33.
- Ghasemi, Fatemeh, Parviz Parvin, and Maryam Lotfi. 2019. "Laser-Induced Fluorescence Spectroscopy for Diagnosis of Cancerous Tissue Based on the Fluorescence Properties of Formaldehyde." *Laser Physics Letters* 16(3).

- Grevelink, J. M., González, S., Bonoan, R., Vibhagool, C., & Gonzalez, E. 1997. "Treatment of Nevus Spilus with the Q-Switched Ruby Laser." *Dermatologic surgery* 23(5): 365–69.
- Grewal, A. M., Grewal, S. S., Thakur, A., Gupta, A., & Malhotra, C. 2019. *Ophthalmic Instruments and Surgical Tools. Refractive Surgery: Basics of Laser Consoles and Ablation Profiles*. Springer, Singapore.
- Gupta, P. K., Swami, M. K., & Patel, H. 2013. *Light-Tissue Interactions. In Handbook of Photomedicine*. Boca Raton, FL: CRC Press.
- Hardy, Curtis L., Ramya Kollipara, Erika Hoss, and Mitchel P. Goldman. 2020. "Comparative Evaluation of 15 Laser and Perfluorodecalin Combinations for Tattoo Removal." *Lasers in Surgery and Medicine* 52(7): 583–85.
- Kaya, Tamer Irfan, and Ulas Guvenc. 2019. "Long Pulse 1,064-Nm Neodymium-Doped Yttrium Aluminum Garnet Laser in Aesthetic Dermatology." *Dermatologic Therapy* 32(3): 1–3.
- Kefayat, Amirhosein et al. 2020. "Utilizing 808 Nm Laser for Sensitizing of Melanoma Tumors to Megavoltage Radiation Therapy." *Lasers in Medical Science* 35(1): 87–93.
- Khalkhal, Ensieh, Majid Rezaei-Tavirani, Mohammad Reza Zali, and Zahra Akbari. 2019. "The Evaluation of Laser Application in Surgery: A Review Article." *Journal of Lasers in Medical Sciences* 10(4): S104–11. <https://doi.org/10.15171/jlms.2019.S18>.
- Kim, Chulhong, Alejandro Garcia-Uribe, Sri-Rajasekhar Kothapalli, and Lihong V. Wang. 2008. "Optical Phantoms for Ultrasound-Modulated Optical Tomography." *Design and Performance Validation of Phantoms Used in Conjunction with Optical Measurements of Tissue* 6870(February 2008): 68700M.
- Kim, Tae im et al. 2019. "Refractive Surgery." *The Lancet* 393(10185): 2085–98. [http://dx.doi.org/10.1016/S0140-6736\(18\)33209-4](http://dx.doi.org/10.1016/S0140-6736(18)33209-4).
- Kim, Won Serk, and R. Glen Calderhead. 2011. "Is Light-Emitting Diode Phototherapy (LED-LLLT) Really Effective?" *Laser Therapy* 20(3): 205–15.
- Konugolu Venkata Sekar, Sanathana et al. 2019. "A Solid Phantom Recipe for Biophotonics Applications: A Step towards Anatomically Correct 3D Tissue Phantoms." *Optics InfoBase Conference Papers Part F142-(4)*: 2090–2100.
- Koren, Amir et al. 2020. "Evaluation of Subject Response Following Treatment for Pigmentation or Wrinkles Using a Diode Laser." *Journal of Cosmetic Dermatology* 19(6): 1371–76.


- van Luijckelaar, A. et al. 2019. "Focal Laser Ablation as Clinical Treatment of Prostate Cancer: Report from a Delphi Consensus Project." *World Journal of Urology* 37(10): 2147–53. <https://doi.org/10.1007/s00345-019-02636-7>.
- M. B. Zerhouni and M. Rachedine. 1993. "“Ultrasonic Calibration Material and Method.”"
- Peng, Qian et al. 2008. "Lasers in Medicine." *Reports on Progress in Physics* 71(5).
- Pradeep Kumar Gupta, Mahesh Kumar Swami, Harishankar Patel. *Light-Tissue Interactions from: Handbook Of Photomedicine*. CRC Press.
- Puyo, L., Paques, M., Fink, M., Sahel, J. A., & Atlan, M. "Non-Invasive and High Temporal Resolution Choroidal and Retinal Blood Flow Imaging Using Laser Doppler Holography." In *In Ophthalmic Technologies XXIX (Vol. 10858, p. 1085811)*, International Society for Optics and Photonics, Vol. 10858, 1085811.
- van Raath, M. I. et al. 2019. "Port Wine Stain Treatment Outcomes Have Not Improved over the Past Three Decades." *Journal of the European Academy of Dermatology and Venereology* 33(7): 1369–77.
- Schoenberg, Elizabeth, Jordan V. Wang, Christopher B. Zachary, and Nazanin Saedi. 2019. "Treatment of Acne Scars with PRP and Laser Therapy: An up-to-Date Appraisal." *Archives of Dermatological Research* 311(8): 643–46. <https://doi.org/10.1007/s00403-019-01936-7>.
- Shah, Jignesh et al. 2008. "Photoacoustic Imaging and Temperature Measurement for Photothermal Cancer Therapy." *Journal of Biomedical Optics* 13(3): 034024.
- Srinivasan, R., D. Kumar, and Megha Singh. 2001. "Optical Tissue-Equivalent Phantoms for Medical Imaging." *Trends in Biomaterials and Artificial Organs* 15(2): 42–47.
- Stanek, Frantisek. 2019. "Laser Angioplasty of Peripheral Arteries: Basic Principles, Current Clinical Studies, and Future Directions." *Diagnostic and Interventional Radiology* 25(5): 392–97.
- "What Is Cold Laser Therapy?" [https://www.thorlaser.com/enquiry.php?utm\\_source=google&utm\\_medium=cpc&keyword=&utm\\_campaign=264612910&gclid=EAIaIQobChMI-4\\_noPzt7AIVNci7CB1g7AXyEAEYASAAEgISofD\\_BwE](https://www.thorlaser.com/enquiry.php?utm_source=google&utm_medium=cpc&keyword=&utm_campaign=264612910&gclid=EAIaIQobChMI-4_noPzt7AIVNci7CB1g7AXyEAEYASAAEgISofD_BwE) (December 18, 2020).
- Zaidi, Zohra, Khalid Hussain, and Simi Sudhakaran. 2019. Treatment of Skin Diseases *Treatment of Skin Diseases. Cosmetic Dermatology*. Springer, Cham.




### MITIGATION OF AMMONIA FROM LITTER BY ADDITIVES IN POULTRY HOUSES

**Busra Yayli<sup>1</sup> & Ilker Kilic<sup>2</sup>**

<sup>2</sup>(RA.), Bursa Uludag University, Bursa, Turkey, e-mail: busrayayli@uludag.edu.tr

 ORCID 0000-0002-0198-3550

<sup>2</sup>(Assoc. Prof. Dr.), Bursa Uludag University, Bursa, Turkey  
e-mail: ikilic@uludag.edu.tr

 ORCID 0000-0003-0087-6718

#### **1. Introduction**

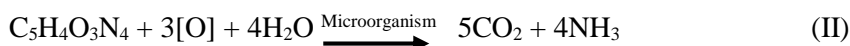
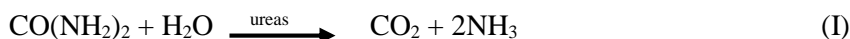
In animal feeding operations (AFO) occur various wastes and pollutants during production. Waste and pollution factors consist of continuous live activities, feeding, excretion, and animal respiration: manure and metabolic digestion of animal's major problem in concentrated animal feeding systems (CAFO). Feces and urine by combining with the litter are decay, feeding and animal activities cause the formation of pollutant gas and pathogens. Carbon dioxide (CO<sub>2</sub>), methane (CH<sub>4</sub>), ammonia (NH<sub>3</sub>), nitrous oxide (N<sub>2</sub>O), hydrogen sulfide (H<sub>2</sub>S), volatile particles, and microorganisms are the most common pollutants from animal operations. NH<sub>3</sub> gas is highly reactive, and its residence time in the atmosphere is shorter than other pollutants.

The agricultural sector is the primary source of ammonia emissions from anthropogenic activities. The agricultural sector constitutes approximately 94% of global anthropogenic NH<sub>3</sub> emissions, about 64% originates from the livestock sector (Steinfeld et al., 2006; Sanchis et al., 2019).

#### **2. Ammonia Formation in Poultry Houses**

NH<sub>3</sub> emissions in poultry houses are generally higher than in other livestock farms. Ammonia consists of microbial decomposition of organic nitrogen (N) compound in manure from animal barns. Nutrients that are not absorbed by animals are excreted as N from the manure with feces and urine (as urea in mammals, as uric acid in poultry) (Oenema et al., 2001; Kilic and Simsek, 2009). Nitrogen taken with feed and nitrogen excreted as feces and uric acid are the primary sources of NH<sub>3</sub> in poultry houses. While the formation of ammonia in the feces occurs slowly, it is rapidly transformed into NH<sub>3</sub> in urine (urea and uric acid) by hydrolysis,

mineralization, and evaporation (Anonymous, 2005). Urea ( $\text{CO}(\text{NH}_2)_2$ ) is hydrolyzed by urease enzymes in anaerobic conditions, causing the formation of ammonia (Equation I-II). Undigested protein and uric acid ( $\text{C}_5\text{H}_4\text{O}_3\text{N}_4$ ) are crash by microorganisms and bacteria, and ammonia is formed in poultry manure (Atapattu et al., 2008) (Equation II-III). The primary source of  $\text{NH}_3$  formation is a degradation of uric acid is in poultry houses. Also, chickens' respiration and aerobic and anaerobic decomposition of litter material increase  $\text{CO}_2$  levels in the house (Ni et al., 2012).



$\text{NH}_3$  is present in aqueous solutions, in the form of ammonium ions ( $\text{NH}_4^+$ ) and non-ionized (liquid)  $\text{NH}_3$  (Equation IV). This situation can be different depending on the pH of the solution. The amount of these two forms of ammonia in an aqueous solution such as manure is called total ammonia nitrogen (TAN). In this transformation, pH and temperature have significant effects (Kilic, 2011). Whereas  $\text{NH}_3$  can be in the atmosphere for a few hours up to 1-5 days,  $\text{NH}_4$  can remain in the atmosphere as an aerosol for 1-15 days (Aneja et al., 2001).

$\text{NH}_3$  remains in the atmosphere for a few hours after spreading, and when combined with gases such as  $\text{NO}_x$  and  $\text{S}_2\text{O}$ , it can remain in the atmosphere for several days. Ammonia reacts with nitrous oxide and sulfur oxides to form ammonium sulfate ( $(\text{NH}_4)_2 \text{SO}_4$ ) and ammonium nitrate ( $\text{NH}_4\text{NO}_3$ ) (Equation V-VI) (Anderson et al., 2003). It can also be transported to long distances by combining with other air pollutants and forming secondary particulate matter (PM<sub>2.5</sub>) (Anonymous, 2020). In addition to producing PM<sub>2.5</sub>, atmospheric  $\text{NH}_3$  can change the clouds' oxidation rates and increase acid rain production. It also contributes to the accumulation of N in the ecosystem. (Naseem & King, 2018).



Various parameters such as litter moisture content, temperature, and litter pH contribute to the formation of  $\text{NH}_3$  in poultry farms (Cabrera and Chiang, 1994; Tiquia and Tam, 2000; Liu et al., 2007; Atapattu et al., 2008; Miles et al., 2011a; Lin, 2014). At higher moisture levels of the litter, faster  $\text{NH}_3$  emission occurs. Business owners should ensure that the litter is dry. For this, it should provide regular ventilation and have sufficient absorbent material in the base. High temperatures increase both bacterial activity and  $\text{NH}_3$  production in the litter. When the litter's pH level reaches higher values, the  $\text{NH}_3$  levels become more variable as the environment turns into a virtual environment and generally increases. The non-ionized  $\text{NH}_3$  form in the fertilizer turns into a gas, and the amount of  $\text{NH}_3$  increases.

Ammonia formation varies according to litter material, aeration rate, manure management practices, animal age, feed ingredient, and seasonal conditions. The type of litter used in the poultry house depends on the type of poultry, the type of litter used, the environmental conditions, the feed composition, the transport of manure, situation (Rodic et al., 2011). Litter change improves poultry health and production, as it provides lower  $\text{NH}_3$  concentrations and lower bacterial density (Terzich et al., 1998). Besides, poultry litter is an essential source of fertilizer, as it contains many nutrients necessary for the growth of plants. Since ammonia consists of manure and litter in the poultry houses, it affects the animals by contacting them before mixing with the indoor air and decreasing the concentration (Atilgan et al., 2010). During the winter months, when ventilation is at minimum capacity, a significant amount of ammonia gas accumulates in the house. Ventilation speed is directly proportional to the emission and inversely proportional to the concentration in the house. In situations where ventilation is insufficient or not possible, the ammonia concentration increases. Having higher moisture content increases  $\text{NH}_3$  production. The  $\text{NH}_3$  emission varies according to the seasons and climates and reaches the highest levels in warmer seasons. The emission rates should be evaluated very well, as the ammonia emission values vary widely according to the countries, cultivation type, and seasons.

In commercial livestock farming,  $\text{NH}_3$  emission occurs due to mixing feces and urine with litter material.  $\text{NH}_3$  formation rates are closely related to microbial bacteria's activities and the density of bacterial populations and microbial activities can be predicted (Okano et al., 2004). The primary sources of  $\text{NH}_3$  include biological processes in animal protein consumption and subsequent degradation of animal waste (Rockfellow et al., 2012). The amount of nitrogen in animal feed ingredients is generally much higher than the animals should take. N, which they cannot take into their bodies, is generally thrown out in the form of  $\text{NH}_3$ . It has been reported that 10-30% of the N amount used for the growth, development, reproduction, and maintenance of animals is used, and the rest is discarded



(Stowel, 2018). Since chickens are in the growing stage in their young period, they spend their grown, and N excretion is decreased. However, in animals that have completed their growth, the feed conversion rate is lower, and the N excretion rate is higher than the growing period. Less ammonia becomes volatile than young chickens, and as the chicken ages, they produce more  $\text{NH}_3$  (Wu-Haan et al., 2007).

### **3. Effects of Ammonia on Environment and Health**

Animal feces contain a significant amount of undigested protein (organic nitrogen) and is mostly converted into ammonia by heterotrophic bacteria under aerobic and anaerobic conditions. While plants can use some of the ammonia produced by bacteria, the excess is converted into ammonium ( $\text{NH}_4$ ) due to hydrolysis. Ammonium is transformed into nitrite ( $\text{NO}_2^-$ ) by Nitrosomonas bacteria under aerobic conditions. With Nitrobacter, a group of nitrification bacteria found in the soil, nitrite is oxidized to nitrate ( $\text{NO}_3^-$ ). Nitrate is used as a fertilizer for plants. Since nitrate is in the form of N, which can be taken, both the plants' intake is more comfortable, increasing groundwater loss in the form of washing. Nitrification takes place by reducing ammonia to ammonium, nitrite, and finally nitrate by nitrification bacteria. Denitrification takes place in aerobic conditions with the transformation of nitrate and nitrite into elemental nitrogen by microorganisms. First, nitrate is reduced to nitrite, and then nitrate is reduced to ammonia for protein formation. With the fixation of free nitrogen in the atmosphere, lightning, rain, and nitrogen-binding bacteria and nitrogen salts are bound to the soil. In the denitrification process,  $\text{N}_2\text{O}$  is formed in the reduction of nitrate. This gas leaves the soil and water and spreads into the atmosphere.  $\text{N}_2\text{O}$  in the atmosphere is reduced to  $\text{N}_2$  and stimulated by oxygen by photolysis, and oxygen oxidizes  $\text{N}_2\text{O}$  to NO (Sawyer et al., 2003) (Figure 1).

Ammonium ( $\text{NH}_4^+$ ), nitrite ( $\text{NO}_2^-$ ), and nitrate ( $\text{NO}_3^-$ ) are water-soluble compounds and are of environmental importance for water resources. Other inorganic oxidation stages,  $\text{N}_2$ ,  $\text{N}_2\text{O}$  (nitrous oxide), NO (nitrous oxide), and  $\text{NO}_2$  (nitrogen dioxide), are in the gas form, and their solubility in water is limited. Excess nitrate in the soil that plants cannot hold is transported to underground waters by leaking from the soil. Nitrate lowers the pH of groundwater, and its N content causes eutrophication and acidification.

$\text{NH}_3$  causes various problems in the ecosystem, not only in the atmosphere but also on land and water.  $\text{NH}_3$  emissions directly or indirectly damage the ecosystem. Soil acidification on land poses a danger by causing eutrophication by decreasing plant species and habitat diversity, algal growth in water. Feed with high nutrient content used in poultry production causes nitrogen and phosphorus-sourced water and soil pollution from production (Sutton et al., 2008; Boggia et al., 2010; Tallentire et al., 2017;

Isik and Kirkpinar, 2020). The N amount in fertilizers applied to the soil is beneficial for soil fertility and products. However, nitrogenous fertilizers applied above the optimum value cause acidification of the soil. Besides, the use of excessive N fertilizers leaks from the soil and mixes with underground waters. It causes algae formation in the water and causes carbon dioxide to increase by consuming the water's oxygen amount. Accordingly, fish deaths occur.

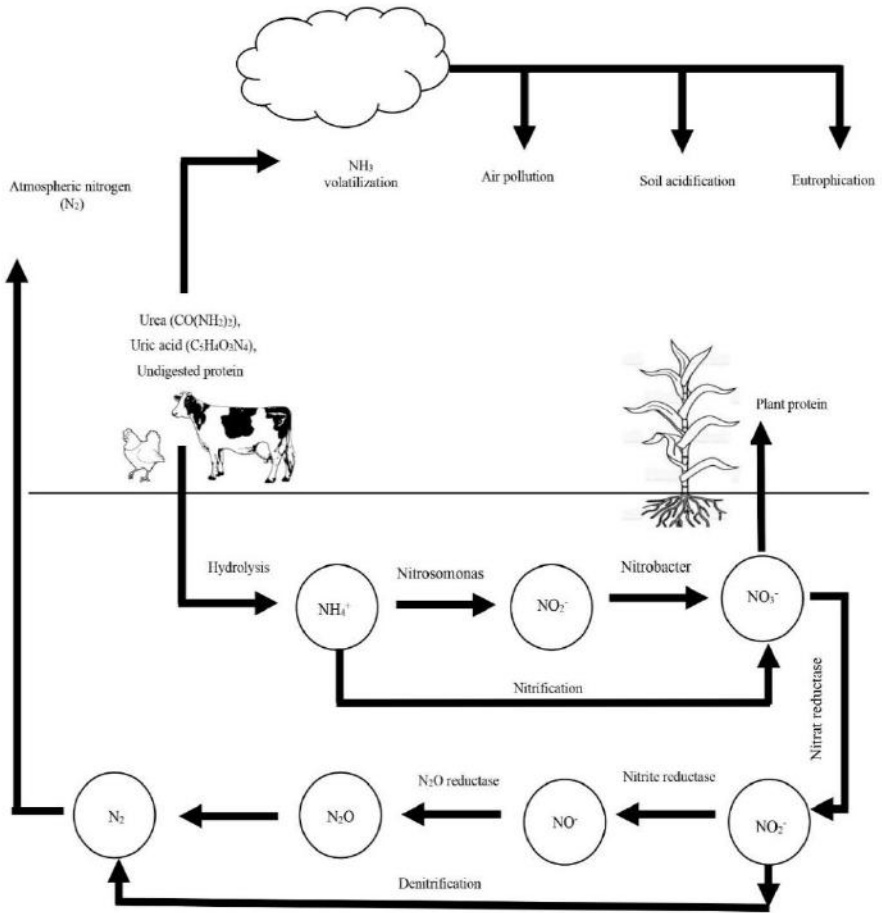


**Figure 1.** N cycle

In laying hens, the high amount of total ammonia nitrogen generated due to anaerobic digestion of chicken manure has been identified as one of the main problems (Farrow et al., 2016; Molaey et al., 2018; Andrade et al., 2020). Since litter is grown in chicken meat breeding operations, the more  $NH_3$  gas is generated due to litter and manure breakdown by microorganisms. Ammonia is the most common and irritating odor gas in the house.  $NH_3$  emission causes potential impacts on the environment and potential impacts on livestock production performance, animal welfare,

and worker health. It is an irritant gas that causes significant health effects in living creatures due to prolonged exposure. The foul odor caused by  $\text{NH}_3$  and  $\text{H}_2\text{S}$  gases in poultry farms causes respiratory distress, causing a decrease in egg production, a decrease in feed utilization rate, and a decrease in the development rate of animals (Eleroglu and Yalcin, 2004). In humans, it can be absorbed quickly through the upper respiratory tract and penetrate the body. Prolonged inhalation irritates the upper respiratory tract, eyes, nose, and throat. Also, the fertilizer's value decreases by reducing the N content in the waste to be used as soil fertilizer because of the adverse effects of ammonia release on poultry production.

#### 4. Abatement of Ammonia from Litter by Additives

In order to reduce the amount of ammonia in the house, it is essential that the bedding is clean and dry, as well as adequate ventilation. Pathogens and microorganisms increase from wetting with fertilizer and urine and increasing moisture content depending on the litter material used. As a result of the microbiological breakdown of manure,  $\text{NH}_3$  volatility increases and causes various problems. Some chemicals can be added to the litter to eliminate gas formation, reduce the formation of other gases, and reduce bacterial growth's harmful effects. Reducing  $\text{NH}_3$  emissions from equine material can also reduce the ventilation capacity, thus providing significant energy savings in cold periods and cold regions and increasing the market and nutritional value by increasing the N content in the manure (Pereira et al., 2019a).

Ammonia is a colorless, pungent gas lighter than air. In addition, since it is a polar compound, it is highly soluble in water.  $\text{NH}_3$  is essential in its aqueous solutions (Equation VII). An acidic environment must be formed to protonate to non-volatile ammonium ( $\text{NH}_4^+$ ) (Equation VIII). The optimum pH levels for the evaporation of  $\text{NH}_3$  are in the 7-10 range. If the environment is at pH 6.5, the  $\text{NH}_3$  volatility will decrease (Spiels et al., 2019; Rhoades et al., 2010). The acidic environment is a desirable environment to reduce evaporation. By reducing the  $\text{NH}_3$  evaporation in the manure, the amount of emission in the environment is reduced, and a better quality fertilizer is obtained by increasing the N content of the fertilizer. The basic principle in acidification of the fertilizer can lower the fertilizer's pH so that less  $\text{NH}_3$  evaporation will occur in  $\text{NH}_3$  aqueous environments. Therefore, reducing the litter material's pH level is very important in reducing the emission of  $\text{NH}_3$ .



Three different strategies can be applied to reduce  $\text{NH}_3$  emissions from poultry production systems:

- I) reduction of N excretion with dietary changes,
- II) reduction of N excretion emitted by additives applied to litter,
- III) N from the polluted air with scrubber or biofilter/recovery (Van der Heyden et al., 2015; Sigurdarson et al., 2018).

Chemical litter changes are available as the best practice to reduce NH<sub>3</sub> emissions, foodborne pathogens, odor and increase litter fertilizer potential (Choi & Moore, 2008; Miles et al., 2011b; Hunolt et al., 2015). The additives used are generally acidic and prevent evaporation by converting ammonia to ammonium. Acidifying additives used in litter and manure wastes reduce the pH value, reducing NH<sub>3</sub> evaporation, and reducing emission rate. As a result, more N is retained as NH<sub>4</sub><sup>+</sup> by litter using acidifying additives. Thus evaporation is reduced, and litter fertilizer value increases. Acidifying agents also inhibit bacterial and enzyme activities that play a role in NH<sub>3</sub> formation, reducing NH<sub>3</sub> formation, and preserving the N content of the fertilizer (Li et al., 2013). Reducing ammonia in the poultry house improves indoor air quality, and acidifiers are used to provide economic benefits by reducing the amount of ventilation and heating costs.

Various studies have demonstrated the ability of chemicals and additives added to the litter to absorb gas emissions. Nakauae et al. (1981) applied and evaluated clinoptilolite first as an additive to litter and then as a feed additive in a study they conducted on a broiler farm. They applied it to the broiler litter at a rate of 5 kg / m<sup>2</sup> and reported that the NH<sub>3</sub> emission rate could be reduced up to 35%. They stated that clinoptilolite added to the feed at a rate of 10% reduced the NH<sub>3</sub> concentration in the air up to 8%.

Moore et al. (2000) examined the NH<sub>3</sub> volatility, litter quality, production, and phosphorus (P) flow by adding aluminum sulfate (Al<sub>2</sub>(SO<sub>4</sub>)<sub>3</sub>·14H<sub>2</sub>O) to the litter in their study in broiler houses. 0.091 kg/chicken aluminum sulfate was added per animal. During the first 3 to 4 weeks, there was a regular reduction in NH<sub>3</sub> emissions. Also, broilers raised in the mixed litter with aluminum sulfate had a heavier weight (1.66 versus 1.73 kg). Phosphorus flow decreased by 73% in the soil treated with aluminum sulfate fertilizers in 3 years compared to the soil treated with normal litter. The results show that poultry litter's aluminum sulfate treatment is a very effective management practice that increases agricultural productivity while reducing non-point-based pollution.

Li et al. (2013) analyzed NH<sub>3</sub> emissions from litter using sodium bisulfate with litter samples taken from a commercial broiler farm. The NH<sub>3</sub> emission reduction rate increased in direct proportion to the sodium bisulfate application rate. Cumulative NH<sub>3</sub> emission was reduced by

51.7%, with an application rate of 244 g / 2 weeks.m<sup>2</sup> under field conditions over three herd periods. In addition to reducing NH<sub>3</sub> emission, the application of sodium bisulfate has significantly improved foot sole quality. The fertilizer value was increased by keeping the total N content in the litter. There was no significant change in body weight gain and feed efficiency.

Lin (2014) investigated different additives (sodium bisulfate [PLT], zeolite, and active charcoal) applied in broiler house litter at different litter moisture levels and application rates. It has been found that PLT application leads to a significant reduction in NH<sub>3</sub> emissions. However, repeated application of zeolite did not result in a significant reduction. Active charcoal, on the other hand, did not show any effect in reducing NH<sub>3</sub> emission. Besides, it has been stated that with increasing moisture in the litter, the NH<sub>3</sub> emission affects directly.

Hunolt et al. (2015) investigated the effects of sodium bisulfate (PLT) they added to broiler litter in the poultry house on NH<sub>3</sub> emissions. Three different applications were carried out, once, with repetitive and without PLT. In once and repeated PLT applications, litter moisture is higher, and litter pH is low. In the repeated application, the NH<sub>3</sub> emission rate was less than the other applications. Besides, since the N ratio in the litter is high, a higher quality fertilizer was obtained.

Nuernberg et al. (2016) wanted to evaluate a low-cost, simple, and fast method to reduce ammonia emissions in poultry litter. They used two different adsorbent zeolites (Cuban zeolite [CZ] and Brazilian basalt ground rock [BZ]) for this. Both zeolites contain SiO<sub>2</sub> and Al<sub>2</sub>O<sub>3</sub> as main components. As a result of the study, both zeolites absorbed ammonia. However, CZ was more effective than BZ (5 g CZ and 20 g BZ) to absorb ammonia. Because CZ has a high surface area, porosity, and acid field ratio.

Wood and Van Heyst (2016) applied PLT to litter during the rearing period in two herds in a turkey incubation and rearing facility. While PLT was applied twice in the first flock, PLT was applied only once in the other herd. After the PLT application, it was found that NH<sub>3</sub> emission decreased by 72% on average over three applications. The application of PLT has been an effective control strategy to reduce ammonia emissions but has been found to have minimal impact on particulate matter emissions.

Chai et al. (2018) evaluated the effects of the additive sodium bisulfate (PLT) added to the litter taken from uncaged egg coops and electrolyzed water sprayed to the environment in a laboratory environment. As a result of the study, the PLT application rate and the NH<sub>3</sub> reduction efficiency are linearly proportional. Due to higher PLT application rates and lower litter pH, NH<sub>3</sub> volatility decreases. A reduction of 28% to 79%

was achieved. After the application of neutral electrolyzed water, the litter moisture content increased up to 60%. PM<sub>2.5</sub>, PM<sub>10</sub>, and TSP levels decreased after the application of electrolyzed water. During the 14-day trial period, water was sprayed for 11 days and not applied for three days. PM levels started to rise again after a period of inactivity.

Pereira et al. (2019a) evaluated the emission rates of ammonia, nitrous oxide, carbon dioxide, and methane by applying magnesium sulfate ( $\text{MgSO}_4 \cdot 7\text{H}_2\text{O}$ ) to broiler litter. While the average annual emission rates of the control group house without magnesium sulfate decreased by 45% for  $\text{NH}_3$  and 25% for  $\text{N}_2\text{O}$  in the house where magnesium sulfate was applied,  $\text{CO}_2$  and  $\text{CH}_4$  emission rates increased by approximately 20%.

Spiehs et al. (2019) applied aluminum sulfate to beef litter material in a laboratory-scale study they conducted. They determined their effects on ammonia, hydrogen sulfide, methane, and carbon dioxide gases with application rates of 0, 2.5, 5, 10%. During the 42-day trial period, 10% aluminum sulfate reduced  $\text{NH}_3$  and  $\text{N}_2\text{O}$  emissions compared to the control group. However, 10% application of aluminum sulfate increased  $\text{CH}_4$  and  $\text{H}_2\text{S}$  emissions compared to the control group, which was not applied to the additive.

Pereira et al. (2019b) examined the effect of using clinoptilolite as a litter additive on ammonia, carbon dioxide, nitrous oxide, and methane emissions and concentrations in chicken coops. As a result of the study, it was seen that clinoptilolite application reduced  $\text{NH}_3$  and  $\text{N}_2\text{O}$  emissions by 28% and 34%, respectively. It has been stated that it has no effect on carbon dioxide emissions and that methane emissions are below the detection limit.

## **5. Conclusion**

Large amounts of poultry manure are produced and accumulated in broiler operations engaged in intensive broiler breeding. Manure can have an alarming effect on the environment. Therefore, it is more important to reduce the pollutants from production systems, control them, and develop control strategies. Although alternative production systems are studied in broiler breeding, generally, littered systems are used. The litter materials used according to the regions (wood shavings, paddy husk, corn stalk, straw, coarse wood shavings, sand, pumice) differ. The litter materials are important for the animals' performance, welfare, productivity, and keeping environmental factors at optimum levels. Various chemicals are used to contain ammonia in the litter, reduce the number of pathogens and microorganisms, and reduce ammonia production by lowering the pH level and obtaining an acidic environment. It has been proven that absorbent and acidifying chemicals added to horses have a more practical and cost-

effective development potential than other methods (McCrary & Hobbs, 2001).

Capturing ammonia nitrogen reduces ammonia evaporation by increasing the proportion of ammonium in the manure. As seen in the studies, different chemicals such as aluminum sulfate ( $\text{Al}_2(\text{SO}_4) \cdot 3.14\text{H}_2\text{O}$ ), PLT (sodium bisulfate), active charcoal, magnesium sulfate ( $\text{MgSO}_4 \cdot 7\text{H}_2\text{O}$ ), clinoptilolite, and natural zeolite types have been used as absorbent materials to reduce  $\text{NH}_3$  emission. It is seen that the additives used are effective in reducing  $\text{NH}_3$  emissions. Especially in poultry studies, there has recently been a new interest in using natural zeolites as a complement to feed additive and litter material to reduce odor and ammonia emissions from broiler houses (Karamanlis et al., 2008). Also, application rates, usage techniques, and the reduction of ammonia emissions vary according to the chemicals used.

Adsorbent additives should be easily accessible, cost-effective, and practical. There are other additives on the market, such as formaldehyde, which reduce ammonia volatility from fertilizers. When formaldehyde reacts with ammonia, it can form a stable complex and inhibit urease and ammonification. In addition to its anti-microbial properties, its use is dangerous and may negatively affect the fertilizer spreads (Anderson, 1994).

Improving the house's indoor conditions is very important in ensuring productivity in poultry and protecting the health and welfare of animals and workers. Reducing ammonia and other harmful gases in the house creates high costs. Therefore, the number of studies is insufficient. The application of additives to reduce ammonia in poultry houses is fascinating due to simple application techniques and low interference with the animals' living conditions. Also, it has advantages such as chemical, physical and microbial effects of additives on wastes, minimum capital expenditure. However, its acidic content may also have a corrosive effect on equipment and structures. The selection of appropriate application methods is crucial for the effective use of adsorbents. More studies are needed to improve the technique and to understand its effectiveness better. Also, more comprehensive studies can be carried out on the effects of additives on other gases, particles, animal welfare, and productivity, as well as reducing  $\text{NH}_3$  emissions.

## References

- Andersson, M. (1994). Performance of additives in reducing ammonia emissions from cow slurry. Sveriges lantbruksuniversitet, Institutionen för jordbrukets biosystem och teknologi (JBT). Available at: [http://www.stalosan.dk/media/7168/3.\\_Performance\\_of\\_additives\\_in\\_reducing\\_ammonia\\_emission\\_from\\_cow\\_slurry.pdf](http://www.stalosan.dk/media/7168/3._Performance_of_additives_in_reducing_ammonia_emission_from_cow_slurry.pdf). Accessed 27 November 2020
- Anderson, N., Strader, R., & Davidson, C. (2003). Airborne reduced nitrogen: ammonia emissions from agriculture and other sources. *Environment International*, 29(2-3), 277-286
- Andrade, W.R., Ferreira, C.D.F., Gates, R.S., Borges, A.C., & Santos, T. (2020). Response from anaerobic digestion of laying hen manure with biochar addition. *Engenharia Agrícola*, 40(3), 315-321
- Aneja, V.P., Bunton, B., Walker, J.T. & Malik, B.P. (2001). Measurement and analysis of atmospheric ammonia emissions from anaerobic lagoons. *Atmospheric Environment*, 35(11), 1949-1958
- Anonymous, 2005. Petition for Exemption From EPCRA and CERCLA Reporting Requirements for Ammonia Emission. Available at: <https://www.uspoultry.org/environment/docs/PoultryPetition.pdf>. Accessed 12 November 2020
- Anonymous, 2020. Emissions of air pollutants in the UK, 1970 to 2018 – Ammonia (NH<sub>3</sub>). Available at: <https://www.gov.uk/government/publications/emissions-of-air-pollutants/emissions-of-air-pollutants-in-the-uk-1970-to-2018-ammonia-nh3>. Accessed 11 November 2020
- Atapattu, N.S.B.M., Senaratna, D., & Belpagodagamage, U.D. (2008). Comparison of ammonia emission rates from three types of broiler litters. *Poultry Science*, 87(12), 2436– 2440
- Atilgan, A., Coskan, A., Hasan, O.Z., & Isler, E. (2010). The vacuum system which is new approach to decrease ammonia level use in broiler housing in winter season. *Journal of the Faculty of Veterinary Medicine, Kafkas University*, 16(2), 257-262
- Boggia A, Paolotti L, & Castellini C. (2010). Environmental impact evaluation of conventional, organic and organic-plus poultry production systems using life cycle assessment. *World's Poultry Science Journal*, 66(1), 95-114
- Cabrera, M.L., & Chiang, S.C. (1994). Water content effect on denitrification and ammonia volatilization in poultry litter. *Soil Science Society of America Journal*, 58, 811-816



- Chai, L., Xin, H., Zhao, Y., Wang, T., Soupir, M., & Liu, K. (2018). Mitigating ammonia and PM generation of cage-free henhouse litter with solid additive and liquid spray. *Transactions of the ASABE*, 61(1), 287-294
- Choi, I.H., & Moore, P.A. (2008). Effect of various litter amendments on ammonia volatilization and nitrogen content of poultry litter. *The Journal of Applied Poultry Research*, 17, 454–462
- Eleroglu, H., & Yalcin, H. (2004). Effects of fattening performance and some litter parameters by addition of zeolite to litter on the broiler. *Journal of Poultry Research*, 5(1), 31-40
- Farrow C., Crolla, A., Kinsley, C., & Mcbean, E. (2016). Anaerobic digestion of chicken manure: Process optimization employing struvite precipitation and novel digestion technologies. *Environmental Progress & Sustainable Energy*, 36(1), 73-82
- Hunolt, A.E., Maguire, R.O., Ogejo, J.A., Badgley, B.D., Frame, W.H., & Reiter, M.S. (2015). Multiple applications of sodium bisulfate to broiler litter affect ammonia release and litter properties. *Journal of environmental quality*, 44(6), 1903-1910
- Isik, O., & Kirkpinar, F. (2020). The effect of feeding on environmental pollutant emissions in broiler production. *Turkish Journal of Agriculture-Food Science and Technology*, 8(1), 234-238
- Karamanlis, X., Fortomaris, P., Arsenos, G., Dosis, I., Papaioannou, D., Batzios, C., & Kamarianos, A. (2008). The effect of a natural zeolite (clinoptilolite) on the performance of broiler chickens and the quality of their litter. *Asian-Australasian Journal of Animal Sciences*, 21(11), 1642-1650
- Kilic, I., & Simsek, E. (2009). The gaseous emissions from animal houses and their environmental impacts. *Uludag University Journal of The Faculty of Engineering*, 14(2)
- Kilic, I. (2011). Characterization of air pollutants in animal barns, Doctoral thesis, Bursa: Uludag University
- Li, H., Lin, C., Collier, S., Brown, W., & White-Hansen, S. (2013). Assessment of frequent litter amendment application on ammonia emission from broilers operations. *Journal of the Air & Waste Management Association*, 63(4), 442-452
- Lin, C. (2014). Mitigating ammonia emission from broilers with frequent litter amendment application, Doctoral thesis, Newark: University of Delaware

- Liu Z., Wang, L., Beasley, D., & E. Oviedo. (2007). Effect of moisture content on ammonia emissions from broiler litter: A laboratory study. *Journal of Atmospheric Chemistry*, 58, 41–53
- McCrary, D.F., & Hobbs, P.J. (2001). Additives to reduce ammonia and odor emissions from livestock wastes: A review. *Journal Environmental Quality*, 30(2), 345-355
- Miles, D.M., Rowe, D.E., & Cathcart, T.C. (2011a). High litter moisture content suppresses litter ammonia volatilization. *Poultry Science*, 90, 1397–1405
- Miles, D.M., Rowe, D.E., & Cathcart, T.C. (2011b). Litter ammonia generation: moisture content and organic versus inorganic bedding materials. *Poultry Science*, 90, 1162–1169
- Molaey, R., Bayrakdar, A., Surmeli, R.O., & Calli, B. (2018). Anaerobic digestion of chicken manure: Mitigating process inhibition at high ammonia concentrations by selenium supplementation. *Biomass and Bioenergy*, (108), 439-446
- Moore Jr, P.A., Daniel, T., & Edwards, D.R. (2000). Reducing phosphorus runoff and inhibiting ammonia loss from poultry manure with aluminum sulfate. *Journal of Environmental Quality*, 29(1), 37-49
- Nakaue, H.S., Koelliker, J.K., & Pierson, M.L. (1981). Studies with clinoptilolite in poultry: II. Effect of feeding broilers and the direct application of clinoptilolite zeolite on clean and reused broiler litter on broiler performance and house environment. *Poultry Science*, 60: 1221–1228
- Naseem, S., & King, A.J. (2018). Ammonia production in poultry houses can affect health of humans, birds, and the environment—techniques for its reduction during poultry production. *Environmental Science and Pollution Research*, 25(16), 15269-15293
- Ni, J.-Q., Chai, L., Chen, L., Bogan, B.W., Wang, K., Cortus, E.L., Heber, A.J., Lim, T.- T., & Diehl, C.A. (2012). Characteristics of ammonia, hydrogen sulfide, carbon dioxide, and particulate matter concentrations in high-rise and manure-belt layer hen houses. *Atmospheric Environment*, 57, 165-174
- Nuernberg, G. B., Moreira, M. A., Ernani, P. R., Almeida, J. A., & Maciel, T. M. (2016). Efficiency of basalt zeolite and Cuban zeolite to adsorb ammonia released from poultry litter. *Journal of environmental management*, 183, 667-672
- Oenema, O., Bannink, A., Sommer, S.G. & Velthof L. (2001). Gaseous nitrogen emissions from livestock farming systems, In Nitrogen in

the Environment: Sources, Problems, and Management, R. F. Follett, and J. L. Hatfield (eds.), Elsevier, 520 pp

- Okano, Y., Hristova, K.R., Leutenegger, C.M., Jackson, L.E., Denison, R.F., Gebreyesus, B., Lebauer, D., & Scow, K.M. (2004). Application of real-time PCR to study effects of ammonium on population size of ammonia-oxidizing bacteria in soil. *Applied and Environmental Microbiology*, 70(2), 1008–1016
- Pereira, J.L., Ferreira, S., Pinheiro, V., & Trindade, H. (2019a). Effect of magnesium sulphate addition to broiler litter on the ammonia, nitrous oxide, carbon dioxide and methane emissions from housing. *Atmospheric Pollution Research*, 10(4), 1284–1290
- Pereira, J.L., Ferreira, S., Pinheiro, V., & Trindade, H. (2019b). Ammonia and greenhouse gas emissions following the application of clinoptilolite on the litter of a breeding hen house. *Environmental Science and Pollution Research*, 26(8), 8352–8357
- Rhoades, M.B., Parker, D.B., Cole, N.A., Todd, R.W., Caraway, E.A., Auvermann, B.W., Topliff, D.R., Schuster, G.L. (2010). Continuous ammonia emission measurements from a commercial beef feedyard in Texas. *Transactions of ASABE*, 53, 1823–1831
- Rockafellow, E.M., Koziel, J.A., & Jenks, W.S. (2012). Laboratory-scale investigation of UV treatment of ammonia for livestock and poultry barn exhaust applications. *Journal of Environmental Quality*, 41(1), 281–288
- Rodić, V., Perić, L., Đukić-Stojčić, M., & Vukelić, N. (2011). The environmental impact of poultry production. *Biotechnology in Animal Husbandry*, 27(4), 1673–1679
- Sanchis, E., Calvet, S., del Prado, A., & Estellés, F. (2019). A meta-analysis of environmental factor effects on ammonia emissions from dairy cattle houses. *Biosystems Engineering*, 178, 176–183
- Sawyer, C.N., McCarty, P.L., & Parkin, G.F. (2003). Chemistry for environmental engineering and science.
- Sigurdarson, J.J., Svane, S., & Karring, H., (2018). The molecular processes of urea hydrolysis in relation to ammonia emissions from agriculture. *Reviews in Environmental Science Biotechnology*, 17, 241–258
- Spiehs, M.J., Woodbury, B.L., & Parker, D.B. (2019). Ammonia, hydrogen sulfide, and greenhouse gas emissions from lab-scaled manure bedpacks with and without aluminum sulfate additions. *Environments*, 6(10), 108

- Steinfeld, H., Gerber, P., Wassenaar, T., Castel, V., Rosales, M., & de Haan, C. (2006). Livestock's long shadow - environmental issues and options. FAO.
- Stowell, R. (2018). Ammonia loss and emission reporting: Considerations for cattle operations. Available at: <http://newsroom.unl.edu/announce/beef/7498/42942>. Accessed 13 October 2020
- Sutton, M.A., Erisman, J.W., Dentener, F., & Möller, D. (2008). Ammonia in the environment: From ancient times to the present. *Environmental Pollution*, 156(3), 583-604
- Tallentire, C.W., Mackenzie, S.G., & Kyriazakis, I. (2017). Environmental impact trade-offs in diet formulation for broiler production systems in the UK and USA. *Agricultural Systems*, 154: 145-156
- Terzich, M., Quarles, C., Goodwin, M.A., & Brown, J. (1998). Effect of poultry litter treatment (PLT) on death due to ascites in broilers. *Avian Diseases*, 42, 385-387
- Tiquia, S.M., & Tam, N.F.Y. (2000). Fate of nitrogen during composting of chicken litter. *Environmental Pollution*, 110: 535-541
- Van der Heyden, C., Demeyer, C., & Volcke, E.I.P. (2015). Mitigating emissions from pig and poultry housing facilities through air scrubbers and biofilters: state-of-the-art and perspectives. *Biosystems Engineering*, 134, 74-93
- Wood, D.J., & Van Heyst, B.J. (2016). The Effects of PLT Poultry Litter Treatment on Ammonia and Particulate Matter Emissions in a Commercial Turkey Grow-Out Facility. *Transactions of the ASABE*, 59(3), 983-991
- Wu-Haan, W., Powers, W.J., Angel, C.R., Hale III, C.E., & Applegate, T.J. (2007). Effect of an acidifying diet combined with zeolite and slight protein reduction on air emissions from laying hens of different ages. *Poultry Science*, 86, 182-190

